学位論文（要約）

Studies on Photoinduced Electron Transfer Based on Carbon-Bridged Oligo(phenylenevinylene)s

（炭素架橋オリゴフェニレンビニレンに基づく
光誘起電子移動の研究 ）

平成 25 年 12 月博士(理学)申請

東京大学大学院理学系研究科化学専攻

助川　潤平

Abstract

Understanding of the factors that control electron transfer (ET) is of fundamental importance in a variety of fields in science. In the emerging area of molecular electronics, the effects of electron–vibration (e–v) coupling have been attracted significant attention because of the resulting novel physical phenomena. So far, some inorganic semiconductors, such as carbon nanotubes and quantum dots, are known to show strong e–v couplings. Because of their structural ambiguity, the structure-property relationship has remained unclear. In this light, organic semiconductor has several advantages such as structural homogeneity, diversity of molecular design, and processability. However, there have been no examples that show strong e–v coupling comparable to inorganic semiconductors because of the flexibility of the organic semiconductors. To shed light on the overshadowed effects of e–v coupling in the organic semiconductors, the author envisioned that carbon-bridged oligo-*p*-phenylenevinylenes (COPVs), which is featured by well-defined and rigid molecular structures, would be suitable models. In addition, the author aimed to develop a novel photosensitizer by making use of the structural features of COPVs.

Chapter 1 overviews the background of ET and introduces some intriguing features of COPVs. Chapter 2 describes the design, synthesis, and photophysical properties of zinc porphyrin-fullerene conjugates bridged by COPVs. Electron transfer in the Marcus inverted region was accelerated as much as 650-times compared to oligo(phenylenevinylene)s (OPVs) due to the strong electronic coupling and the e–v coupling. Chapter 3 describes the design, synthesis, and photophysical properties of COPV–fullerene conjugates. COPVs showed a strong e–v coupling even then they act as the electron donor. In Chapter 4, a new donor–acceptor system that is characterized by homoconjugation of COPVs were designed and synthesized for artificial photosynthesis. Finally these studies are summarized in Chapter 5.

Contents

Abbreviations

A	acceptor
Ac	acetyl
Anal.	elemental analysis
APCI	atmospheric pressure chemical ionization
aq.	aqueous
Ar	aryl group
a.u.	arbitrary unit
B	bridge
B3LYP	Becke's 3-parameter hybrid with Lee, Young and Parr's correlation functional
Bu	butyl
calcd.	calculated
COPV	carbon-bridged oligo-*p*-phenylenevinylene
CR	charge recombination
CS	charge separation
CT	charge transfer
CV	cyclic voltammetry
D	donor
DBA	donor–bridge–acceptor
DCM	dichloromethane
dec	decomposition
DFT	density functional theory
DMF	*N*,*N*-dimethylformamide
dppf	1,1′-bis(diphenylphosphino)ferrocene
eq	equivalent
ET	electron transfer
e–v	electron–vibration
Fc	ferrocene
GPC	gel permeation chromatography
HT	hole transfer

HOMO	highest occupied molecular orbital
ISC	intersystem crossing
LiNaph	lithium naphthalenide
LUMO	lowest unoccupied molecular orbital
MALDI	matrix-assisted laser desorption ionization
Mp	melting point
MS	mass spectrometry
n-	normal-
NBS	*N*-bromosuccinimide
$NMPC_{60}$	*N*-methylpyrrolidino[60]fullerene
NMR	nuclear magnetic resonance
OF	oligo-fluorene
OP	oligo-phenylene
OPE	oligo-phenyleneethynylene
OPV	oligo-*p*-phenylenevinylene
PET	photoinduced electron transfer
Ph	phenyl
PhCN	benzonitrile
PhMe	toluene
pin	pinacolato
rt	room temperature
THF	tetrahydrofuran
TOF	time of flight
TRZ	triazine
ZnP	zinc porphyrin

Physical Quantities

k	rate constant
λ	total reorganization energy
λ_S	solvent reorganization energy
λ_V	vibrational reorganization energy
V	electronic coupling element
k_B	Boltzmann constant
T	thermodynamic temperature
$\hbar$	Dirac's constant, reduced Plank constant
ω	vibrational wavenumber
S	electron–vibration coupling, Huang–Rhys factor
ΔG^0	standard Gibbs free energy
$\Delta G^{\ddagger}$	activation energy
β	attenuation factor
R	distance
r	spherical radius
E_{ox}	oxidation potential
E_{red}	reduction potential
E_{IP}	energy of radical ion-pair
E_{00}	energy of the excited state from which the electron transfer occurs
E_g^{OP}	energy estimated from the optical band gap
Φ_F	fluorescence quantum yield
τ	lifetime
τ_F	fluorescence lifetime
ε_S	static dielectric constant of solvent
ε_0	dielectric constant of vacuum
e	electronic charge

Chapter 1

General Introduction

1-1. Photoinduced Electron Transfer

The study on the photoinduced electron transfer (PET) is one of the most fundamental topics in the interdisciplinary research field among chemistry, physics, and biology. PET is a process of the photoexcitation of donor (D) or acceptor (A) and the subsequent charge separation (CS) to produce the charge-separated state ($D^{\bullet+} + A^{\bullet-}$) (Equation 1 and 2). Depending on the molecule excited by light, PET can be classified into two types; (1) the electron transfer (ET) from the excited electron donor (D^*) to the acceptor (A) and (2) the hole transfer (HT) from the donor (D) to the excited acceptor (A^*). ET occurs via LUMO, while HT occurs via HOMO. Finally, the charge recombination (CR) occurs to reproduce the ground state when the charge-separated state is not converted into electronic or chemical potential (Equation 3).

$$D^* + A \rightarrow D^{\bullet+} + A^{\bullet-} \quad (1)$$

$$D + A^* \rightarrow D^{\bullet+} + A^{\bullet-} \quad (2)$$

$$D^{\bullet+} + A^{\bullet-} \rightarrow D + A \quad (3)$$

The photosynthesis is the most important example of PET. Figure 1 shows the crystal structure of *Rb. sphaeroids*, a bacterial photosynthetic reaction center.[1] In this system CS occurs stepwisely from the photoexcited dimer of bacterial chlorophyll *a* (BChl) to the quinones (Q) via peripheral bacterio pheophytins (Bphe). The efficiency of CS is almost unity, which is vastly owing to the Marcus inverted region described in the next section. The energy of the charge-separated state is converted into proton gradation in the cell to produce adenosine triphosphate (ATP).

PET is also the key process in the molecular electronics, where single molecule serves as a device such as transistor, memory, and switch. Such molecular devise has attracted due to the tremendous tendency of minitualization of the electric circuit. In addition, molecules can show nonlinear effects, which cannot be seen in the bulk system due to the electron confinement where quantum effects appear.

Thus PET plays a central role in a variety of systems. To this end, it is required to understand the principal of PET and control it. In the next section, the detailed background of the ET study is outlined.

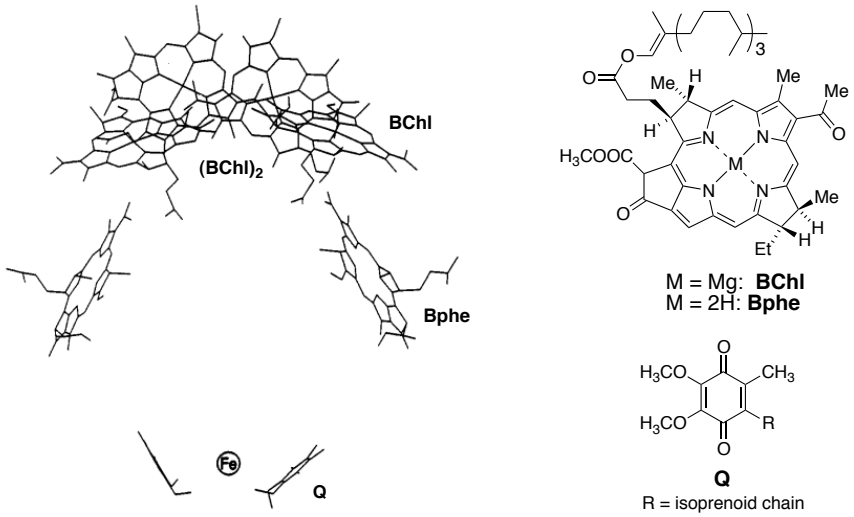

Figure 1. The reaction center of the bacterial photosynthesis. (Reprinted with permission from reference 1. Copyright 1992, American Chemical Society).

1.2 Overview of the Theoretical and Experimental Study on Electron Transfer

The theoretical framework of ET was established by Rudolf A. Marcus in 1956.[2] Although the validity of his theory (so called Marcus theory) had been controversial due to the lack of experimental evidence (vide infra), he eventually won the Novel prize in chemistry in 1992.

Marcus showed that ET occurs according to the Frank-Condon principle, where the Born-Oppenheimer approximation holds, and the energy conservation before and after ET is achieved by the nuclear fluctuation including the solvent polarization. Especially the latter point attracted significant attention because solvents were considered to have negligible effects on the rate of chemical reaction at that time. The reason why the solvents play an important role in ET is that ET occurs via different mechanism with other chemical reaction (i.e. electron tunneling).

The ET scheme is described in figure 2. The ET reaction occurs when the interaction between the donor and acceptor molecules are small via electron tunneling. The energies between the initial state and the final state must be balanced in the reaction, which is achieved by the non-equilibrated state due to the nuclear fluctuation (state III). The ET rate is determined by the frequency of the energy balancing. ET occurs without the nuclear motion according to the Frank-Condon principle (state IV), following nuclear relaxation such as bond and solvent reorganization (state V).

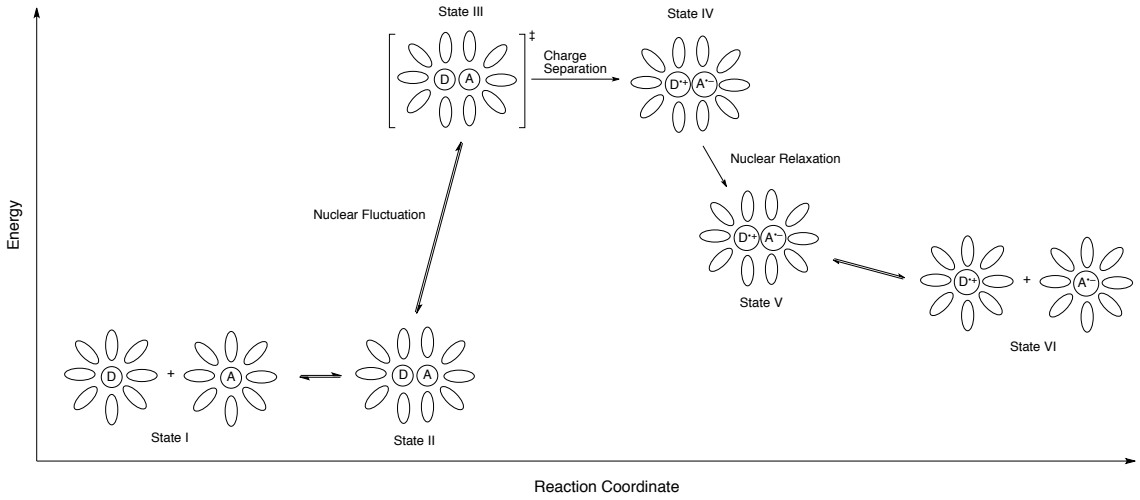

Figure 2. ET reaction scheme in free electron donor (D) and acceptor (A) in solution.

In the high temperature limit, the rate of nonadiabatic ET (k_{ET}) can be written as

$$k_{ET} = \sqrt{\frac{\pi}{\hbar^2 \lambda k_B T}} V^2 \exp\left(-\frac{\left(\Delta G^0_{ET} + \lambda\right)^2}{4\lambda k_B T} \right) \tag{4}$$

In Equation 4, k_B is the Boltzmann constant, T is thermodynamic temperature, ΔG^0_{ET} is the standard free energy change, and λ is the total reorganization energy.

The most striking prediction of the Marcus theory is the presence of the inverted region, where k_{ET} decreases as the driving force ($-\Delta G^0_{ET}$) increases (Figure 3).

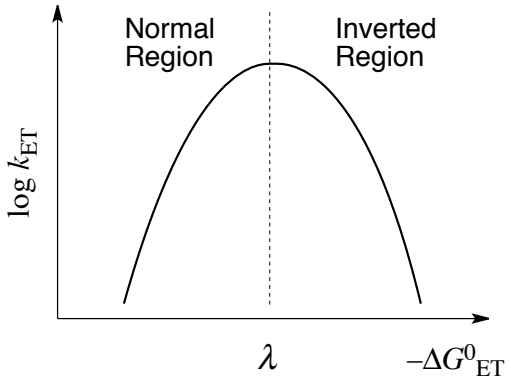

Figure 3. Energy gap low predicted by the Marcus theory.

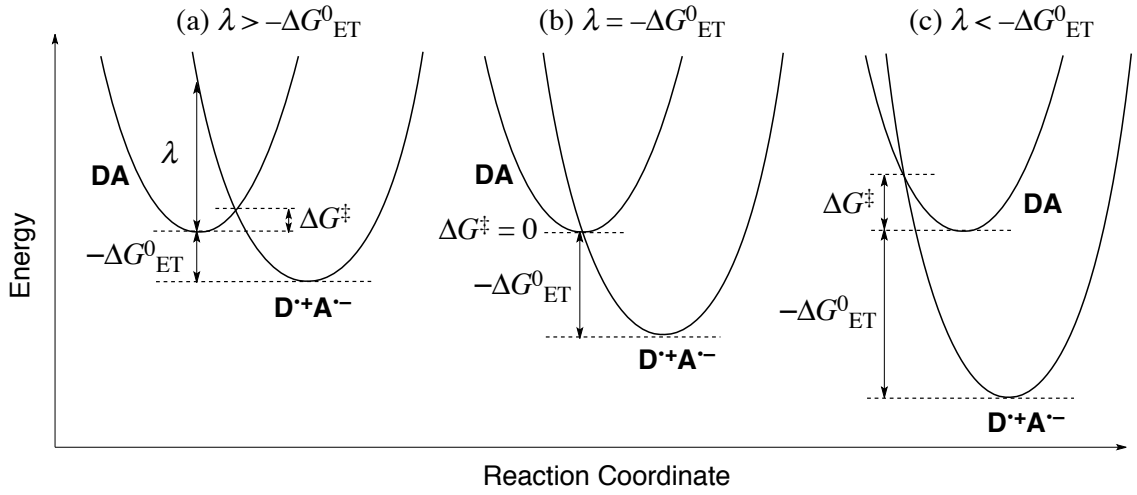

Figure 4. Reaction coordinate for the electron transfer in donor–acceptor (DA) system. The reaction can be categorized into (a) normal region, (b) top region, and (c) inverted region depending on the relationship between the reorganization energy (λ) and the driving force ($-\Delta G^0_{ET}$). The activation energy ($\Delta G^{\ddagger}$) increases as $-\Delta G^0_{ET}$ increases in the inverted region.

The most famous experimental trial to prove the Marcus theory in the early stage was conducted by Rehm and Weller in 1970.[3] They estimated the quenching rate of the emission from various fluorophores by quencher according the Stern-Volmer equation. The figure 5 shows the plots of ET rates versus the free energy change, suggesting that the inverted region was not observed (Note that the x-axis is not the driving force). Electron transfer can occur longer distance between the donor and acceptor, and thus the reorganization energy will increase. On the other hand, Marcus theory can be applied in the normal region because ET occurs at the distance where λ becomes minimum (i.e. λ is constant).

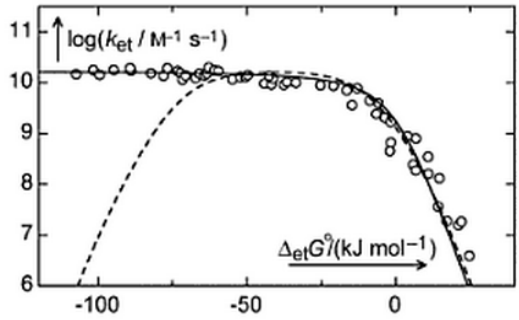

Figure 5. The plot of the quenching rate (k_q) versus the free energy change (ΔG^0_{ET}) (from Petr Clán and Jakob Wirz, Photochemistry of Organic Compounds: From Concepts to Practice. Copyright © 2009 by John and Wiley Sons, Inc. Reprinted by permission of John and Wiley Sons, Inc.).

To improve the classical Marcus theory, several groups such as Jortner,[4] Fischer, Van Duyne, and Hopfield took into account the quantum mechanical nature of high-frequency molecular vibration. This theory is called as *semi-classical* Marcus theory, which can be written as follows.

$$k_{ET} = \sqrt{\frac{\pi}{\hbar^2 \lambda_S k_B T}} |V|^2 \sum_n^{\infty} \frac{e^{-s} S^n}{n!} \exp\left(-\frac{\left(\Delta G^0_{ET} + \lambda_S + n\hbar\omega\right)^2}{4\lambda_S k_B T} \right) \tag{5}$$

$$S = \frac{\lambda_V}{\hbar\omega} \tag{6}$$

In Equation 5 and 6, S is the electron–vibration (e–v) coupling, n donates the vibrational quantum number, ω is the averaged frequency of the coupled quantum mechanical vibration mode, λ_V is the vibrational reorganization energy, and λ_S is the solvent reorganization energy.

The semi-classical Marcus theory considers a vibrational excited state $(D–A)^*$. In the normal region (Figure 6a) and the top region (Figure 6b), the vibrational ground state will be favored as a product because of the lowest activation energy (G). On the other hand, the vibrational excited state will be favored in the inverted region (Figure 6c) because of the lower activation energy. Thus the e–v coupling provides the less

pronounced inverted region. This behavior is simulated in Figure 7. It can be seen that the fitting is almost symmetrical when $S = 0.5$, and thus it resembles the fitting by the *classical* Marcus equation.

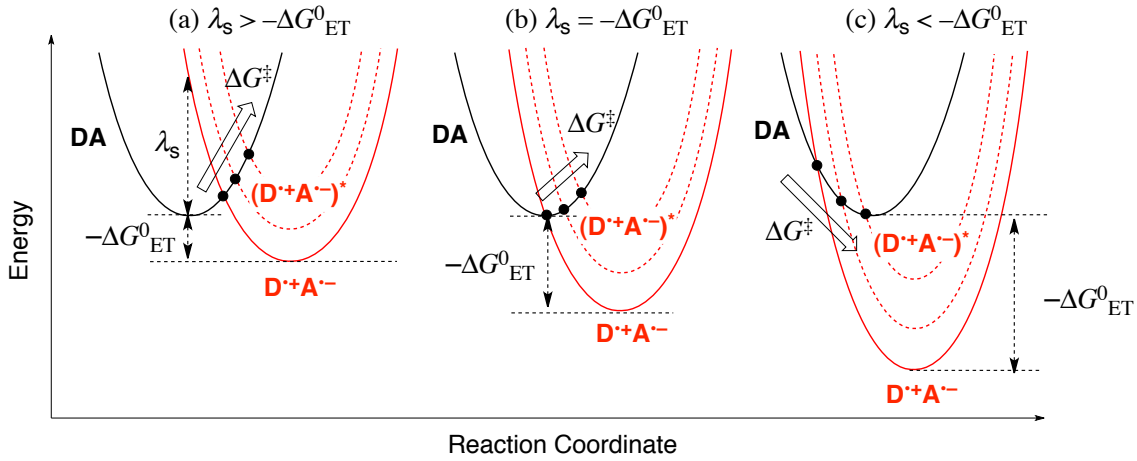

Figure 6. Effects of e–v coupling. Transition states (black dots) leading to vibrational excited state $(D^{\bullet+}A^{\bullet-})^*$ have smaller activation energy ($\Delta G^{\ddagger}$) in the inverted region (c).

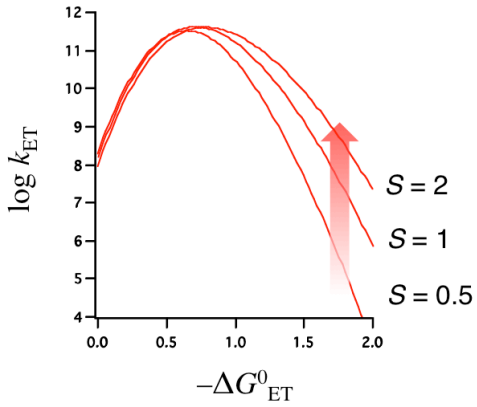

Figure 7. Simulations of the driving force dependence with variable S values (0.5, 1 and 2) according to Equation 5. Other parameters were fixed with $\lambda_s = 0.5$ eV, $V = 0.005$ eV, $\hbar\omega = 0.186$ eV, and $T = 298$ K in all cases.

The first experimental proof of the Marcus inverted region was provided by Miller *et al*. in 1984.[5,6] They constructed the covalently connected donor-acceptor system using a steroid as a bridge (Figure 8). This strategy enabled to investigate the effects of the nuclear factor (i.e. the driving force dependence of ET rate) while maintaining the electronic factor unchanged because of the constant donor-acceptor

distance. The electron donating biphenyl radical anion was created by the pulse radiolysis.

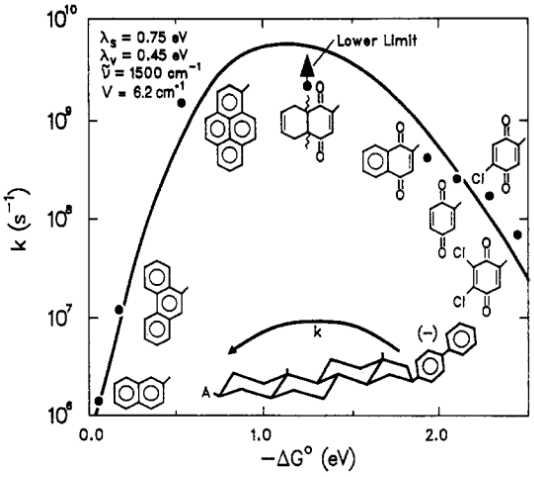

Figure 8. Plots of the electron transfer rate (k) versus the driving force ($-\Delta G^0$). Fitting was performed according to the *semi-classical* Marcus equation (Reprinted with permission from reference 5. Copyright 1986, American Chemical Society).

For the artificial photosynthesis (i.e. light-to-energy conversion), the lifetime of the charge-seprated state (τ) needs to be as long as possible to increase the efficiency of the successive reaction. Thus the decrement in CR rate (k_{CR}) is the main challenge because τ is the inverse of k_{CR} (Equation 7)

$$\tau = \frac{1}{k_{CR}} \tag{7}$$

There are two strategies to decrease k_{CR}; one is to decrease the reorganization energy λ and the other is to decrease the electronic coupling V_{DA}. In 1996, Imahori, *et al*. reported that the fullerene serves as an excellent acceptor due to the rigid skeleton and large spherical radius.[7,8] Later Imahori and Fukuzumi *et al*. have synthesized a series of porphyrin-fullerene conjugates, showing that CR process is located deeply in the inverted region (Figure 9).[9–14] The total reorganization energy λ can be estimated to be 0.5 eV from the top of the parabola, which is much smaller than that of porphyrin–quinone systems (*e.g.* 1.2 eV). Thus the porphyrin-fullerene conjugates have been exploited as the most standard donor–acceptor pair to achieve a long-lived charge-separated state.[15]

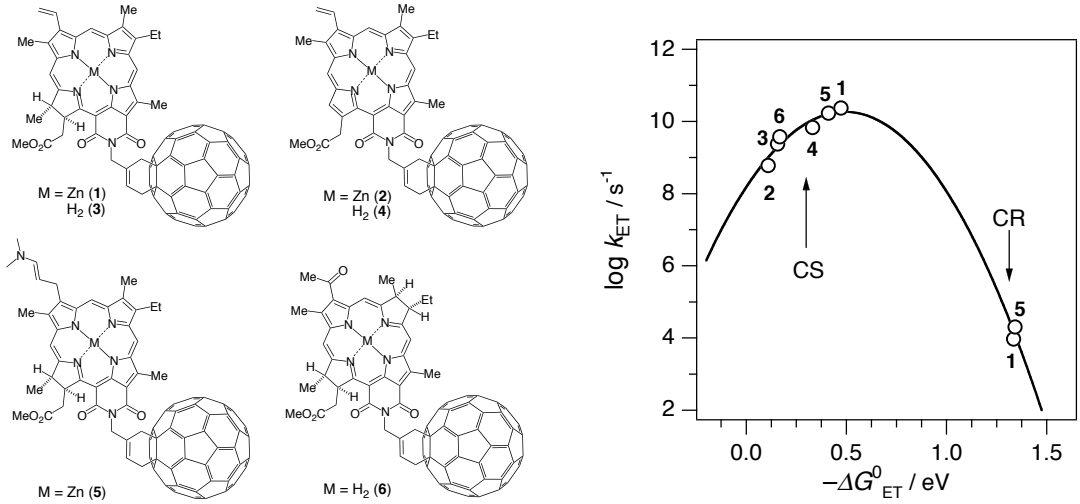

Figure 9. Fitting of the rate of CS and CR versus the driving force ($-\Delta G^0_{ET}$) based on the *classical* Marcus equation. (Created from the data in reference 13 and 14).

To summarize this section, the inverted region of the Marcus theory can be observed when the distance between the donor and acceptor is well defined. The symmetric parabola can be observed when the rigid molecules such as porphyrin and fullerene are used as donor and acceptor because of the small vibrational reorganization energy (λ_V). On the other hand, molecules containing carbonyl[5,16] and cyano[17] group shows the less pronounced inverted region because of the effects of the e–v coupling. Marcus inverted region is responsible for the long lifetime of the charge-separated state in photosynthesis. Porphyrin–fullerene conjugates have emerged as suitable donor-acceptor systems for the light-to-energy conversion due to the small reorganization energy and suitable energy levels.

1-3. Study on the Bridge

In most biological, chemical, and physical systems, electron transfer occurs via bridge. In donor–bridge–acceptor (DBA) systems, the nature of the bridge primarily determines the efficiency of the long-distance electron transfer. In the long-distance electron transfer, the rate is primarily determined by the electronic coupling between donor and acceptor (V_{DA}), which is the overlap of D–A wavefunctions mediated by the bridge.

$$V_{DA} = \frac{V_{DB}V_{BA}}{\omega_{DB}}\left(\frac{V_{BB}}{\omega_{DB}}\right)^{n-1} \tag{8}$$

Here, V_{DB} and V_{BA} are the electronic coupling of donor and bridge and bridge and acceptor, respectively. ω_{DB} is the energy gap between donor and bridge. n is the number of the repeating unit. The electronic coupling between bridge sites V_{BB} is dependent on the twist angle of the bridge, thus V_{BB} can be significantly reduced by the torsional motions in flexible bridges.

In the long-distance ET, the V_{DA} shows exponential distance dependence,

$$V = V_0 \exp\left(-\frac{\beta}{2}R_{DA}\right) \tag{9}$$

Here, V_0 is the preexponential factor (s^{-1}), R_{DA} is the donor-acceptor center-to-center distance (Å) and β is the attenuation factor ($Å^{-1}$). Thus the distance dependence of ET can be written as

$$k_{ET} = k_0 \exp(-\beta R_{DA}) \tag{10}$$

Here, k_0 is the preexponential factor (s^{-1}). Typical β value is 4.0 $Å^{-1}$ for vacuum, 1.0–1.4 $Å^{-1}$ for peptides in protein,[18,19] 0.8–1.0 $Å^{-1}$ for saturated hydrocarbons,[20–22] and 0.01–0.6 $Å^{-1}$ for π-conjugated molecules such as oligo-phenylene,[23–29] oligo-fluorene,[30–33] oligo-phenylenevinylene,[34] and oligo-phenyleneethynylene[35–38] (Figure 10). The molecules with a small attenuation factor are expected to serve as *molecular wires*, which are able to transport electrons over long distances in molecular size electronic circuits.[39]

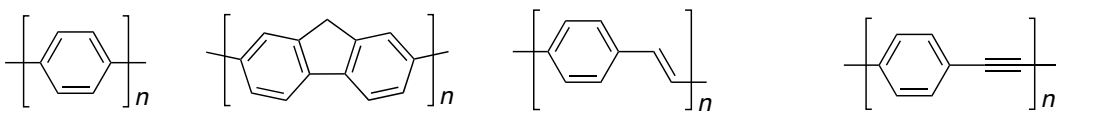

oligo-*p*-phenylene (**OP*n***) | oligo-fluorene (**OF*n***) | oligo-*p*-phenylenevinylene (**OPV*n***) | oligo-*p*-phenylenethynylene (**OPE*n***)

Figure 10. Structures of representative molecular wires.

It is well known that the attenuation factor primarily depends on the

mechanism of electron transfer. Superexchange-mediated tunneling (eq. 11) and thermally-activated hopping (eq. 12) are relevant for the mechanism of the molecular wires. The former is a single process where the bridge acts as a tunneling barrier, while the later is a sequential process where the bridge acts as real sites to temporally accommodate a charge. Basically superexchange mechanism shows stronger distance dependence than the hopping mechanism.

$$\mathbf{D^{*}BA \rightarrow D^{\bullet+}BA^{\bullet-}} \tag{11}$$

$$\mathbf{D^{*}BA \rightarrow D^{\bullet+}B^{\bullet-}A \rightarrow D^{\bullet+}BA^{\bullet-}} \tag{12}$$

Wasielewski *et al*. reported that lengthening the OPV bridges shows the switch in the mechanism (Figure 11).[40] In the short bridge region (n = 1 and 2), the LUMO levels of the bridge is much higher than that of donor The crossover of the mechanism can be seen in the most molecular wires. When the time scale of both ET and vibrational motion become close, the electronic factor V_{DA} in the Marcus theory becomes dependent on the nuclear coordinate, showing a complex temperature dependence.[41]

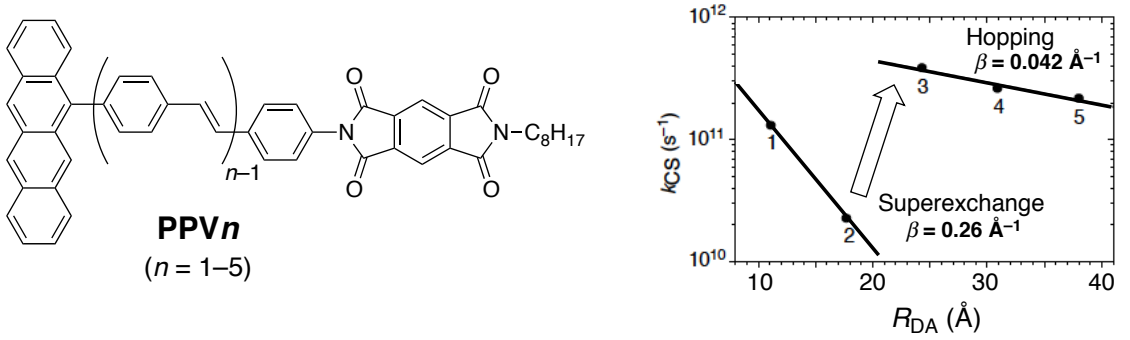

Figure 11. Crossover of the mechanism from superexchange to hopping in OPV wires (Reprinted with permission from reference 40. Copyright © 1998, Rights Managed by Nature Publishing Group).

1-4. Carbon-Bridged Oligo-*p*-(Phenylenevinylene)s

As described in the previous section the conventional π-conjugated molecular wires potentially suffer from torsional motions, which reduce the electronic coupling. In addition, such a low frequency vibration serves as "hot bath", which accepts an excess energy in ET to maintain the energy conservation law. Thus the high frequency vibrations such as skeletal C=C stretching vibration, which is relevant to the electron-vibration (e–v) coupling, are not significant. E–v coupling has been attracted much attention because it can offer new physical phenomena beneficial to the development of molecular electronics. However, the structure–property relationship remains unclear because strong e–v coupling has been observed for inorganic semiconductors such as carbon nanotube and quantum dots, which are structurally inhomogeneous. Thus the well-defined organic semiconductor with strong e–v coupling is desired. In this light rigid and planar π-conjugated molecule such as carbon-bridged oligo-*p*-(phenylenevinylene)s (COPV), which is fused oligo-*p*-(phenylenevinylene)s (OPV), would be possible candidates to study the e–v coupling in organic molecular wires (Figure 12). [42–45]

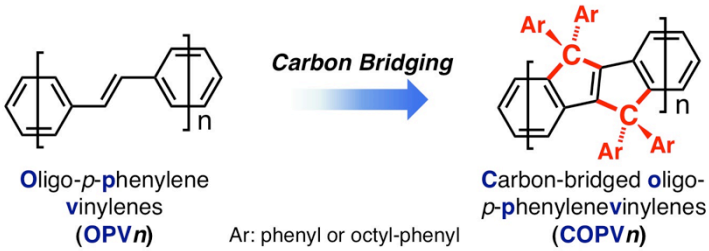

Figure 12. Structure of **COPV*n*** and **OPV*n***.

Figure 13 illustrates the effects of the rigidification and planarization of the OPV skeleton. The singlet excited state energy estimated by the absorption and emission spectra becomes smaller, suggesting the effective π-conjugation in COPVs. The maximum absorption wavelength increased from 481 to 544 nm (Figure 12a). The shift of a Raman-active vibrational frequency is pronounced in the COPVs, indicating the effective e–v coupling (Figure 12b).

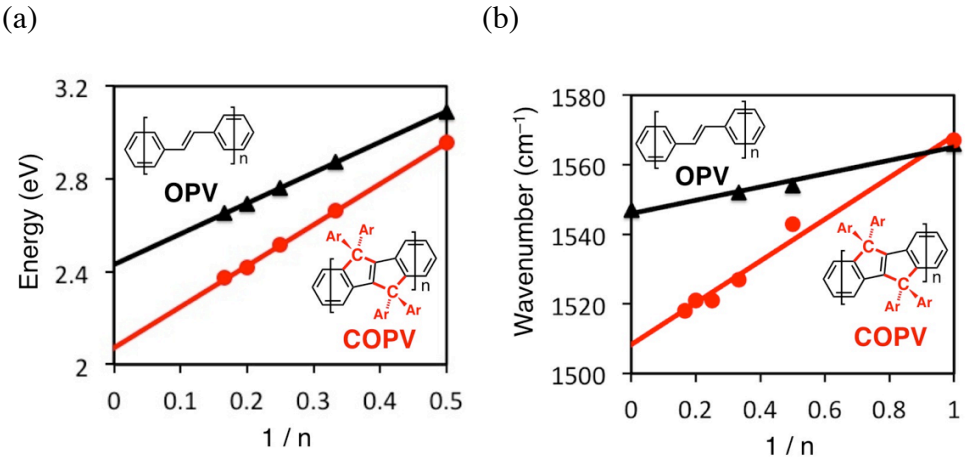

Figure 13. Electronic coupling and e–v coupling in OPV and COPV. (a) Plots of the singlet excited state energy versus the inverse of the unit number. (b) Plots of the wavenumber of a Raman-active vibrational mode versus the inverse of the unit number. (Created from the data in reference 44. Copyright 2012, American Chemical Society).

Meanwhile, the structure of COPVs is featured by homoconjugation at the bridging carbon atoms (Figure 14). Homoconjugation is defined as the orbital overlap of two π-systems separated by a non-conjugated group such as CH_2 (IUPAC). Electronic coupling via homoconjugation has been well investigated in cationic compounds, however, that in neutral compounds, especially in D–A systems, is poorly understood. Thus obtaining insights into the properties of homoconjugated D–A systems is challenging and is of particular interest in artificial photosynthesis.

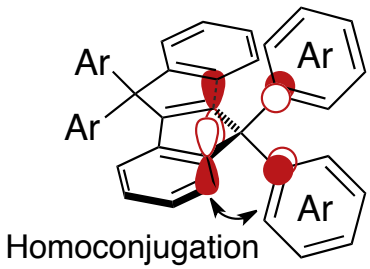

Figure 14. Orbital interaction between COPV backbone and aryl substituents.

1-5. Thesis outline

The author targeted COPVs as model compounds to study the effects of rigidity and planarity of molecular structures on electron transfer properties as well as to investigate homoconjugative interactions in donor–acceptor systems, both of which have not been explored so far. In Chapter 2, an unprecedentedly strong e–v coupling was confirmed in zinc porphyrin-fullerene conjugates bridged by COPVs. Chapter 3 describes the photophysical properties of COPV–fullerene dyads, which is a complementary study to Chapter 2. The e–v coupling of COPVs is also significant when they act as electron donor. In Chapter 4, a new class of homoconjgated donor–acceptor system involving COPV and triazine was investigated. Efficient CS and 100-times slower CR suggested that COPVs are useful for photosensitizer. Chapter 5 is the overview of the study.

References

1 Wasielewski, M. R. Photoinduced electron transfer in supramolecular systems for artificial photosynthesis. *Chem. Rev.* **92,** 435–461 (1992).

2 Marcus, R. A., On the theory of oxidation-reduction reactions involving electron transfer. I. *J. Chem. Phys.* **24**, 966–978 (1956).

3 Rehm, D.; Weller, A. *Isr. J. Chem.* **8**, 259 (1970).

4 Jortner, J., Temperature dependent activation energy for electron transfer between biological molecules, *J. Chem. Phys.* **64**, 4860–4867 (1976).

5 Closs, G. L., Calcaterra, L. T., Green, N. J., Penfield, K. W., Miller, J. R, Distance, stereoelectronic effects, and the Marcus inverted region in intramolecular electron transfer in organic radical anions, *J. Phys. Chem.* **90**, 3673 (1986).

6 Closs, G. L. & Miller, J. R. Intramolecular long-distance electron transfer in organic molecules, *Science* **240**, 440–447 (1988).

7 Imahori, H. *et al*. The small reorganization energy of C_{60} in electron transfer. *Chemical physics letters* **263,** 545–550 (1996).

8 Imahori, H., Hagiwara, K., Akiyama, T., Taniguchi, S., Okada, T. & Sakata, Y. Synthesis and photophysical property of porphyrin-linked fullerene, *Chem. Lett.* **24**, 265–266 (1995).

9 Imahori, H. *et al*. Modulating charge separation and charge recombination dynamics in porphyrin–fullerene linked dyads and triads: Marcus-normal versus inverted region. *J. Am. Chem. Soc.* **123,** 2607–2617 (2001).

10 Imahori, H. *et al*. Charge separation in a novel artificial photosynthetic reaction center lives 380 ms. *J. Am. Chem. Soc.* **123,** 6617–6628 (2001).

11 Imahori, H. *et al*. An extremely small reorganization energy of electron transfer in porphyrin–fullerene dyad. *J. Phys. Chem. A* **105,** 1750–1756 (2001).

12 Chukharev, V. *et al*. Tuning the ground-state and excited-state interchromophore interactions in porphyrin–fullerene π-stacks. *J. Phys. Chem. B* **108,** 16377–16385 (2004).

13 Fukuzumi, S. *et al*. Photochemical and electrochemical properties of zinc chlorin–C_{60} dyad as compared to corresponding free-base chlorin–C_{60}, free-base porphyrin–C_{60}, and zinc porphyrin–C_{60} dyads. *J. Am. Chem. Soc.* **123,** 10676–10683 (2001).

14 Ohkubo, K. *et al*. Small reorganization energy of intramolecular electron transfer in fullerene-based dyads with short linkage. *J. Phys. Chem. A* **106,** 10991–10998 (2002).

15 Fong, R., Schuster, D. I. & Wilson, S. R. Synthesis and photophysical properties of steroid-linked porphyrin–fullerene hybrids. *Org. Lett.* **1,** 729–732 (1999).

16 Wiederrecht, G. P., Niemczyk, M. P., Svec, W. A. & Wasielewski, M. R. Ultrafast photoinduced electron transfer in a Chlorophyll-based triad: Vibrationally hot ion pair intermediates and dynamic solvent effects. *J. Am. Chem.*

Soc., **118**, 81–88 (1996).

17 Koch, M. *et al*. Real-time observation of the formation of excited radical ions in bimolecular photoinduced charge separation: Absence of the Marcus inverted region explained. *J*. *Am*. *Chem*. *Soc*., **135**, 9843–9848 (2013).

18 Winkler, J. R. & Gray, H. B. Electron transfer in ruthenium-modified proteins. *Chem*. *Rev*. **92**, 369–379 (1992).

19 Moser, C. C., Keske, J. M., Warncke, K., Farid, R. S. & Dutton, P. L. Nature of biological electron transfer. *Nature* **355**, 796–802 (1992).

20 Oevering, H. *et al*. Long-range photoinduced through-bond electron transfer and radiative recombination via rigid nonconjugated bridges: distance and solvent dependence. *J*. *Am*. *Chem*. *Soc*. **109**, 3258–3269 (1987).

21 Helms, A., Heiler, D. & McLendon, G. Electron transfer in bis-porphyrin donor-acceptor compounds with polyphenylene spacers shows a weak distance dependence. *J*. *Am*. *Chem*. *Soc*. **114**, 6227–6238 (1992).

22 Paulson, B. P., Miller, J. R., Gan, W.-X. & Closs, G. Superexchange and sequential mechanisms in charge transfer with a mediating state between the donor and acceptor. *J*. *Am*. *Chem*. *Soc*. **127,** 4860–4868 (2005).

23 Hanss, D., Walther, M. E. & Wenger, O. S. Accelerated hole transfer across a molecular double barrier. *Chem*. *Commun*. **46,** 7034 (2010).

24 Walther, M. E. & Wenger, O. S. Hole tunneling and hopping in a $Ru(bpy)^{32+}$-phenothiazine dyad with a bridge derived from oligo-*p*-phenylene. *Inorg*. *Chem*. **50,** 10901–10907 (2011).

25 Indelli, M. T. *et al*. Electron transfer across modular oligo-*p*-phenylene bridges in $Ru(bpy)_2(bpy–ph_n–DQ)^{4+}$ (n = 1–5) dyads. Unusual effects of bridge elongation. *J*. *Phys*. *Chem*. *A* **116,** 119–131 (2012).

26 Hanss, D. & Wenger, O. S. Tunneling barrier effects on photoinduced charge transfer through covalent rigid rod-like bridges. *Inorg*. *Chem*. **48,** 671–680 (2009).

27 Indelli, M. T., Chiorboli, C., Flamigni, L., De Cola, L. & Scandola, F. Photoinduced electron transfer across oligo-*p*-phenylene bridges. Distance and conformational effects in Ru(II)–Rh(III) dyads. *Inorg*. *Chem*. **46,** 5630–5641 (2007).

28 Weiss, E. A. *et al*. Conformationally gated switching between superexchange and hopping within oligo-*p*-phenylene-based molecular wires. *J*. *Am*. *Chem*. *Soc*. **127,** 11842–11850 (2005).

29 Weiss, E. A. *et al*. Making a molecular wire: Charge and spin transport through para-phenylene oligomers. *J*. *Am*. *Chem*. *Soc*. **126,** 5577–5584 (2004).

30 Goldsmith, R. H. *et al*. Wire-like charge transport at near constant bridge energy through fluorene oligomers. *Proc*. *Natl*. *Acad*. *Sci*. *USA* **102,** 3540–3545 (2005).

31 Atienza-Castellanos, C. *et al*. Determination of the attenuation factor in fluorene-based molecular wires. *Chem*. *Commun*. 5164–5166 (2007).

32 Goldsmith, R. H. *et al*. Challenges in distinguishing superexchange and hopping mechanisms of intramolecular charge transfer through fluorene oligomers. *J. Phys. Chem. A* **112,** 4410–4414 (2008).

33 Ricks, A. B. *et al*. Exponential distance dependence of photoinitiated stepwise electron transfer in donor–bridge–acceptor molecules: Implications for wirelike behavior. *J. Am. Chem. Soc*. **134,** 4581–4588 (2012).

34 Giacalone, F., Segura, J. L., Martin, N. & Guldi, D. M. Exceptionally small attenuation factors in molecular wires. *J. Am. Chem. Soc*. **126,** 5340–5341 (2004).

35 Pettersson, K. *et al*. Singlet energy transfer in porphyrin-based donor–bridge–acceptor systems: Interaction between bridge length and bridge energy. *J. Phys. Chem. A* **110,** 310–318 (2006).

36 Wielopolski, M., Atienza, C., Clark, T., Guldi, D. M. & Martin, N. p-Phenyleneethynylene molecular wires: Influence of structure on photoinduced electron-transfer properties. *Chem. Eur. J*. **14,** 6379–6390 (2008).

37 Cho, H. S. *et al*. Excited-state energy transfer processes in phenylene- and biphenylene-linked and directly-linked zinc(II) and free-base hybrid diporphyrins. *J. Phys. Chem. A* **105,** 4200–4210 (2001).

38 Tashiro, K. *et al*. Long-range photoinduced electron transfer mediated by oligo-*p*-phenylenebutadiynylene conjugated bridges. *Chem. Lett*. **35,** 518–519 (2006).

39 Joachim, C., Gimzewski, J. K. & Aviram, A. Electronics using hybrid-molecular and mono-molecular devices. *Nature* **408,** 541–548 (2000).

40 Davis, W. B., Svec, W. A., Ratner, M. A. & Wasielewski, M. R. Molecular-wire behaviour in *p*-phenylenevinylene oligomers. *Nature* **396,** 60–63 (1998).

41 Davis, W. B., Ratner, M. A. & Wasielewski, M. R. Conformational gating of long distance electron transfer through wire-like bridges in donor–bridge–acceptor molecules. *J. Am. Chem. Soc*. **123,** 7877–7886 (2001).

42 Zhu, X.; Mitsui, C.; Tsuji, H. & Nakamura,E, Modular synthesis of 1*H*-indenes, dihydro-*s*-indacene, and diindenoindacene-a carbon-bridged *p*-phenylenevinylene congener, *J. Am. Chem. Soc*. **131**, 13596–13597 (2009).

43 Zhu, X., Tsuji, H., Nakabayashi, K., Ohkoshi, S. & Nakamura, E. Air- and heat-stable planar tri-*p*-quinodimethane with distinct biradical characteristics. *J. Am. Chem. Soc*. **133**, 16342–16345 (2011).

44 Zhu, X., Tsuji, H., López-Navarrete, J. T., Casado, J. and Nakamura, E., Carbon-bridged oligo(phenylenevinylene)s: stable π-systems with high responsiveness to doping and excitation, *J. Am. Chem. Soc*. **134**, 19254–19259 (2012).

45 Zhu, X. *et al*. New sensitizers for dye-sensitized solar cells featuring a carbon-bridged phenylenevinylene. *Chem. Commun*., **49***,* 582-584 (2013).

Chapter 2

Synthesis and Photophysical Properties of Zinc Porphyrin–Fullerene Conjugates Bridged by Carbon-Bridged Oligo(Phenylenevinylene)s

2-1. Introduction

Recent experimental and theoretical works on electron transfer related to photosynthesis, light-to-energy conversion, and molecular electronics have revealed the significant importance of the electron-vibration (phonon) interactions. High frequency vibrations such as skeletal stretching vibration can offer new physical phenomena such as inelastic tunneling[1] and multi electron generation[2,3], while low frequency vibrations such as torsional motion just dissipate the energy as heat. Due to the necessity of the structural rigidity, only the rigid materials such as carbon nanotubes,[4] graphenes,[5,6] and quantum dots[7,8] are known to exhibit strong electron-vibration (e–v) couplings, which have hampered the understanding of the structure-property relationship. To address this issue, we used our original molecular materials, carbon-bridged oligo-*p*-phenylenevinylenes (COPVs),[9] which possess well-defined rigid molecular structures. In fact, we observed as much as 650-fold acceleration of the electron transfer in the Marcus inverted region compared to the flexible oligo-*p*-phenylenevinylenes (OPVs) due to the operation of the unprecedented inelastic tunneling mechanism. The electron-vibration coupling caused by the skeletal rigidity accounts for the 50-fold acceleration and the electronic coupling due to the planarity accounts for the rest 13-fold acceleration.

2-2. Results&Discussion

2-2-1. Synthesis of ZnP–COPV*n*–C_{60} (*n* = 1–3)

To study the e–v coupling properties of the COPV molecules, we synthesized a series of donor-bridge-acceptor (DBA) systems (**ZnP–COPV*n*–C_{60}**, *n* = 1–4; Figure 1a) with zinc porphyrin (ZnP) as a donor, [60]fullerene (C_{60}) as an acceptor, and COPV*n* (*n* = 1–4) as a bridge.[10,11,12] The OPV-based DBA systems (**ZnP–OPV*n*–C_{60}**, *n* = 3 and 5; Figure 1b) reported previouslywere used as reference molecules.[13] COPVs were studied because our previous resonance Raman studies suggested strong e–v coupling.[9,14] On the other hand, ZnP and C_{60} were selected because of the small e–v coupling,[15,16] which would avoid masking the e–v coupling effects stemming from the bridge.[17–19]

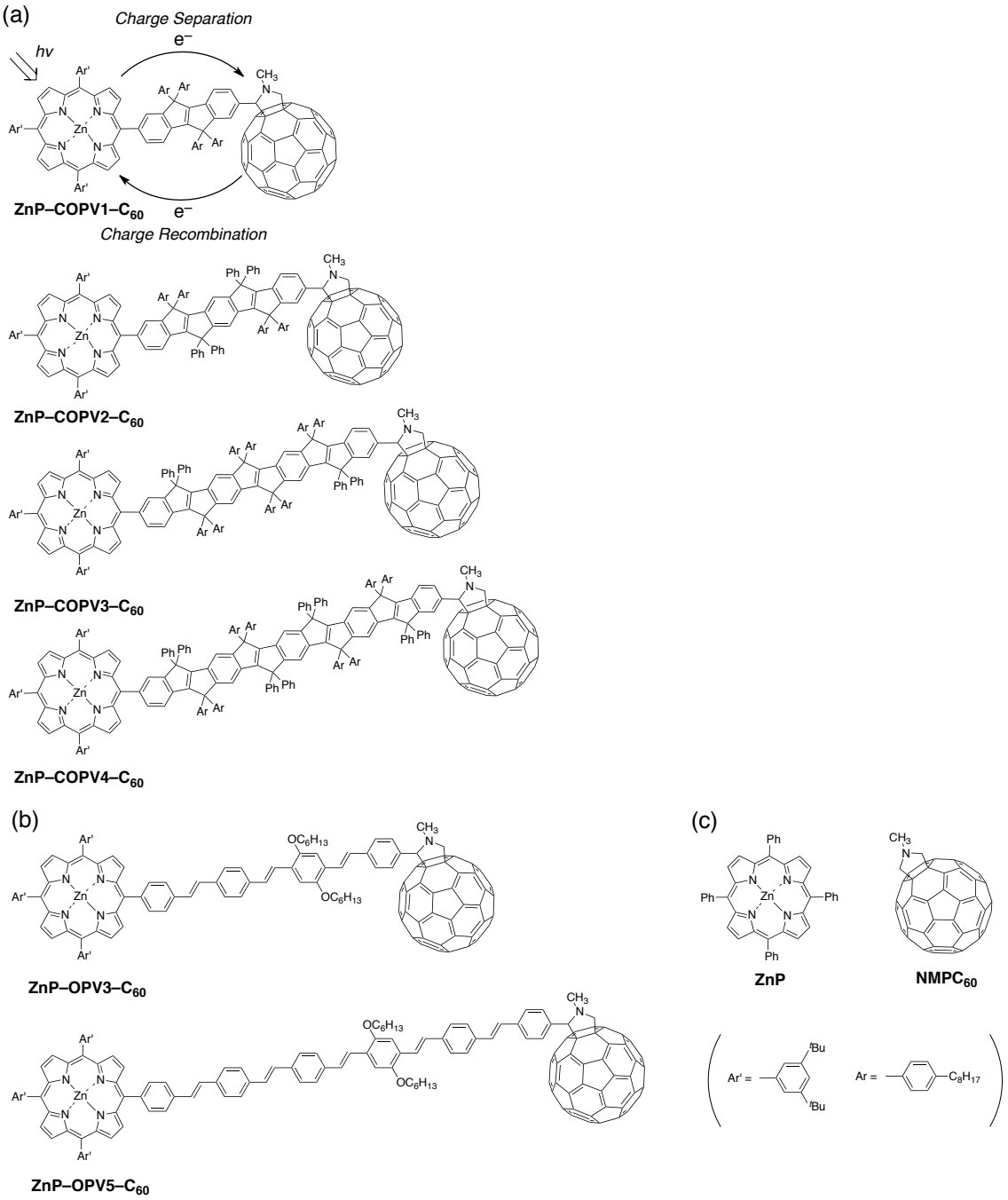

Figure 1. Structures of compounds used in this study. (a) ZnP–fullerene conjugates molecules linked by COPV. (b) ZnP–fullerene conjugates molecules linked by OPV. (c) ZnP and fullerene references.

Scheme 1 shows the synthetic route of **ZnP–COPV*n*–C$_{60}$** (*n* = 1–4). **COPV*n*** (*n* = 1–4) were synthesized according to the previously established procedure.[9, 20] Bromination using copper dibromide of **COPV*n*** proceeded

quantitatively except for $n = 4$. In the case of COPV4, the reaction was sluggish and less selective because the HOMO of COPV4 is confined in the center of the COPV core (Figure 2). The dibromide **Br–COPV*n*–Br** was lithiated by 1 equivalent of *n*-BuLi and the resulting anion was trapped by *N*,*N*-dimethylformamide (DMF) to afford the aldehyde **Br–COPV*n*–CHO**. Suzuki–Miyaura cross-coupling with zinc porphyrin boronic ester **ZnP–Bpin** (scheme 2), followed by its 1,3-dipolar cycloaddition with C_{60}[21] provided the desired compounds.

Scheme 1. Synthesis of **ZnP–COPV*n*–C_{60}**.

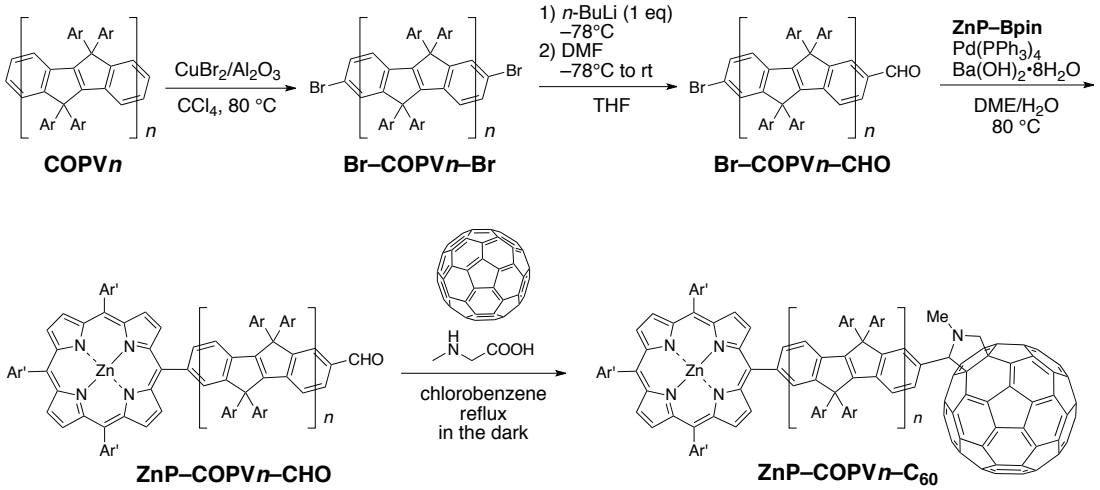

Scheme 2. Synthesis of zinc porphyrin boronic ester (**ZnP–Bpin**).

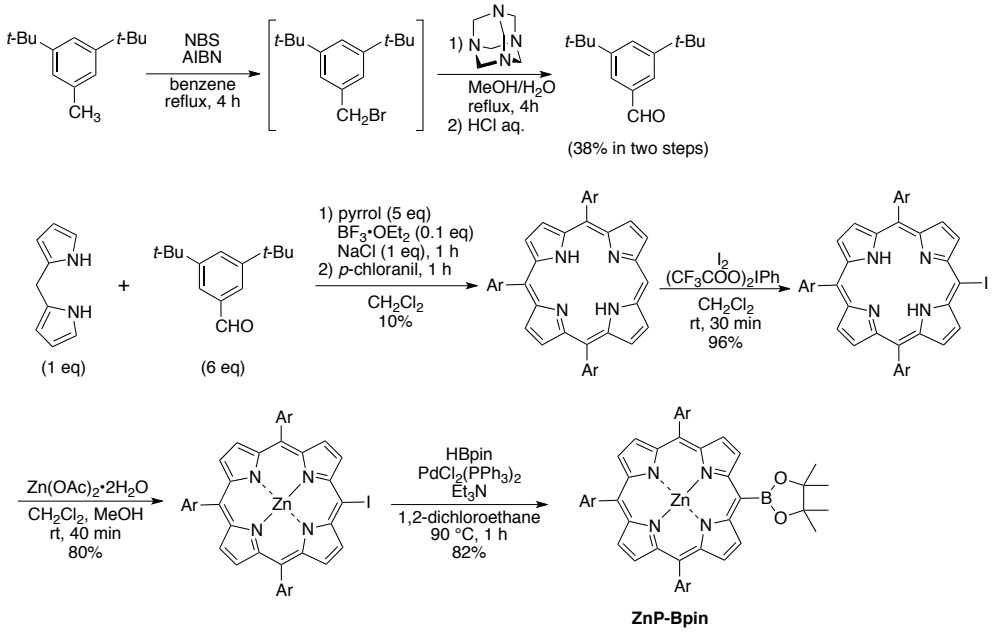

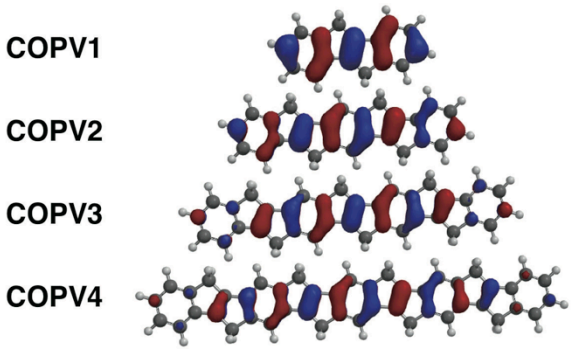

Figure 2. Kohn–Sham orbitals of **COPV*n*** (HOMO, B3LYP/6-31G*).

2-2-2. Steady-State Photophysical Properties

In the ground state, the absorption spectrum of **ZnP–COPV*n*–C_{60}** is best described as superimpositions of the different constituents, that is, ZnP, COPV, and C_{60} with a slightly disintensified and red-shifted ZnP Soret band and Q band (Figure 3 and 4a). For example, in **ZnP–COPV4–C_{60}**, the Soret band of ZnP and the COPV4 absorptions are red-shifted by 6.5 and 7.5 nm, respectively. From these findings, it can be concluded that ZnP, COPV*n*, and C_{60} are electronically isolated from each other in the ground state. In the excited state, ET from ZnP to C_{60} upon photoexcitation and energy transfer from COPV*n* to ZnP is inferred from the quenching of both ZnP and COPV*n* fluorescence. In particular, the fluorescence of ZnP and COPV upon, for example, 430 nm excitation of **ZnP–COPV4–C_{60}** in THF is strongly quenched in with quantum yields as low as 0.0022 (Figure 4b). Nevertheless, the ZnP fluorescence quantum yield (Φ_F) in **ZnP–COPV*n*–C_{60}** (n = 1–4) increases upon 550 nm excitation as the COPV length increases, with Φ_F in THF of 0.0010, 0.0025, 0.0062, and 0.0092, respectively. This trend matches that for ET, which slows down as the COPV length increases. A similar trend was observed in benzonitrile with even lower Φ_F of 0.0010, 0.0021, 0.0048, and 0.0085.

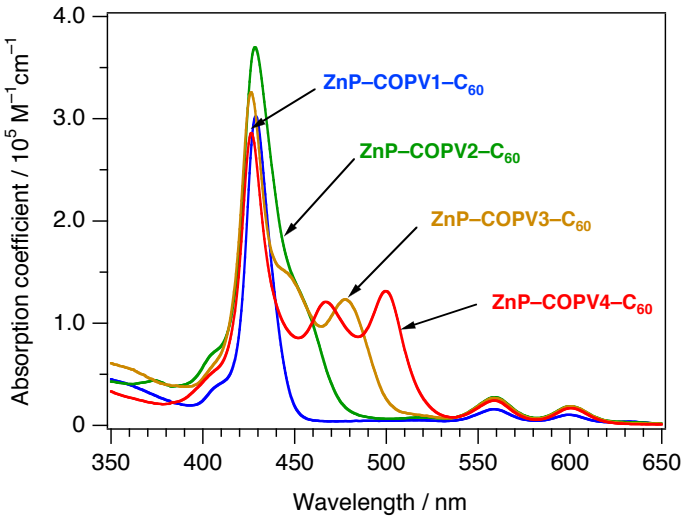

Figure 3. Steady-state photophysical properties of **ZnP–COPV*n*–C$_{60}$** in THF at room temperature.

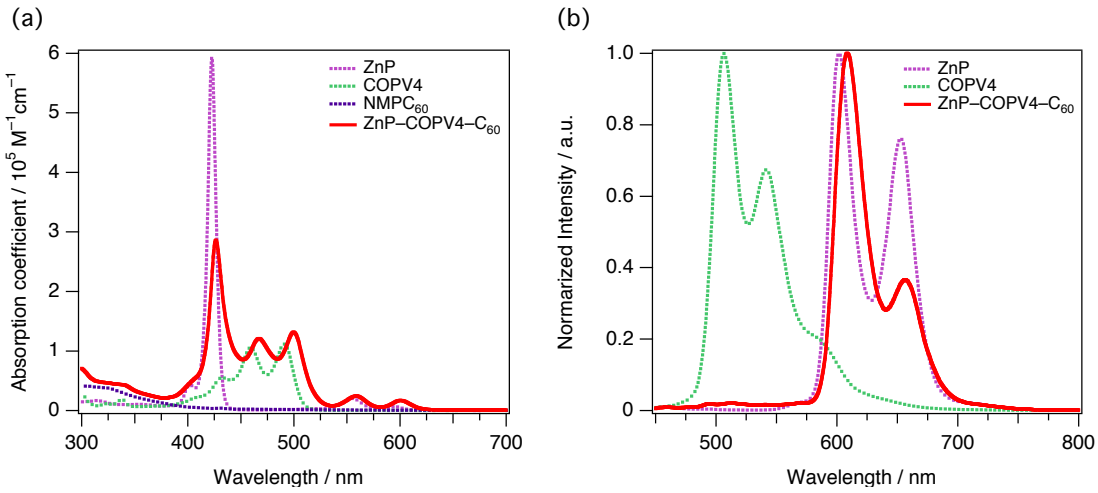

Figure 4. Steady-state photophysical properties in THF at room temperature. (a) Absorption spectra of **ZnP**, **COPV**, **NMPC$_{60}$**, and **ZnP–COPV4–C$_{60}$**. (b) Normalized fluorescence spectra of **ZnP** (Φ_F = 0.04), **COPV4** (Φ_F = 1.0), and **ZnP–COPV4–C$_{60}$** (Φ_F = 0.0022) excited at 430 nm.

2-2-3. Laser Flash Photolysis

Transient absorption measurements with **ZnP–COPV*n*–C_{60}** in benzonitrile, THF, and anisole at room temperature corroborated ET, with dynamics in the Marcus normal region and Marcus inverted region for charge separation (CS) and charge recombination (CR), respectively (Figures 5–7). Only in the latter the e–v coupling is expected to play a significant role.

Photoexcitation of **ZnP–COPV*n*–C_{60}** (*n* = 1–4) at 387 or 550 nm commences with the formation of either ZnP or COPV*n* single excited states. With respect to photoexciting COPV, any discernible features in the differential absorption spectra that are attributable to COPV-centered singlet-excited states are not noticed (Figures 5–8 vs Figure 9). This is because of the rapid transduction (< 1 ps) of singlet excited-state energy from COPV to ZnP. Here, dipole–dipole interactions funnel the excited-state energy to ZnP. With respect to photoexciting ZnP, it was noted that the contribution of ZnP single excited state that shows fingerprint absorptions at 524, 581, 560, and 615 nm early in the tests. From the latter, charge separation, for which spectroscopic evidence is based on the ZnP radical cation and the C_{60} radical anion characteristics that develop at 600–800 and 1,000 nm, respectively, evolves for **ZnP–COPV*n*–C_{60}** (*n* = 1 and 2) in THF and anisole. In contrast to the latter, the formation of **ZnP–COPV$n^{\bullet+}$–$C_{60}^{\bullet-}$** (*n* = 3 and 4) governs the excited-state dynamics in THF and anisole with the COPV radical cation absorption evolving in the 600–850 nm region and the C_{60} radical anion absorption developing at 1,000 nm. Note that the absorption spectra of the COPV radical cation species were reported in the literature.[9] Importantly, in more polar solvents such as benzonitrile, the formation of **ZnP$^{\bullet+}$–COPV*n*–$C_{60}^{\bullet-}$** (*n* = 1–4) was found to dominate the overall photoreactivity. The CS and CR rate constants and the lifetimes of COPV*n* are summarized in Table 1 and 2, respectively.

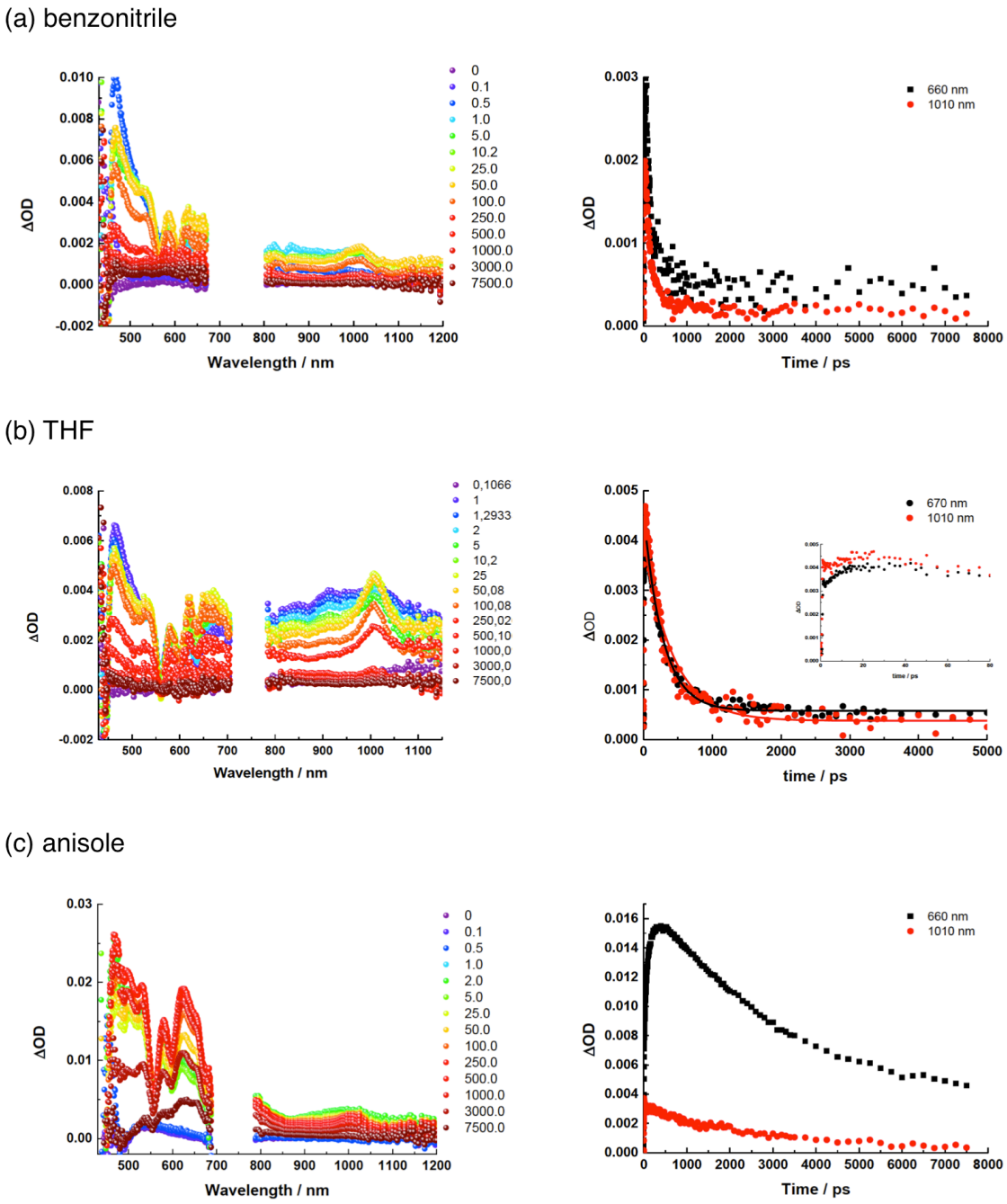

Figure 5. Differential absorption spectra of **ZnP–COPV1–C_{60}** (387 nm, 200 nJ) in argon-saturated (a) benzonitrile, (b) THF, and (c) anisole at room temperature with several time delays between 0 to 7500 ps and the time absorption profiles monitoring CS and CR dynamics.

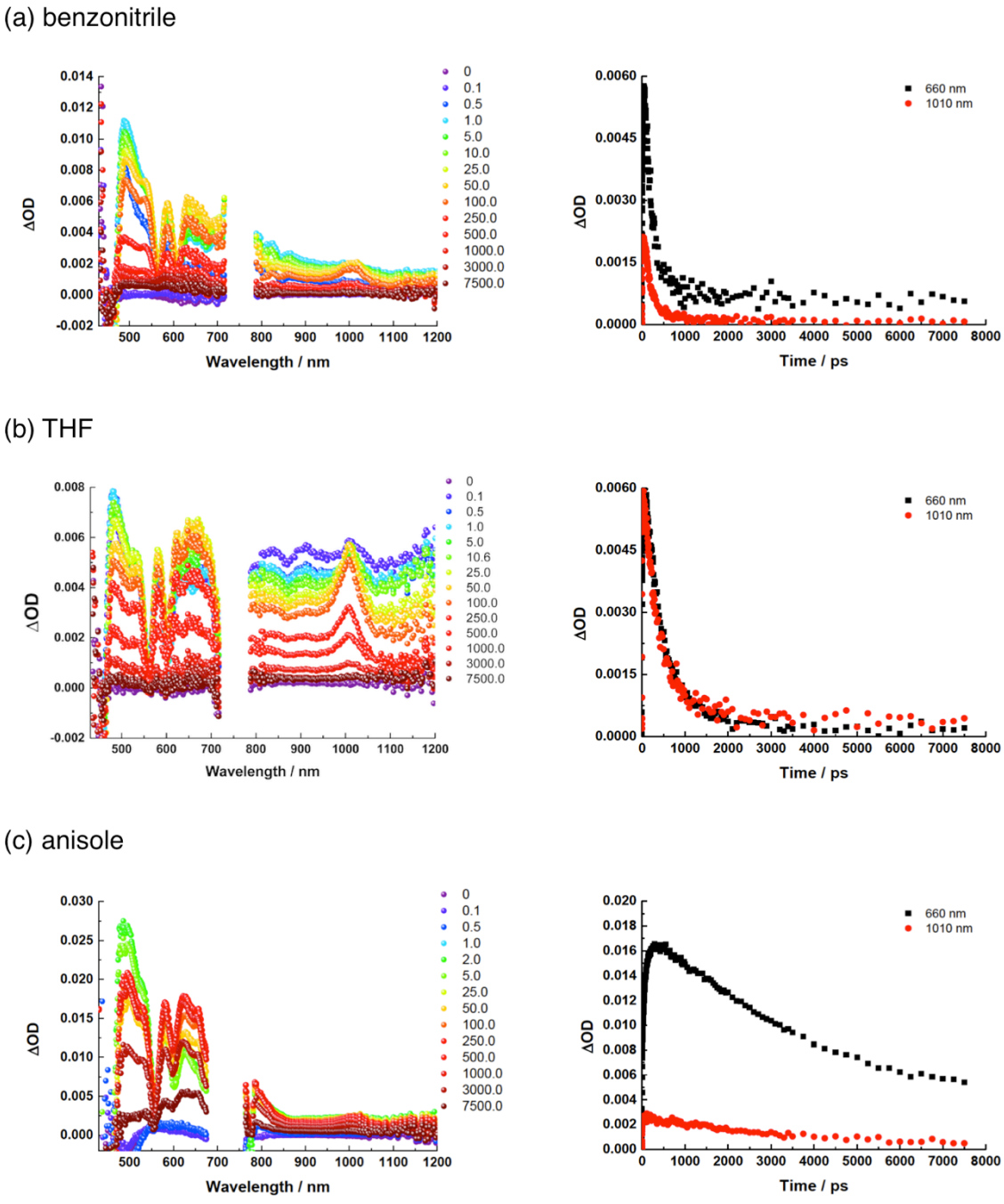

Figure 6. Differential absorption spectra of **ZnP–COPV2–C_{60}** (387 nm, 200 nJ) in argon-saturated (a) benzonitrile, (b) THF, and (c) anisole at room temperature with several time delays between 0 to 7500 ps and the time absorption profiles monitoring CS and CR dynamics.

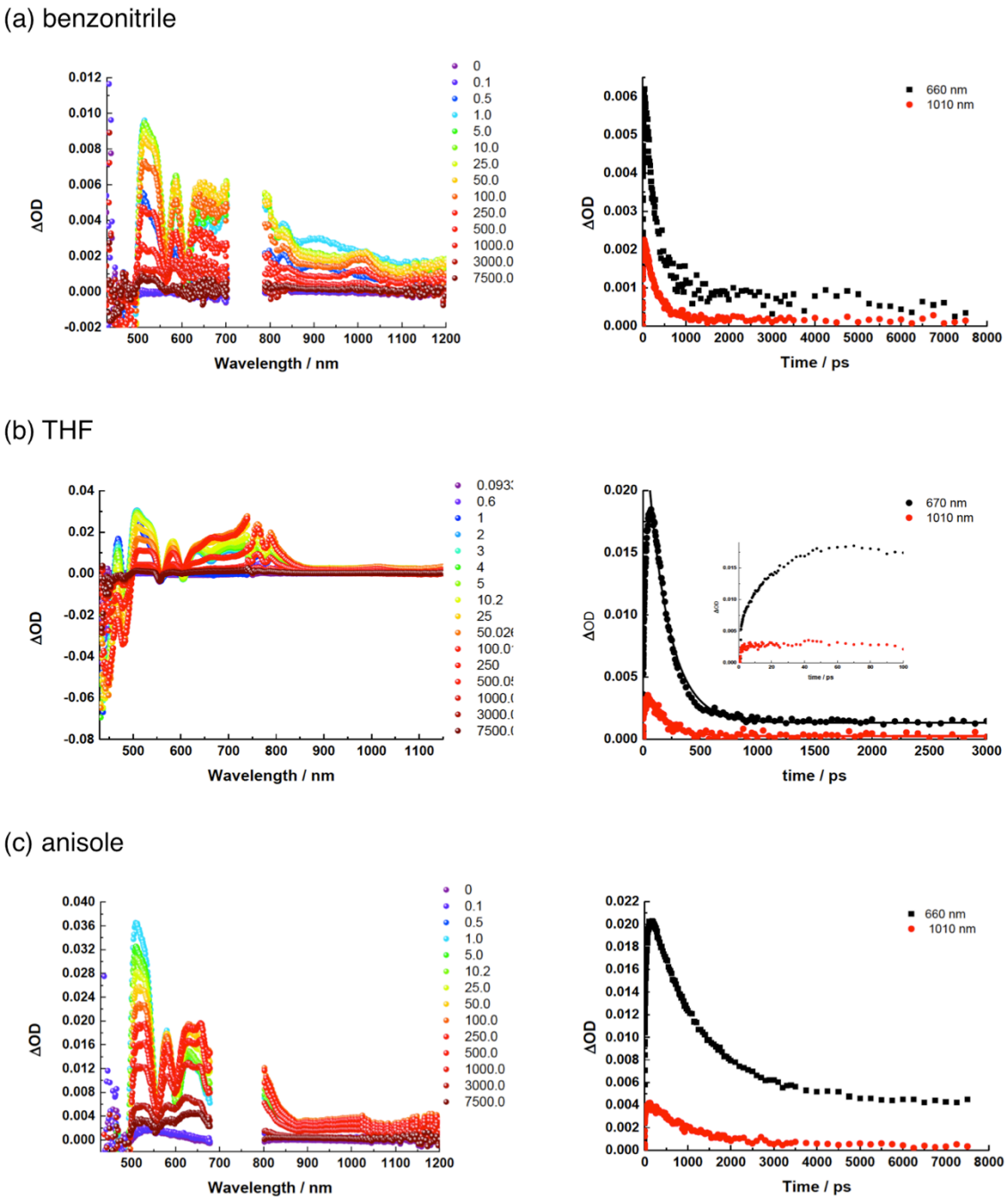

Figure 7. Differential absorption spectra of **ZnP–COPV3–C_{60}** (387 nm, 200 nJ) in argon-saturated (a) benzonitrile, (b) THF, and (c) anisole at room temperature with several time delays between 0 to 7500 ps and the time absorption profiles monitoring CS and CR dynamics.

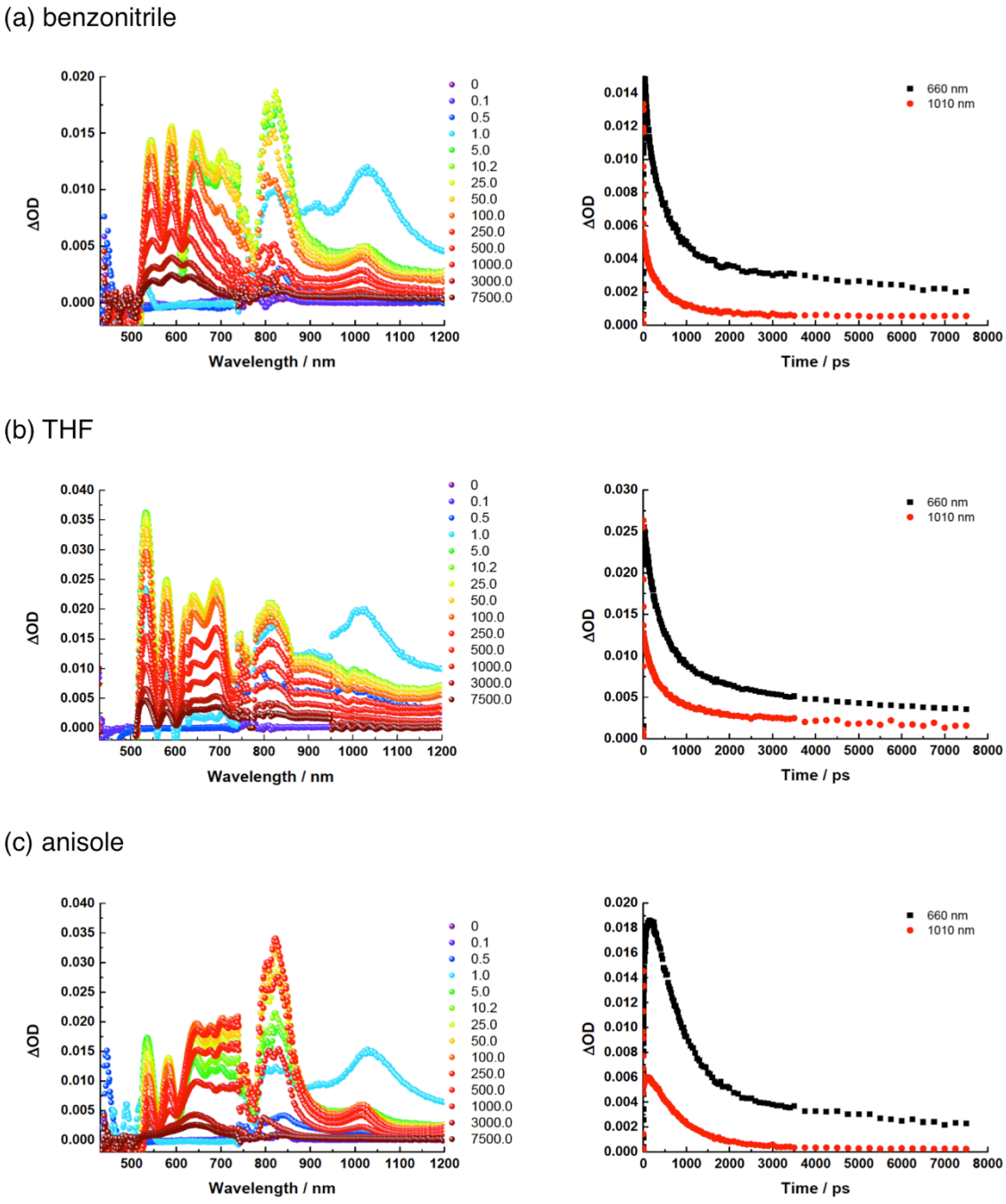

Figure 8. Differential absorption spectra of **ZnP–COPV4–C_{60}** (387 nm, 200 nJ) in argon-saturated (a) benzonitrile, (b) THF, and (c) anisole at room temperature with several time delays between 0 to 7500 ps and the time absorption profiles monitoring CS and CR dynamics.

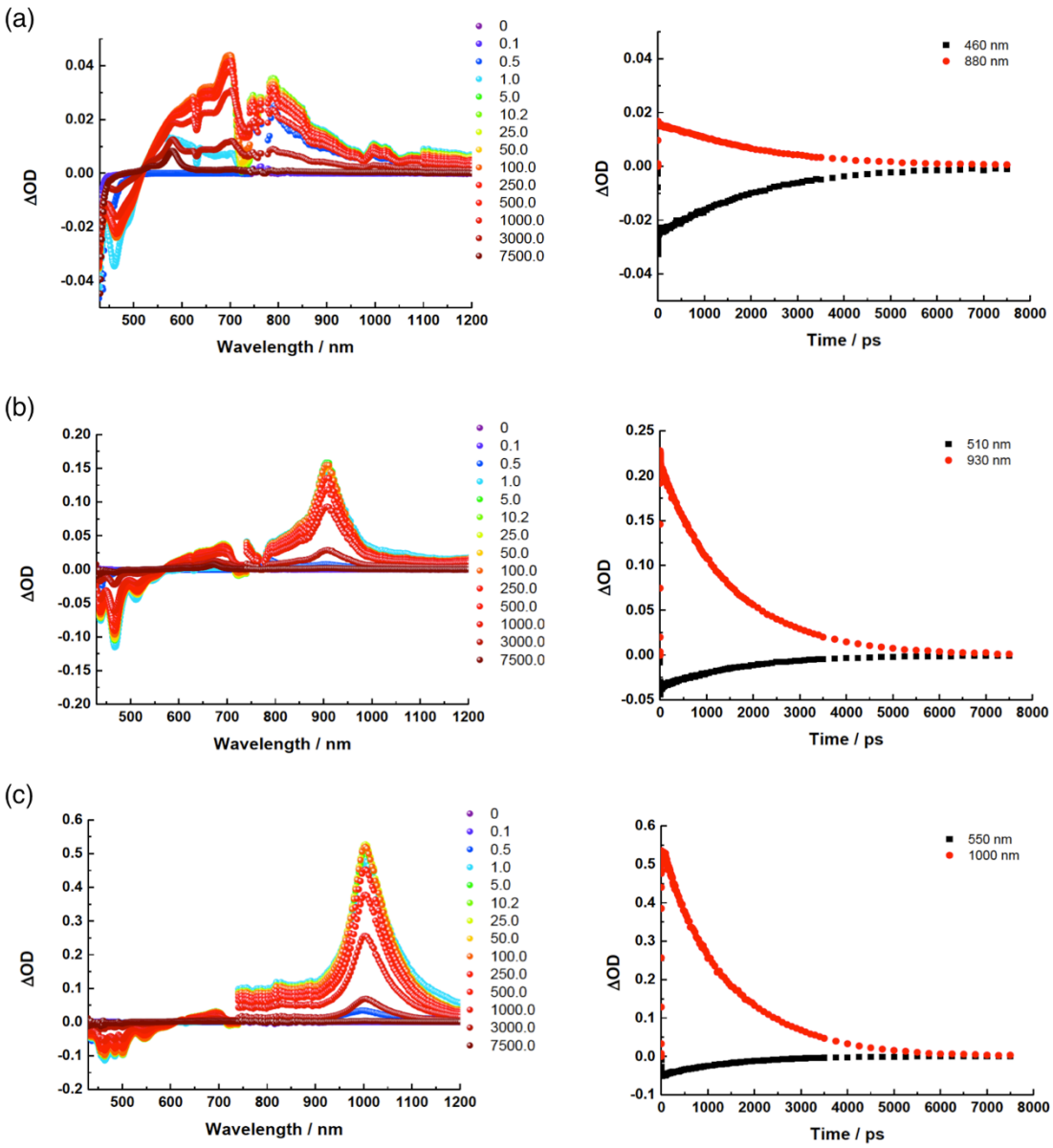

Figure 9. Differential absorption spectra of (a) **COPV2**, (b) **COPV3**, (c) **COPV4** (387 nm, 200 nJ) in THF at room temperature with several time delay between 0 to 7500 ps and the time absorption profiles monitoring the singlet excited state dynamics. Note that the differential absorption spectrum of **COPV1** could not be acquired due to the lack of absorption at 387 nm.

Table 1. Data for CS and CR in **ZnP–COPV*n*–C$_{60}$** (n = 1–4) and **ZnP–OPV*n*–C$_{60}$** (n = 3 and 5). The underlined data correspond to the **ZnP–COPV*n*$^{\bullet+}$–C$_{60}^{\bullet-}$** absorptions, which are irrelevant to the present study.

Compound	PhCN (ε_S = 25.2)		THF (ε_S = 7.53)		Anisole (ε_S = 4.33)	
	k_{CS} / s^{-1}	k_{CR} / s^{-1}	k_{CS} / s^{-1}	k_{CR} / s^{-1}	k_{CS} / s^{-1}	k_{CR} / s^{-1}
ZnP–COPV1–C$_{60}$	1.1×10^{11}	8.1×10^{9}	3.7×10^{10}	3.6×10^{9}	1.21×10^{10}	2.6×10^{8}
ZnP–COPV2–C$_{60}$	7.8×10^{10}	5.2×10^{9}	1.2×10^{11}	2.3×10^{9}	1.17×10^{10}	2.0×10^{8}
ZnP–COPV3–C$_{60}$	5.7×10^{10}	3.7×10^{9}	$\underline{7.1 \times 10^{10}}$	$\underline{5.9 \times 10^{9}}$	$\underline{2.5 \times 10^{10}}$	$\underline{1.24 \times 10^{8}}$
ZnP–COPV4–C$_{60}$	$\underline{1.2 \times 10^{11}}$	1.8×10^{9}	$\underline{2.5 \times 10^{11}}$	$\underline{4.8 \times 10^{9}}$	$\underline{4.8 \times 10^{10}}$	$\underline{1.18 \times 10^{8}}$
ZnP–OPV3–C$_{60}$ [a]	8.8×10^{9}	4.4×10^{6}	4.5×10^{9}	1.2×10^{6}	–	–
ZnP–OPV5–C$_{60}$ [a]	4.4×10^{9}	2.7×10^{6}	3.2×10^{9}	9.3×10^{5}	–	–

[a] taken from ref 13.

Table 2. Lifetimes of the singlet excited state of **COPV*n*** (n = 2–4) in argon-saturated THF.

Compound	τ / ps
COPV2	2000
COPV3	1800
COPV4	1600

2-2-4. Energy Levels

It was first verified that the desired D-to-A electron transfer occurs for **ZnP–COPV*n*–C$_{60}$** and found that only the molecules with n = 1–3 are suitable of the purpose of the present study. Thus, cyclic voltammetry of **ZnP–COPV*n*–C$_{60}$** (n = 1–3) in a polar solvent system, 1,2-dichlorobenzene(ODCB)/acetonitrile (4:1), showed reversible one-electron oxidation of ZnP moiety at 0.24 V (vs Fc^+/Fc) and COPV*n* moiety at 0.27–0.83 V, accompanied by reversible one-electron reduction of fullerene moiety at –1.13 V (Table 1). These data indicate that HOMO and LUMO of **ZnP–COPV*n*–C$_{60}$** are due to the ZnP and the fullerene moieties, respectively.

Table 3. Oxidation and reduction potentials (V vs Fc^+/Fc).

Compound	E_{ox} / V	E_{red} / V
NMPC$_{60}$ [a,c]	-	–1.20
COPV1 [a,d]	0.83	–2.67
COPV2 [a,d]	0.53	–2.58
COPV3 [a,d]	0.32	–2.51
COPV4 [a,d]	0.27	–2.42
ZnP–COPV1–C$_{60}$ [b]	0.24	–1.13
ZnP–COPV2–C$_{60}$ [b]	0.24	–1.13
ZnP–COPV3–C$_{60}$ [b]	0.24	–1.13

[a] in dichloromethane. [b] in ODCB/MeCN=4:1 (ε_S = 15.4). [c] estimated from data in reference 22 (–0.70 V vs SCE) and the oxidation potential of ferrocene (0.50 V vs SCE). [d] taken from reference 9.

The Weller's equation (equation 1)[23] provided the energy levels of the two possible charge separated states **ZnP$^{\bullet+}$–COPV*n*–C$_{60}^{\bullet-}$** and **ZnP–COPV*n*$^{\bullet+}$–C$_{60}^{\bullet-}$** that will result from the desired D-to-A ET and the undesirable B-to-A ET, respectively (Figure 10).

$$E_{IP} = E_{ox} - E_{red} - \frac{1}{4\pi\varepsilon_0}\frac{e^2}{\varepsilon_S R_{DA}} + \frac{e^2}{4\pi\varepsilon_0}\left(\frac{1}{2r_D}+\frac{1}{2r_A}\right)\left(\frac{1}{\varepsilon_S}-\frac{1}{\varepsilon'_S}\right) \quad (1)$$

where E_{ox} and E_{red} are oxidation and reduction potentials, respectively, e is the electronic charge, ε_0 is the dielectric constant of vacuum, ε_s is the static dielectric constatnt of the solvent in which the rate constants are measured, ε_s' is the dielectic constant of the solvent in which E_{ox} and E_{red} are measured, R_{DA} is the donor-acceptor center-to-center distance, and r_D and r_A are the spherical radii of donor and acceptor, respectively. R_{DA}

was estimated from the energy minized strucutre calculated using density functional theory (Figure 11).

It should be noted that Eq. 1 assumes some approximations such that the molecules can be regarded as a sphere and that the solvent behaves as dielectric continuum although it provided reasonable results in many cases in the literatures. The shapes of COPVs are far from spherical but rod-like, however, the values of the spherical radii of COPVs are not so sensitive to the energy (e.g. A 20% increase in the radius of COPV4 results in the change of the energy levels within ±2%).

Figure 10 summarizes the energies of **ZnP$^{\bullet+}$–COPV*n*–C$_{60}^{\bullet-}$** and **ZnP–COPV*n*$^{\bullet+}$–C$_{60}^{\bullet-}$** estimated by Equation 1. For **ZnP$^{\bullet+}$–COPV*n*–C$_{60}^{\bullet-}$**, the energy is nearly insensitive to the COPV length (*n*) regardless of the solvent polarity, while for **ZnP–COPV*n*$^{\bullet+}$–C$_{60}^{\bullet-}$**, the energy drops precipitously as *n* increases because of an overall increase in the dipole moment. In fact, ET between COPV and C_{60} dominates for $n = 3$ and 4 in THF ($\varepsilon_S = 7.58$) and anisole ($\varepsilon_S = 4.33$), while ET between ZnP and C_{60} governs the photoactivity for $n = 3$ and 4 in benzonitrile (PhCN, $\varepsilon_S = 24.8$). Thus, **ZnP–COPV*n*–C$_{60}$** with $n = 1$ and 2 is more suitable for probing the functions of COPV bridges.

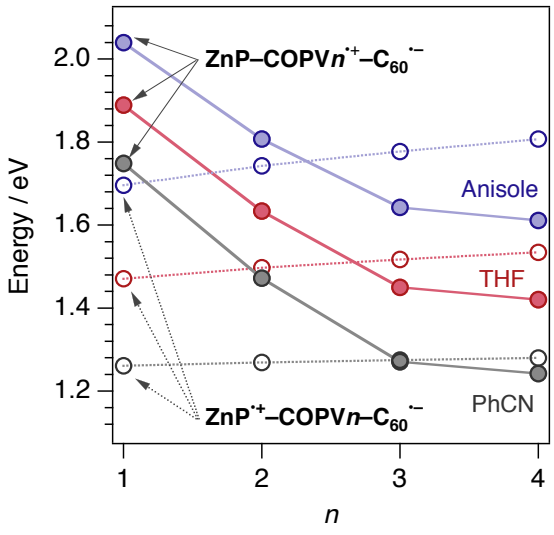

Figure 10. Stability of **ZnP$^{\bullet+}$–COPV*n*–C$_{60}^{\bullet-}$** and **ZnP–COPV*n*$^{\bullet+}$–C$_{60}^{\bullet-}$** ($n = 1$–4) in benzonitrile, THF, and anisole.

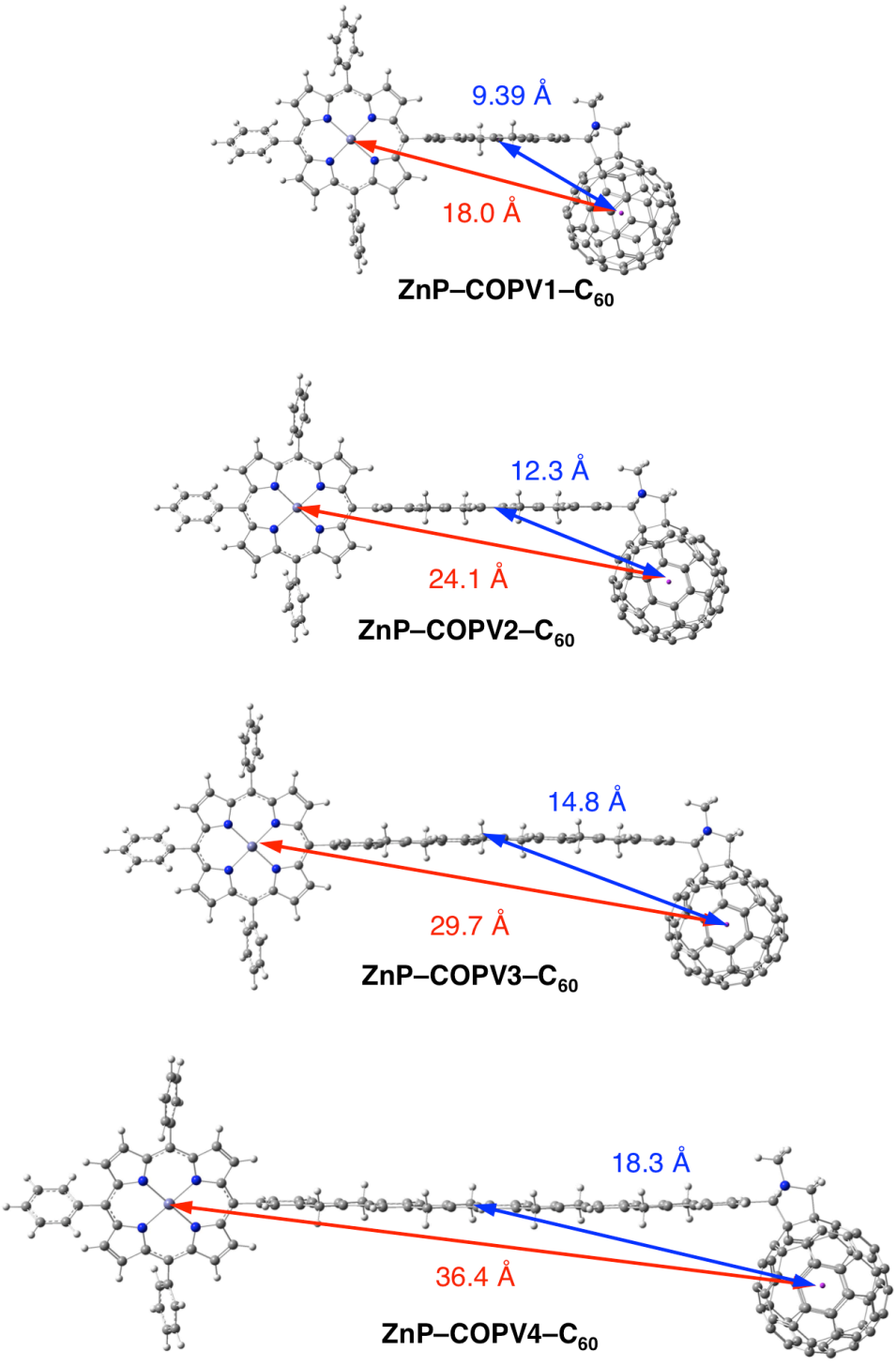

Figure 11. Molecular model of **ZnP–COPV*n*–C$_{60}$** (n = 1–4) calculated at B3LYP/6-31G* level. The substituents are omitted to reduce the calculation costs. The donor–acceptor distance (R_{DA}) and bridge–acceptor distance (R_{BA}) are measured from zinc ion to center of fullerene and the center of bridge to the center of fullerene.

Table 4. Summary of R_{BA} and r_B. The latter was estimated from the energy minimized structures of **COPV*n*** (ary groups were replaced by hydrogen atoms) calculated using density functional theory (B3LYP/6-31G* level).

Compound	R_{DA} / Å	R_{BA} / Å	r_B / Å
ZnP–COPV1–C$_{60}$	18.0	9.39	4.97
ZnP–COPV2–C$_{60}$	24.1	12.3	5.58
ZnP–COPV3–C$_{60}$	29.7	14.8	5.62
ZnP–COPV4–C$_{60}$	36.4	18.3	6.67
ZnP–OPV3–C$_{60}$	32.1	–	–
ZnP–OPV5–C$_{60}$	45.3	–	–

Table 5 and 6 summarizes the driving forces for CS ($-\Delta G^0_{CS}$) and CR ($-\Delta G^0_{CR}$) of **ZnP–COPV*n*–C$_{60}$** and **ZnP–OPV*n*–C$_{60}$** according to Equation 1–3.

$$E_{IP} = -\Delta G^0_{CR} \quad (2)$$

$$-\Delta G^0_{CS} = E_{00} - (-\Delta G^0_{CR}) \quad (3)$$

In Equation 3, E_{00} is the energy of excited state of ZnP (2.08 eV). As described above the desired charge separation occurs only for **ZnP–COPV*n*–C$_{60}$** of n = 1 and 2. The driving forces for CS were found to be positive enough in all solvents, suggesting that CS processes are thermodynamically favorable.

Table 5. $-\Delta G^0_{CS}$ and $-\Delta G^0_{CR}$ of **ZnP–COPV*n*–C$_{60}$** estimated from Weller's model.

n	E_{ox} / V	E_{red} / V	$-\Delta G^0_{CS}$ / eV			$-\Delta G^0_{CR}$ / eV		
			PhCN	THF	Anisole	PhCN	THF	Anisole
1	0.24	–1.13	0.819	0.61	0.38	1.261	1.47	1.70
2	0.24	–1.13	0.811	0.58	0.34	1.269	1.50	1.74

Table 6. $-\Delta G^0_{CS}$ and $-\Delta G^0_{CR}$ of **ZnP–OPV*n*–C$_{60}$** calculated from Weller's model. The redox potentials (V vs SCE) are taken from reference 13.

n	E_{ox} / V	E_{red} / V	$-\Delta G^0_{CS}$ / eV		$-\Delta G^0_{CR}$ / eV	
			PhCN	THF	PhCN	THF
3	0.83	–0.61	0.735	0.49	1.345	1.59
5	0.82	–0.62	0.73	0.48	1.350	1.60

2-2-5. Arrhenius Analyses

Additional insights into the CS and CR mechanisms as well as the corresponding activation barriers were gained through temperature-dependence experiments in benzonitrile. The CS and CR rate constants at different temperatures were obtained from the fluorescence quantum yields at 2.5–50 °C and femtosecond transient-absorption spectroscopy at 1.6–65 °C, respectively. The temperature dependent CS and CR rates constants are treated within the framework of the Marcus theory in terms of the thermodynamic parameters (Equation 4 and 5)[24].

$$k_{ET} = \sqrt{\frac{\pi}{\hbar^2 \lambda k_B T}} V^2 \exp\left(-\frac{\left(\Delta G^0_{ET} + \lambda\right)^2}{4\lambda k_B T} \right) \quad (4)$$

$$\Delta G^{\ddagger} = \frac{\left(\Delta G^0_{ET} + \lambda\right)^2}{4\lambda} \quad (5)$$

In equation 4 and 5, V is the electronic coupling constant, λ is the total reorganization energy, $\Delta G^{\ddagger}$ is the activation energy for the ET reaction, $\hbar$ is the Dirac constant, k_B is the Boltzmann constant, T is the thermodynamic temperature. The equation 4 was then transformed to the Arrhenius type form to estimate V, λ, and $\Delta G^{\ddagger}$.

$$\ln\left(k_{ET} T^{1/2}\right) = \ln\left(\sqrt{\frac{\pi}{\hbar^2 \lambda k_B}} V^2 \right) - \frac{\left(\Delta G^0_{ET} + \lambda\right)^2}{4\lambda k_B T} \quad (6)$$

The plotting $\ln(k_{CS}T^{1/2})$ versus T^{-1} provided the V values for CS (V_{CS}) and CR (V_{CR}) and the λ values for CS (λ_{CS}) and CR (λ_{CR}) in benzonitrile (Figure 12). The $\Delta G^{\ddagger}$ values for CS ($\Delta G^{\ddagger}_{CS}$) and CR ($\Delta G^{\ddagger}_{CR}$) were calculated according to Equation 5, which are notably smaller than the energetic differences between the LUMOs of ZnP and COPV and HOMOs of ZnP and COPV estimated by the cyclic voltammetry, which exceed 0.32 eV and 0.1 eV, respectively. Hence the electron tunneling should be the modus operandi for CS and CR. In contrast, in **ZnP–OPV3–C_{60}** an activation barrier as high as 0.2 eV suggests a thermally activated hopping mechanism.[13]

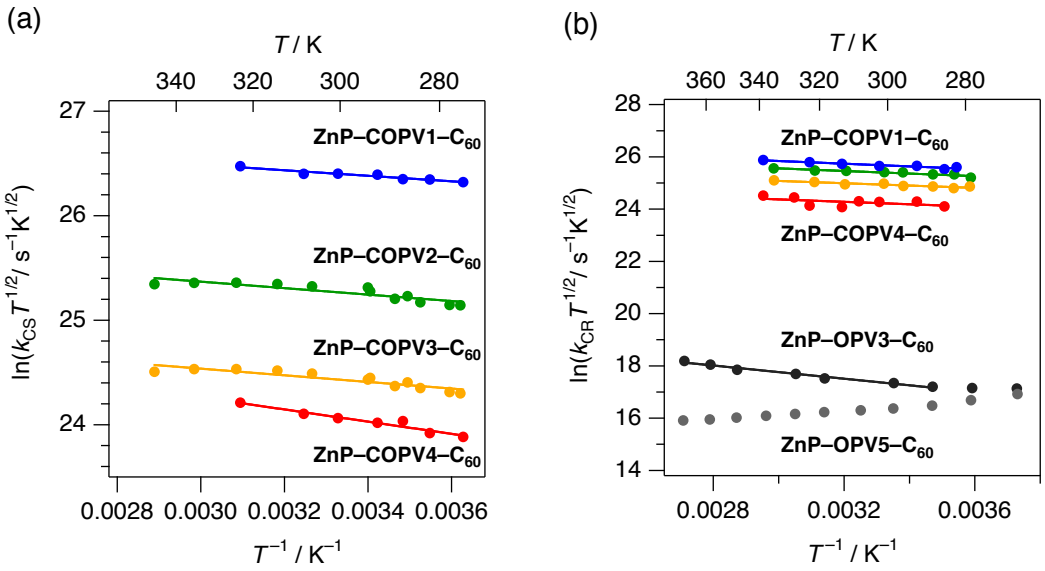

Figure 12. Arrhenius analyses of CS and CR in benzonitirle. (a) CS process. (b) CR process. The lines represent the best fit to Equation 6.

Table 7. Fitting parameters obtained in Figure 12 and the activation energy ($\Delta G^{\ddagger}$) estimated by Equation 5. The values in italic correspond to the ET from COPV*n* to C_{60}.

n	V / cm^{-1}		λ / eV		$\Delta G^{\ddagger}$ / eV	
	CS	CR	CS	CR	CS	CR
1	13.0 ± 0.7	12.8 ± 1.3	1.14 ± 0.02	0.87 ± 0.02	0.023	0.044
2	8.0 ± 0.7	10.8 ± 1.1	1.16 ± 0.03	0.88 ± 0.02	0.026	0.043
3	5.3 ± 0.4	7.9 ± 0.8	1.16 ± 0.03	0.90 ± 0.02	0.027	0.039
4	*7.1 ± 0.8*	5.8 ± 2.5	*1.31 ± 0.03*	0.90 ± 0.10	*0.028*	0.040
OPV3	–	0.66 ± 0.08	–	0.72 ± 0.01	–	0.11

2-2-6. Distance Dependence of k_{ET} and V for CS and CR in Benzonitrile

The CS and CR processes in benzonitrile show the exponential distance dependence as described in Equation 7 (Figure 13). It should be noted that hopping mechanism does not depend on an exponential law rather than on an inverse proportional law. Nevertheless, the hopping mechanism can exhibit exponential distance dependence for sufficiently long bridges.[25]

$$k_{ET} = k_0 \exp\left(-\beta R_{DA}\right) \tag{7}$$

In Equation 7, k_0 is the preexponential factor, β is the attenuation factor, and R_{DA} is the electron donor–acceptor distance. The stronger distance dependence for CR in COPVs agrees well with the proposed tunneling mechanism. Closer examination discloses that the rates at R_{DA} = 30 Å for CS ($k_{CS(30)}$) and CR ($k_{CR(30)}$) in COPVs, where the exponential approximation should be valid, with values of 5.6×10^{10} and 3.0×10^{9} s^{-1}, respectively, are larger than those for OPVs with values of 9.7×10^{9} and 4.6×10^{6} s^{-1}, respectively, by factors of 5.7 and 6.5×10^{2}. Note that the linear distance dependence of CR rate constants of π–extended tetrathiafulvalene (*ex*TTF)–OPV*n*–C_{60} conjugates with four different lengths of OPV was reported by Guldi *et al*., which verifies the fitting of the only 2 data points.[13,26]

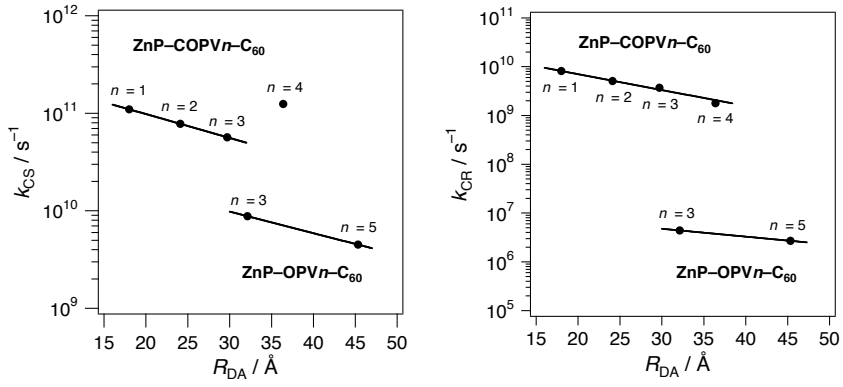

Figure 13. Rate constants versus center-to-center donor-acceptor distance in benzonitrile at room temperature. (a) CS and (b) CR. The lines represent the best fit to Equation 7.

Table 8. Fitting parameters obtained in Figure 13. Note that the β_{CR} and $k_{CR(0)}$ values in **ZnP–OPV*n*–C$_{60}$** are phenomenological due to the hopping mechanism.

Compound	CS		CR	
	$k_{CS(0)}$ / s^{-1}	β_{CS} / Å^{-1}	$k_{CR(0)}$ / s^{-1}	β_{CR} / Å^{-1}
ZnP–COPV*n*–C$_{60}$	$3.0 \pm 0.2 \times 10^{11}$	0.056 ± 0.002	$3.1 \pm 0.4 \times 10^{10}$	0.078 ± 0.006
ZnP–OPV*n*–C$_{60}$	4.5×10^{10}	0.050	1.4×10^{7}	0.036

To estimate the contribution of V on the rate enhancement, the distance dependence of V was analyzed according to the equation 8 (Figure 14). The V values at R_{DA} of 30 Å for CS ($V_{CS(30)}$) and CR ($V_{CR(30)}$) were estimated to be 5.4 and 8.0 cm^{-1}, respectively. Thus, $V_{CR(30)}$ is 1.49-times higher than $V_{CS(30)}$, which would result in a rate enhancement of 2.21, since k is proportional to V^2. The acceleration for CS at 30 Å of 5.7 is attributable to the enhancement of V, because CS is located in the Marcus normal region, where e–v coupling (S) does not have a notable impact. For CR, the 6.5 × 10^2-times rate increase cannot be rationalized solely on the basis of the 13-times increase in V. Thus, the origin of the remaining factor of 50 should be attributable to S.

$$V = V_0 \exp\left(-\frac{\beta}{2} R_{DA}\right) \tag{8}$$

Here, V_0 is the preexponential factor, β is the attenuation factor, and R_{DA} is the center-to-center donor–acceptor distance.

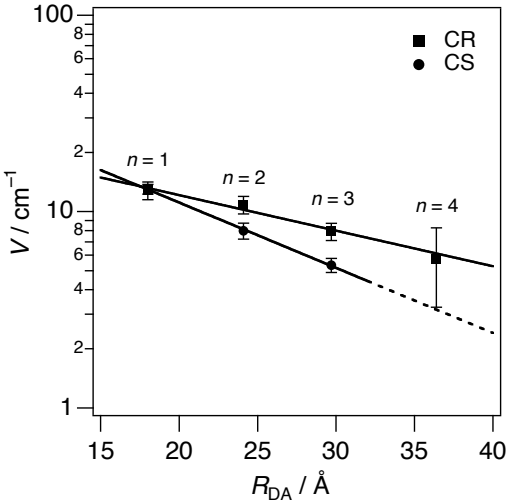

Figure 14. Distance dependence of *V* for CS and CR in benzonitrile. The lines represent the best fit to Equation 8.

Table 9. Fitting parameters obtained in Figure 14.

	V_0 / cm^{-1}	β / Å^{-1}
CS	51.3 ± 10.0	0.15 ± 0.02
CR	27.9 ± 7.8	0.083 ± 0.023

2-2-7. Marcus Plot

The plot of the ET rate (k_{ET}) versus the driving force of the ET process in different solvents ($-\Delta G^0_{ET}$) according to the classical Marcus equation (Equation 4; Figure 15) provided the strength of the electronic coupling (V = 24 ± 7 cm^{-1} for **ZnP–COPV2–C$_{60}$**) and the total reorganization energy (λ = 0.89 ± 0.04 eV for **ZnP–COPV2–C$_{60}$**). Please note that V is enhanced by the planarization as expected, however, λ became somewhat larger (V = 5 ± 3 and λ = 0.73 ± 0.05 cm^{-1} for **ZnP–OPV3–C$_{60}$**).

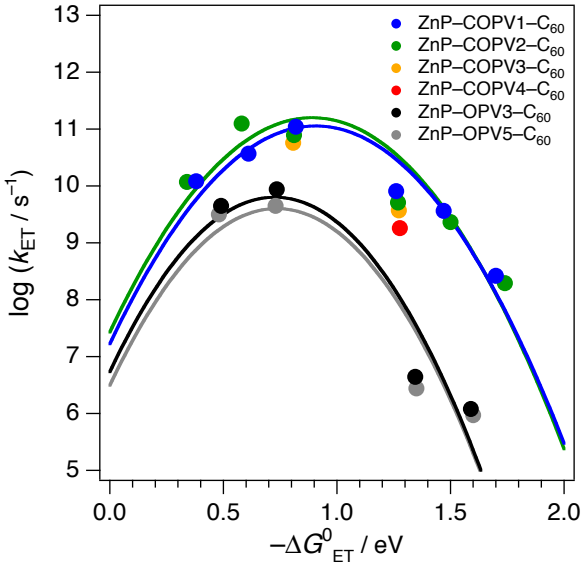

Figure 15. Fitting of the plot of the rate constants for charge separation and charge recombination versus driving force ($-\Delta G^0_{ET}$) in **ZnP–COPV*n*–C$_{60}$** (n = 1–4) and **ZnP–OPV*n*–C$_{60}$** (n = 3 and 5) according to Equation 4.

Table 10. Obtained fitting parameters corresponding to Figure 15.

Compound	λ / eV	V / cm^{-1}
ZnP–COPV1–C$_{60}$	0.90 ± 0.03	20 ± 4
ZnP–COPV2–C$_{60}$	0.89 ± 0.04	24 ± 7
ZnP–OPV3–C$_{60}$	0.73 ± 0.05	5 ± 3
ZnP–OPV5–C$_{60}$	0.74 ± 0.06	4 ± 2

To elucidate the mechanism of the unexpected increment in λ, the semi-classical Marcus equation, which divides λ into solvent reorganization energy (λ_S) and

vibrational reorganization energy (λ_V) (Equation 9 and 10)[27–29] was applied (Figure 16). It should be noted that the electron transfer parameters such as V are not so sensitive to the nature of the reaction (CS and CR) and these reactions can be adequately described by a single pair of parameters.[30]

$$k_{ET} = \sqrt{\frac{\pi}{\hbar^2 \lambda_S k_B T}} |V|^2 \sum_n^{\infty} \frac{e^{-s} S^n}{n!} \exp\left(-\frac{\left(\Delta G^0_{ET} + \lambda_S + n\hbar\omega\right)^2}{4\lambda_S k_B T} \right) \quad (9)$$

$$S = \frac{\lambda_V}{\hbar\omega} \quad (10)$$

In Equation 9 and 10, S is e–v coupling and ω relates to the averaged frequency of the coupled quantum mechanical vibration modes. The vibrational quantum $\hbar\omega$ is assumed to be 1500 cm^{-1} (0.186 eV) based on aromatic C=C stretching vibration in all cases.[31] The new data provided V = 22 ± 5 and 22 ± 4 cm^{-1} for **ZnP–COPV*n*–C$_{60}$** (n = 1 and 2), respectively. Similarly, fitting for **ZnP–OPV*n*–C$_{60}$** (n = 3 and 5) provided V = 7 ± 5 and 5 ± 4 cm^{-1}, respectively. The strong electron coupling, V, in the COPV series because of the lack of the torsional motions.

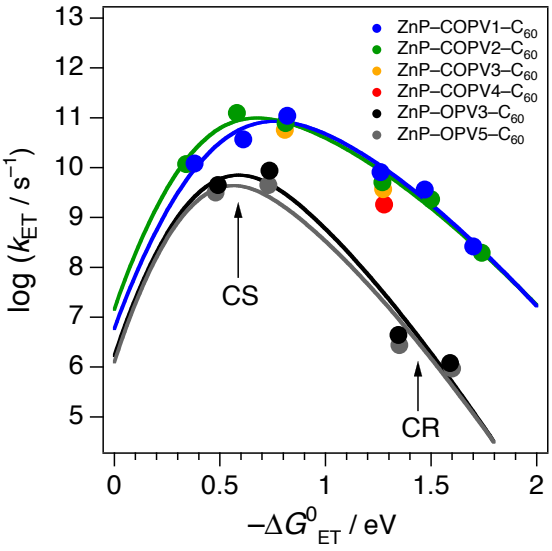

Figure 16. Driving force ($-\Delta G^0_{ET}$) dependence of k_{CS} and k_{CR} based on solvent variation. The $-\Delta G^0_{ET}$ for anisole, THF, and benzonitrile were used. The curves represent the best fit to Equation 9 with $\hbar\omega$ = 0.186 eV and T = 298 K in all cases.

Table 11. Obtained fitting parameters corresponding to Figure 16. The values in italic are the fixed parameters.

Compound	λ_S / eV	λ_V / eV	V / cm^{-1}	$S = \lambda_V/\hbar\omega$
ZnP–COPV1–C$_{60}$	0.52 ± 0.07	0.18 ± 0.06	22 ± 5	1.0 ± 0.4
ZnP–COPV2–C$_{60}$	0.42 ± 0.06	0.23 ± 0.05	22 ± 4	1.2 ± 0.3
ZnP–OPV3–C$_{60}$	0.38 ± 0.2	0.084 ± 0.10	7 ± 5	0.45 ± 0.5
ZnP–OPV5–C$_{60}$	0.36 ± 0.2	0.10 ± 0.11	5 ± 4	0.54 ± 0.6

More importantly the S values for **ZnP–COPV*n*–C$_{60}$** (n = 1 and 2) were found to be as large as 1.0 and 1.2, respectively, which are more than twice the values seen for OPVs (S = 0.45 and 0.54). This observation clearly indicates the impact of ring fusion. In particular, the bridging carbon atoms in COPVs become an active part of the skeletal vibration and increase the vibrational modes around 1,350–1,570 cm^{-1}. The enhanced e–v coupling for COPVs is in agreement with the Raman analysis of the skeletal vibration.[9] Taking the weak temperature dependence of CR and the stronger e–v coupling into account, inelastic electron tunneling, where the electron tunneling excites bridge vibrations, can be mainly responsible for the larger S and, as such, for the marked ET rate acceleration. In fact, the presence of vibrational channels decreases the activation barrier of ET to open the inelastic tunneling paths (Figure 17b). Low activation energies for inelastic tunneling account also for the lack of a mechanism crossover; namely from tunneling to the thermally activated hopping that is found in many OPVs. It should be mentioned that large e–v couplings were reported only when the donor and/or acceptor contain a functional group such as carbonyl[32] and cyano group[33], which can be highly polarized and lengthened upon the ionization.

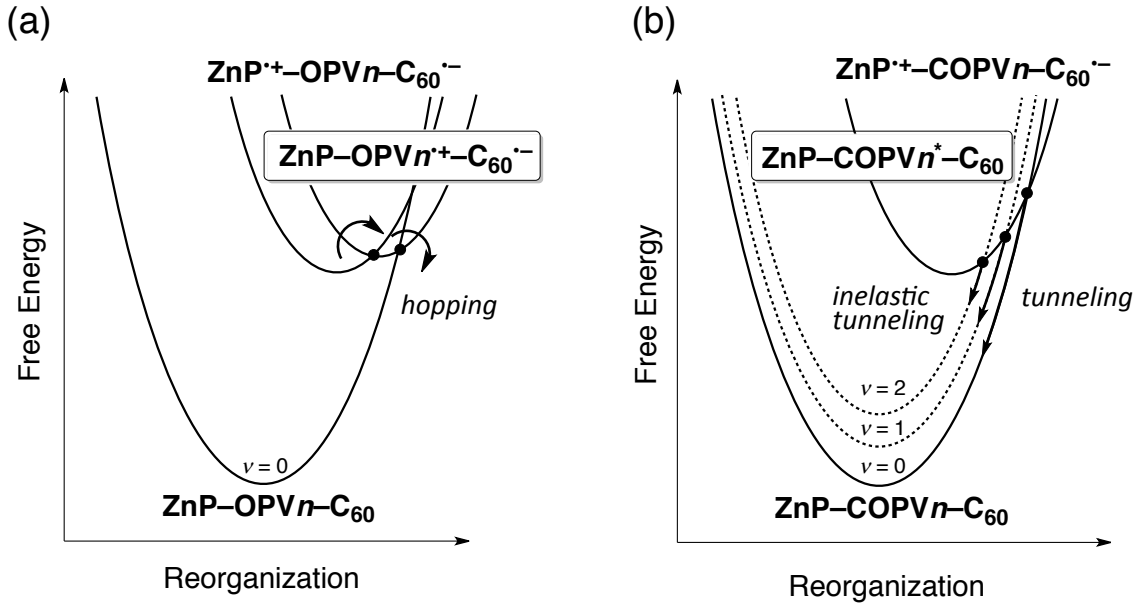

Figure 17. Reaction coordinates for CR. (a) The CR in **ZnP–OPV*n*–C$_{60}$** occurs via a hopping mechanism in which the charges reside on the bridge (**ZnP–OPV*n*$^{\bullet+}$–C$_{60}$$^{\bullet-}$**; blue). (b) The CR in **ZnP–COPV*n*–C$_{60}$** occurs via an inelastic tunneling mechanism in which the products are vibrationally excited states (**ZnP–COPV*n**–C$_{60}$**; red).

2-3. Summary

In summary, planar and rigid COPV wires transfer electrons only by means of a tunneling mechanism; that is, elastic tunneling for CS in the Marcus normal region and inelastic tunneling for CR in the inverted region. The thermally activated hopping mechanism, which is widely observed in flexible organic molecular wires, is not operative. In the inverted region, the ET process occurs with rates 6.5×10^2-times faster than in the corresponding flexible OPVs; this is because of enhanced e–v and electronic coupling. Overall, unusually strong e–v coupling, as a result of a rigid π-system, makes a major contribution and accounts for as much as a 50-times rate enhancement. Electron coupling is also enhanced through the flatness of the system, but it only accounts for a 13-times enhancement. The present study on a rationally designed π-conjugated system provides clear experimental evidence that the rigidity of the π-system strengthens e–v coupling. The strained array of two fused five-membered rings locked into the π-skeleton together with six-membered rings is undoubtedly responsible for the pronounced rigidity of the system, which is important also for the stability of polarons and photoexcited states. Inelastic electron tunneling has so far only been observed for molecular wires fixed onto substrates and at extremely low temperatures[34,35]. Thus, the emergence of this ET pathway in solution at room temperature is remarkable, suggesting that COPVs may be utilized for molecular devices operating under practically useful conditions. The COPV molecules show useful bulk properties such as high ambipolar mobility in their amorphous state and strong near-IR absorption and emission[36]. Notably, the aryl groups on COPV that carry octyl chains in the present study can be readily modified, leading to a variety of organic and inorganic functional groups and, therefore, provide a wide possibility for self-assembly and device fabrication as has already been shown in the area of dye-sensitized solar cells.[37,38] The strong e–v coupling and the resulting acceleration of CR is indeed a bottleneck for light-to-energy conversion. Nevertheless, the rapid and efficient CS is a particular asset of COPVs when used as electron donors. The e–v coupling may be controlled at atomic precision by, for example, introducing functional groups such as amines, etc. as well as by replacing carbon atoms of the bridge with heteroatoms.[39] These aspects are actively studied with the help of theoretical calculations as demonstrated in the past on the occasion of vibronic coupling density analysis.[40]

Experimental Section

General. All reactions dealing with air- or moisture-sensitive compounds were carried out in a dry reaction vessel under nitrogen or argon. The water content of the solvent was confirmed with a Karl-Fischer Moisture Titrator (MKC-210, Kyoto Electronics Company) to be less than 50 ppm. Analytical thin-layer chromatography was performed on glass plates coated with 0.25 mm 230–400 mesh silica gel containing a fluorescent indicator (Merck). Analysis with high pressure liquid chromatography (HPLC) was performed on JASCO HPLC system equipped with an ODS column (Senshu PEGASIL ODS 4.6 × 250 mm; column temperature at 40 °C). Flash silica gel column chromatography was performed on silica gel 60N (Kanto, spherical and neutral, 140–325 mesh) as described by Still. Gel permeation column chromatography (GPC) was performed on a Japan Analytical Industry LC-908 (eluent: toluene) with JAIGEL 1H and 2H polystyrene columns.

Materials. Unless otherwise noted, materials were purchased from Tokyo Kasei Co., Aldrich Inc., and other commercial suppliers and used after appropriate purification before use. Anhydrous ethereal solvents (stabilizer-free) were purchased from WAKO Pure Chemical and purified by a solvent purification system (GlassContour) equipped with columns of activated alumina and supported copper catalyst (Q-5) prior to use. All other solvents were purified by distillation and stored over molecular sieves 4Å.

Instruments. Proton nuclear magnetic resonance (^{1}H NMR) and carbon nuclear magnetic resonance (^{13}C NMR) spectra were recorded using a JEOL ECA-500 (500 MHz) or a JEOL ECX-400 (400 MHz) NMR spectrometers. Chemical data for protons are reported in parts per million (ppm, δ scale) downfield from tetramethylsilane and are referenced to the residual protons in the NMR solvent ($CDCl_3$: δ 7.26 and tetrachloroethane-d_2: δ 5.98). Carbon nuclear magnetic resonance spectra (^{13}C NMR) were recorded at 125 MHz or 100 MHz: chemical data for carbons are reported in parts per million (ppm, δ scale) downfield from tetramethylsilane and are referenced to the carbon resonance of the solvent ($CDCl_3$: δ 77.0 and tetrachloroethane-d_2: δ 73.79). The data are presented as follows: chemical shift, multiplicity (s = singlet, d = doublet, t = triplet, m = multiplet and/or multiple resonances, br = broad), coupling constant in

Hertz (Hz), and integration. Melting points of solid materials were determined on a Mel-Temp II capillary melting-point apparatus and are uncorrected. Routine mass spectra were acquired by atmospheric pressure ionization (APCI) using a quadrupole mass analyzer on Shimadzu QP-8000 or Waters ZQ-S spectrometer, and by matrix-assisted laser desorption ionization using a time-of-flight mass analyzer (MALDI-TOF) with *trans*-2-[3-(4-*tert*-butylphenyl)-2-methyl-2-propenylidene]malononitrile (DCTB) matrix. UV-vis absorption and fluorescence spectra are recorded on JASCO V-670 and FP6500 spectrometers, respectively. Cyclic voltammetry (CV) and differential pulse voltammetry (DPV) were performed on a HOKUTO DENKO HZ-5000 voltammetry analyzer. Steasy-state UV/Vis spectroscopy was performed on Lambda 2 UV/Vis spectrophotometer (Perkin–Elmer) or JASCO V-670; absorption maxima λ_{max} given in nm. Steady state fluorescence spectroscopy was performed on Horiba Jobin Yvon Fluoromax 3 or JASCO FP6500 spectrophotometer at room temperature (298 K) in a 1 to 1 cm quartz cuvette. All spectra were corrected for the instrument response. For excitation wavelength below 450 nm a cut off filter (435 nm) was inserted. Femtosecond transient absorption studies were performed with laser pulses (1 kHz, 150 fs pulse width) from an amplified Ti/sapphire laser system (Model CPA 2101, Clark-MXR Inc.; output 775 nm). For an excitation wavelength of 420 and 550 nm, a nonlinear optical parametric converter (NOPA) was used to generate ultra-short tunable visible pulses out of the pump pulses. The transient absorption pump probe spectrometer (TAPPS) is referred to as a two-beam setup, in which the pump pulse is used as excitation source for transient species and the delay of the probe pulse is exactly controlled by an optical delay rail. As the probe (white-light continuum), a small fraction of pulses stemming from the CPA laser system was focused by a 50 mm lens into a 2 mm thick sapphire disc. The transient spectra were recorded using fresh argon-saturated solutions in each laser excitation. All experiments were performed at 298 K in a 2 mm quartz cuvette. Nanosecond Laser Flash Photolysis experiments were performed with 355 or 532 nm laser pulses from a Quanta-Ray CDR Nd:YAG system (6 ns pulse width) in a front face excitation geometry.

Synthesis.

In the following molecular structures, Ar and Ar' represents 4-octylphenyl 3,5-di-*tert*-butylphenyl, respectively.

2,7-bis((2-(methoxydiphenylmethyl)phenyl)ethynyl)-5,5,10,10-tetrakis(4-octylphenyl)-5,10-dihydroindeno[2,1-*a*]indene

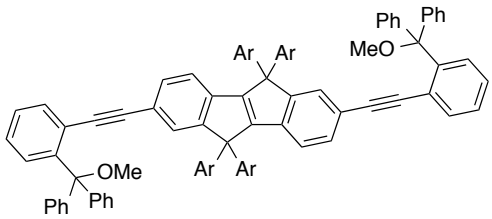

To a solution of 22 mL of THF and 11 mL of trietylamine, **I–COPV1–I**[9] (478 mg, 0.728 mmol), $PdCl_2(PPh_3)_2$ (51.0 mg, 0.0728 mmol), CuI (27.7 mg, 0.146 mmol), and ((2-ethynylphenyl)(methoxy)methylene)dibenzene (880 mg, 1.60 mmol) were added and the solution was degassed through argon for 15 min. After stirring for 7 h at 70 °C, the reaction mixture was filtered to remove the catalyst, and washed with sat. NH_4Cl aq. and dried over $MgSO_4$. Silica gel chromatography (eluent: *n*-hexane) gave the title compound (1.07 g, 0.689 mmol, 95%) as a yellow solid. Mp. 199.5–200.5 °C; ^{1}H NMR (500 MHz, $CDCl_3$) δ 0.86 (t, *J* = 6.9 Hz, 12H), 1.25–1.35 (m, 40H), 1.58–1.64 (m, 8H), 2.58 (t, *J* = 7.7 Hz, 8H), 3.01 (s, 6H), 6.80 (d, *J* = 7.4 Hz, 2H), 6.92 (s, 2H), 7.00–7.04 (m, 6H), 7.09 (d, *J* = 8.0 Hz, 8H), 7.14–7.20 (m, 18H), 7.31 (m, 2H), 7.44 (d, *J* = 7.4 Hz, 2H), 7.52 (d, *J* = 8.0 Hz, 8H), 7.86 (d, *J* = 8.0 Hz, 2H); ^{13}C NMR (125 MHz, $CDCl_3$) δ 14.1, 22.6, 29.2, 29.4, 29.5, 31.4, 31.9, 35.6, 52.0, 62.2, 86.9, 90.7, 97.5, 120.4, 120.5, 122.7, 126.8, 127.0, 127.5, 127.9, 128.0, 128.3, 129.0, 130.2, 134.8, 138.2, 139.3, 141.6, 142.1, 145.3, 156.2, 157.7; Anal. Calcd for $C_{116}H_{124}O_2$: C, 89.87; H, 8.06. Found: C, 89.71, H, 8.23.

((5,5,10,10-tetrakis(4-octylphenyl)-5,10-dihydroindeno[2,1-*a*]indene-2,7-diyl)bis(1,1-diphenyl-1*H*-indene-3,2-diyl))bis(bis(4-octylphenyl)methanol)

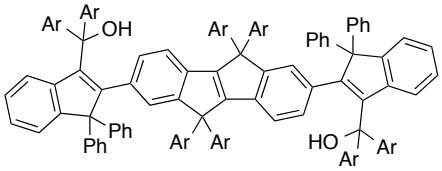

To a solution of 2,7-bis((2-(methoxydiphenylmethyl)phenyl)ethynyl-5,5,10,10-tetrakis(4-octylphenyl)-5,10-dihydroindeno[2,1-*a*]indene (1.02 g, 0.655 mmol) in 30 mL of dry THF was added LiNaph (0.200 M, 13.8 mL, 2.76 mmol) *via* syringe over 10 minutes at ambient temperature. After 1.5 h, bis(4-octylphenyl)methanone (0.582 M, 5.0 mL, 2.91 mmol) was added and sat. NH_4Cl was poured into the reaction mixture. The organic layer was washed with ethyl acetate and dried over $MgSO_4$ to give orange oil. Silica gel chromatography was performed twice (*n*-hexane/DCM = 4:1) to give the title compound (1.13 g, 0.490 mmol, 75%) as a pale yellow solid. Mp. 69.0–69.5 °C; ^{1}H NMR (500 MHz, $CDCl_3$) δ0.84–0.92 (br, 24H), 1.25–1.43 (m, 80H), 1.52–1.67 (m, 16H), 2.47 (t, *J* = 7.4 Hz, 8H), 2.55 (br, 8H), 3.09 (s, 2H), 6.35–7.12 (m, 66H); ^{13}C NMR (125 MHz, $CDCl_3$) δ 14.1, 22.7, 29.3, 29.4, 29.5, 31.4, 31.9, 35.6, 62.2, 68.4, 120.5, 121.2, 124.4, 124.7, 125.8, 126.3, 126.4, 126.9, 127.7, 128.10, 128.14, 128.3, 128.5, 131.92, 137.8, 139.9, 140.9, 142.1, 142.2, 155.0, 155.4, 155.7, 156.7; Anal. Calcd for $C_{172}H_{204}O_2$•H_2O: C, 88.99, H, 8.94. Found: C, 89.19, H, 9.01.

5,5,7,7,14,14,16,16-octakis(4-octylphenyl)-9,9,18,18-tetraphenyl-5,7,9,14,16,18-hexahydroindeno[2,1-*a*]indeno[2',1':5,6]-*s*-indaceno[2,1-*g*]-*s*-indacene (COPV3)

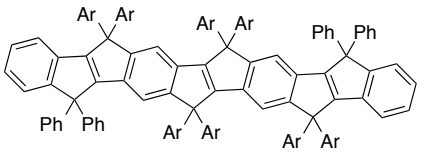

To a solution of ((5,5,10,10-tetrakis(4-octylphenyl)-5,10-dihydroindeno[2,1-*a*]indene-2,7-diyl)bis(1,1-diphenyl-1*H*-indene-3,2-diyl))bis(bis(4-octylphenyl)methanol) (920 mg, 0.406 mmol) in 40 of carbon tetrachloride was added boron trifluoride (62.2 mg, 0.440 mmol) at

ambient temperature. After 5 min, sat. NH_4Cl aq. was poured into the reaction mixture and it was extracted with chloroform three times and dried over $MgSO_4$. Purification by silica-gel chromatography afforded the title compound (807 mg, 0.356 mmol, 88%) as a yellow solid. Mp. 232.2–232.8 °C; ^{1}H NMR (500 MHz, $CDCl_3$) δ 0.87 (t, *J* = 6.9 Hz, 12H), 0.88 (t, *J* = 6.9 Hz, 12H), 1.27–1.32 (m, 80H), 1.54–1.59 (m, 16H), 2.47–2.53 (m, 16H), 6.86 (d, *J* = 8.6 Hz, 8H), 6.94 (d, *J* = 8.0 Hz, 8H), 6.99 (d, *J* = 8.6 Hz, 8H), 7.04–7.11 (m, 24H), 7.16–7.20 (m, 10H), 7.23 (s, 2H), 7.27 (s, 2H), 7.38 (d, *J* = 7.4 Hz, 2H); ^{13}C NMR (125 MHz, $CDCl_3$) δ 14.1, 22.7, 29.3, 29.5, 35.6, 31.4, 31.9, 62.2, 68.3, 120.5, 121.2, 124.3, 124.7, 125.8, 126.3, 126.4, 126.9, 127.7, 128.09, 128.14, 128.3, 128.5, 131.9, 137.7, 139.9, 140.9,142.0, 142.2, 155.0, 155.4, 155.7, 156.7; Anal. Calcd for $C_{172}H_{200}$: C, 91.11; H, 8.89. Found: C, 90.78, H, 9.01.

2,11-dibromo-5,5,7,7,14,14,16,16-octakis(4-octylphenyl)-9,9,18,18-tetraphenyl-5,7,9,14,16,18-hexahydroindeno[2,1-*a*]indeno[2',1':5,6]-*s*-indaceno[2,1-*g*]-*s*-indacene (Br–COPV3–Br)

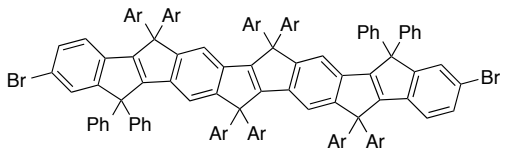

To the solution of COPV3 (576 mg, 0.245 mmol) in 15 mL of carbon tetrachloride was added $CuBr_2/Al_2O_3$ (340 mg, 1.52 mmol) under reflux for 20 h. The resulting mixture was filtered through a short pad of silica gel and evaporated to give the title compound (600 mg, 0.254 mmol, 97%) as a yellow solid. Mp. 320 °C (dec); ^{1}H NMR (500 MHz, $CDCl_3$) δ 0.88 (t, *J* = 6.9 Hz, 24H), 1.28–1.32 (m, 80H), 1.52–1.59 (m, 16H), 2.48–2.53 (m, 16H), 6.88 (d, *J* = 7.4 Hz, 8H), 6.97 (d, *J* = 8.0 Hz, 8H), 7.00 (d, *J* = 7.4 Hz, 8H), 7.05–7.06 (m, 2H), 7.10 (d, *J* = 8.0 Hz, 8H), 7.11–7.12 (m, 12H), 7.18–7.20 (m, 10H), 7.25 (s, 2H), 7.29 (s, 2H), 7.41 (d, *J* = 7.4 Hz, 2H); ^{13}C NMR (125 MHz, $CDCl_3$) δ 14.1, 22.70, 22.71, 29.33, 29.35, 29.53, 29.59, 29.68, 31.42, 31.45, 31.93, 31.97, 35.6, 62.2, 63.1, 118.0, 119.1, 121.6, 127.0, 128.0, 128.1, 128.32, 128.34, 128.38, 130.2, 137.1, 140.2, 140.5, 141.0, 141.3, 142.2, 156.6, 158.6; Anal. Calcd for $C_{172}H_{198}Br_2 \bullet H_2O$: C, 84.55; H, 8.25. Found: C, 84.76, H, 8.39.

3,14-Dibromo-7,7,11,11,18,18,22,22-octakis(*p*-octylphenyl)-5,5,9,9,16,16,20,20-octaphenyl-5,7,9,11,16,18,20,22-octahydro-di(indeno[2,1:5,6]-*s*-indaceno[2',1'-g])-*s*-indacene (Br–COPV4–Br)

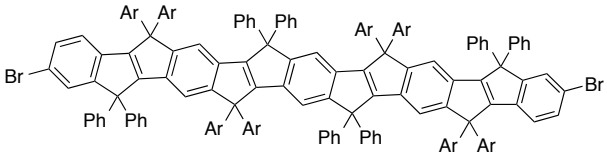

A mixture of COPV4 (237 mg, 87.8 × 10^{-3} mmol) and $CuBr_2/Al_2O_3$ (353 mg, 0.527 mmol) in CCl_4 (12 mL) was heated to reflux under argon for 20 h. The reaction was then cooled to room temperature and filtered with dichloromethane. After evaporation of the solvent, the residue was purified on silica-gel column (*n*-hexane:DCM = 10:1) to give the titled compound (59.3 mg, 20.8 × 10^{-3} mmol, 24%) as a yellow solid. Mp. 245.4–247.4 °C; ^{1}H NMR (500 MHz, $CDCl_3$) δ 0.877 (t, *J* = 7.4 Hz, 12H) 0.881 (t, *J* = 6.8 Hz, 12H), 1.27–1.31 (m, 16H), 1.49–1.56 (m, 16H), 2.47 (t, *J* = 7.8 Hz, 8H), 2.50–2.53 (m, 8H), 6.86 (d, *J* = 8.0 Hz, 8H), 6.95–6.99 (m, 16H), 7.00 (d, *J* = 8.0 Hz, 2H), 7.02–7.17 (m, 48H), 7.20 (s, 2H), 7.22 (dd, *J* = 1.8 and 8.0 Hz, 2H), 7.24 (s, 2H), 7.28 (s, 2H), 7.49 (d, *J* = 1.8 Hz, 1H). ^{13}C NMR (125 MHz, $CDCl_3$) δ 14.1, 22.7, 29.26, 29.51, 29.54, 29.6, 31.34, 31.39, 31.93, 31.95, 35.6, 62.1, 62.2, 62.7, 63.1, 117.6, 117.89, 117.94, 119.2, 121.6, 126.5, 127.0, 130.2, 135.3, 136.6, 137.0, 138.2, 140.1, 140.4, 141.1, 141.3, 142.2, 143.5, 153.5, 154.4, 155.5, 155.6, 156.0, 156.1, 156.7, 158.6; MS (APCI+) calcd for $C_{206}H_{220}Br_2^+$ $[M]^+$ 2851.56, found 2851.78; Anal. Calcd for $C_{206}H_{219}Br_2 \bullet H_2O$: C, 86.10; H, 7.79. Found: C, 85.91, H, 7.86.

7-bromo-5,5,10,10-tetrakis(*p*-octylphenyl)-5,10-dihydroindeno[2,1-*a*]indene-2-carbaldehyde (Br–COPV1–CHO)

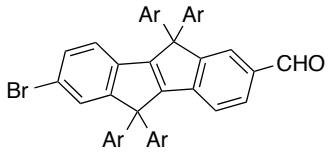

To a solution of **Br–COPV1–Br** (0.235 g, 0.210 mmol) in 2 mL of dry THF was added *n*-BuLi (1.57 M, 0.134 mL, 0.210 mmol) at –78 °C. After stirring at – 78 °C for 30 min, the mixture was stirred at ambient temperature for 30 min. The mixture was cooled to – 78 °C and DMF (0.067 mL) was added. The organic layer was washed with ethyl

acetate and dried over $MgSO_4$ to give orange oil. Silica gel chromatography (*n*-hexane:toluene = 1:1) was performed to give the title compound (0.107 g, 0.100 mmol, 48%). Mp. 170.0–171.0 °C; ^{1}H NMR (500 MHz, $CDCl_3$) δ 0.87 (t, *J* = 6.8 Hz, 12H), 1.26–1.30 (m, 40H), 1.54–1.61 (m, 8H), 2.52–2.57 (m, 8H), 7.05 (d, *J* = 8.6 Hz, 8H), 7.16 (d, *J* = 7.4 Hz, 8H), 7.56 (d, *J* = 1.1 Hz, 1H), 7.64 (d, J = 7.4 Hz, 1H), 7.91 (d, *J* = 1.2 Hz, 1H), 9.87 (s, 1H); ^{13}C NMR (125 MHz, $CDCl_3$) δ 14.1, 22.7, 29.2, 29.4, 29.5, 31.3, 31.9, 35.6, 62.5, 62.6, 120.92, 120.95, 122.6, 124.9, 128.06, 128.10, 128.49, 128.58, 128.59, 130.3, 130.8, 134.0, 136.8, 138.4, 138.6, 142.05, 142.08, 144.5, 154.7, 158.4, 159.2, 160.0, 191.8; MS (APCI+): 1064 $[M+H]^+$; Anal. Calcd for $C_{73}H_{91}BrO$: C, 82.37, H, 8.62. Found: C, 82.18, H, 8.70.

9-Bromo-7,7,14,14-tetrakis(4-octylphenyl)-5,5,12,12-tetraphenyl-5,7,12,14-tetrahydrodiindeno[2,1-*a*:2',1'-*g*]-*s*-indacene-2-carbaldehyde (Br–COPV2–CHO)

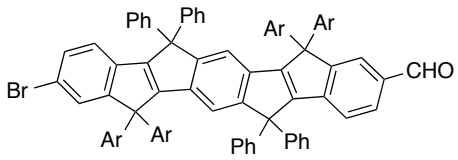

To a solution of **Br–COPV2–Br** (1.00 g, 0.647 mmol) in 40 mL of dry THF was added tetramethylethylenediamine (96.3 μmol, 0.647 mmol) and *n*-BuLi (1.66 M, 0.423 mL, 0.702 mmol) at –78 °C and stirred for 1 hour. Then DMF (0.10 mL) was added and stirred for 30 min at –78°C ant then at room temperature for 30 min. To the solution was added sat. NH_4Cl and the organic layer was washed with ethyl acetate three times and dried over $MgSO_4$. Silica gel chromatography (*n*-hexane/DCM = 3:1 to 1:2) was performed to give the title compound (0.619 g, 0.414 mmol, 64%) as a yellow solid. Mp. 229.7–230.8 °C; ^{1}H NMR (500 MHz, $CDCl_3$) δ 0.86–0.89 (m, 12H), 1.27–1.30 (m, 40H), 1.50–1.57 (m, 8H), 2.47–2.55 (m, 8H), 6.94 (d, *J* = 8.0 Hz, 4H), 6.95 (d, *J* = 8.0 Hz, 4H), 7.00 (d, *J* = 8.6 Hz, 1H), 7.06 (d, *J* = 8.0 Hz, 4H), 7.08 (d, *J* = 8.0 Hz, 4H), 7.15–7.22 (m, 21H), 7.23–7.24 (m, 1H), 7.28 (s, 1H), 7.32 (t, *J* = 5.2 Hz, 1H), 7.51 (d, *J* = 1.7 Hz, 1H), 7.62 (dd, *J* = 1.2 and 8.0 Hz, 1H), 7.89 (d, *J* = 1.7 Hz, 1H) 9.84 (s, 1H); ^{13}C NMR (125 MHz, $CDCl_3$) δ 14.1, 22.7, 29.2, 29.49, 29.53, 29.6, 31.27, 31.28, 31.90, 31.91, 35.57, 35.58, 62.51, 62.58, 62.8, 62.9, 118.1, 118.7, 119.7, 120.4, 121.6, 124.9, 126.87, 126.94, 128.07, 128.11, 128.14, 128.2, 128.3, 128.36, 128.39, 128.43, 128.44,

128.46, 128.46, 128.61, 130.9, 133.6, 136.0, 138.8, 139.1, 141.7, 141.8, 142.7, 142.8, 145.1, 153.3, 154.1, 156.2, 156.4, 157.0, 158.0, 159.2, 161.0, 191.8; Anal. Calcd for $C_{107}H_{113}BrO$: C, 85.97, H, 7.62. Found: C, 85.93, H, 7.71.

11-bromo-5,5,7,7,14,14,16,16-octakis(4-octylphenyl)-9,9,18,18-tetraphenyl-5,7,9,14,16,18-hexahydroindeno[2,1-*a*]indeno[2',1':5,6]-*s*-indaceno[2,1-*g*]-*s*-indacene-2-carbaldehyde (Br–COPV3–CHO)

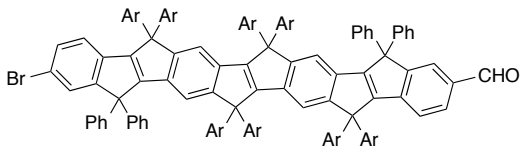

To a solution of **Br–COPV3–Br** (0.121 g, 50.0×10^{-3} mmol) in 2.5 mL of dry THF was added *n*-BuLi (1.56 M, 38.5 μL, 60.1×10^{-3} mmol) at –78 °C are stirred for 30 min and then DMF (40 μL) was added. After stirring at room temperature for 2 h, the reaction mixture was quenched with sat. NH_4Cl aq. The organic layer was washed with water and brine and dried over $MgSO_4$. Purification by silica gel chromatography (*n*-hexane/DCM = 10:1) provided the title compound (44.3 mg, 18.6×10^{-3} mmol, 27%) as a yellow solid. Mp. 340 °C (dec); ^{1}H NMR (500 MHz, $CDCl_3$) δ 0.89–0.91 (m, 24H), 1.25-1.40 (m, 80H), 1.54-1.62 (m, 16H), 2.50-2.56 (m, 16H), 6.90 (d, *J* = 8.6 Hz, 11H), 6.99–7.10 (m, 35H), 7.12–7.17 (m, 18H), 7.19–7.23 (m, 10H), 7.25–7.28 (m, 3H), 7.29–7.32 (m, 4H), 7.53 (d, *J* = 1.7 Hz, 1H), 7.66 (dd, *J* = 1.1 and 8.0 Hz, 1H), 7.91 (s, 1H), 9.87 (s, 1H). ^{13}C NMR (125 MHz, $CDCl_3$) δ 14.3, 22.85, 22.87, 29.48, 29.51, 29.68, 29.75, 29.83, 31.59, 31.61, 31.67, 32.09, 32.11, 35.8, 62.30, 62.31, 62.37, 62.41, 63.20, 63.27, 118.1, 118.2, 118.7, 119.4, 120.7, 121.8, 124.9, 127.1, 127.2, 128.19, 128.28, 128.36, 128.44, 128.87, 128.49, 128.54, 128.60, 130.4, 131.4, 133.5, 135.0, 135.6, 137.1, 138.2, 138.3, 140.1, 140.4, 140.5, 140.6, 141.2, 141.3, 141.5, 141.7, 142.0, 142.4, 145.8, 153.5, 153.8, 155.1, 155.97, 156.55, 156.19, 156.64, 156.81, 157.49, 158.7, 160.9, 191.9.

13-Bromo-7,7,11,11,18,18,22,22-octakis(*p*-octylphenyl)-5,5,9,9,16,16,20,20-octaphenyl-5,7,9,11,16,18,20,22-octahydro-di(indeno[2,1:5,6]-*s*-indaceno[2',1'-g])-*s*-indacene-2-carbaldehyde (Br–COPV4–CHO)

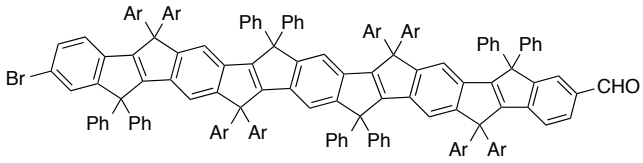

To a solution of **Br–COPV4–Br** (43 mg, 15.0×10^{-3} mmol) in 2 mL of dry THF was added *n*-BuLi (1.59 M, 12 μL, 19.1×10^{-3} mmol) at –78 °C are stirred for 1 h and then DMF (2 μL, 29×10^{-3} mmol) was added. After stirring at room temperature for 1 h, the reaction mixture was quenched with sat. NH_4Cl aq. The organic layer was washed with water and brine and dried over $MgSO_4$. Purification by silica gel chromatography (*n*-hexane:DCM = 10:1 to 1:1) provided the title compound (20 mg, 7.1×10^{-3} mmol, 48%) as a orange solid. The compound was used to next reaction without characterization.

ZnP–COPV1–CHO

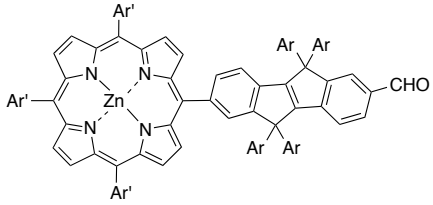

To a solution of **Br–COPV1–CHO** (62.1 mg, 58.4×10^{-3} mmol) and **ZnP–Bpin** (65.6 mg, 61.6×10^{-3} mmol) in 16.0 mL of dimethoxyethane and 4.0 mL of water was added $Ba(OH)_2 \bullet 8H_2O$ (92.0 mg, 0.292 mmol). The solution was degassed through argon for 15 min and then $Pd(PPh_3)_4$ (6.7 mg, 5.80×10^{-3} mol) was added. After being stirred for 3 h at 80 °C, the reaction mixture was allowed to cool to room temperature and the organic phase was washed with water three times and dried over $MgSO_4$. After evaporation, the residue was subjected to silica gel chromatography (*n*-hexane/DCM = 5:1) and GPC (toluene) to give the title compound (28.0 mg, 14.6×10^{-3} mmol, 25%) as a purple solid. ^{1}H NMR (500 MHz, $CDCl_3$) δ 0.84 (t, *J* = 6.4 Hz, 6H), 0.89 (t, *J* = 6.4 Hz, 6H), 1.25–1.41 (m, 44H), 1.542 (s, 36H), 1.546 (s, 18H) 1.65–1.72 (m, 4H), 2.56 (t, *J* = 8.0 Hz, 4H), 2.66 (t, *J* = 8.0 Hz, 4H), 7.12 (d, *J* = 8.0 Hz, 4H), 7.23 (d, *J* = 8.0 Hz, 4H), 7.42–

7.46 (m, 9H), 7.61 (d, J = 7.4 Hz, 1H), 7.74 (d, J = 8.0 Hz, 1H), 7.79-7.80 (m, 3H), 8.05–8.06 (m, 2H), 8.08–8.09 (m, 6H), 8.42 (s, 1H), 8.92 (d, J = 4.6 Hz, 2H), 8.95 (d, J = 4.6 Hz, 2H), 8.97-8.99 (m, 4H), 9.95 (s, 1H); ^{13}C NMR (125 MHz, $CDCl_3$) δ 14.09, 14.13, 22.62, 22.67, 29.20, 29.27, 29.37, 29.50, 29.56, 31.30, 31.36, 31.74, 31.84, 31.90, 35.00, 35.01, 35.56, 35. 67, 62.7, 62.9, 119.5, 120.55, 120.63, 120.9, 122.2, 122.3, 125.0, 128.35, 128.45, 128.50, 128.7, 131.8, 131.9, 132.0, 132.1, 133.8, 134.4, 136.8, 139.7, 141.8, 142.0, 142.1, 145. 2, 145.2, 148.4, 149.9, 150.1, 150.28, 150.33, 155.2, 156.8, 158.6, 160.4, 192.0.

ZnP–COPV2–CHO

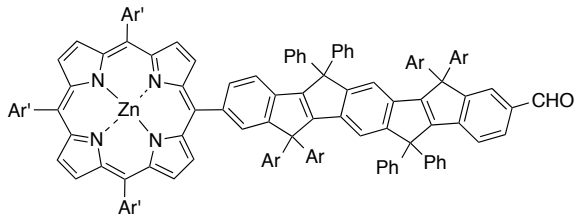

To a solution of **Br–COPV2–CHO** (34.5 mg, 22.9 × 10^{-3} mmol) and **ZnP–Bpin** (24.4 mg, 22.9 × 10^{-3} mmol) in 4.0 mL of dimethoxyethane and 0.5 mL of water was added $Ba(OH)_2$•$8H_2O$ (36.3 mg, 0.115 mmol). The solution was degassed through argon for 15 min and then $Pd(PPh_3)_4$ (2.6 mg, 2.3 × 10^{-3} mol) was added. After being stirred for 1 h at 80 °C, the reaction mixture was allowed to cool to room temperature and filtered through a pad of silica gel. After evaporation, the residue was subjected to silica gel chromatography to give **ZnP–COPV2–CHO** (39.6 mg, 16.8 × 10^{-3} mmol, 73%). ^{1}H NMR (500 MHz, $CDCl_3$) δ 0.84 (t, J = 6.8 Hz, 6H), 0.90 (t, J = 6.8 Hz, 6H), 1.23–1.34 (m, 40H), 1.517 (s, 36H), 1.522 (s, 18H) 2.48 (t, J = 7.7 Hz, 4H), 2.54 (t, J = 7.7 Hz, 4H), 6.97 (d, J = 8.0 Hz, 4H), 7.02 (d, J = 8.0 Hz, 4H), 7.17 (d, J = 8.0 Hz, 4H), 7.24–7.27 (m, 5H), 7.29–7.38 (m, 13H), 7.44–7.46 (m, 6H), 7.55 (d, J = 7.4 Hz, 1H), 7.64 (dd, J = 2.3 and 8.0 Hz, 1H), 7.77-7.79 (m, 3H), 7.94 (d, J = 1.1 Hz 1H), 8.00 (dd, J = 1.1 and 8.0 Hz, 1H), 8.06–8.07 (m, 6H), 8.35 (d, J = 1.2 Hz, 1H), 8.90 (d, J = 9.6 Hz, 2H), 8.96 (d, J = 9.6 Hz, 2H), 8.99 (s, 4H), 9.87 (s, 1H); ^{13}C NMR (125 MHz, $CDCl_3$) δ 14.1, 14.2, 22.6, 22.7, 29.2, 29.3, 29.4, 29.5, 29.57, 29.59, 31.30, 31.34, 31.7, 31.87, 31.94, 35.0, 35.58, 35.63, 62.5, 62.6, 62.9, 63.2, 118.2, 120.6, 121.2, 122.4, 124.9, 126.89, 126.93, 128.2, 128.30, 128.33, 128.38, 128.44, 128.48, 128.51, 128.8, 129.54, 129.59,

129.68, 129.70, 129.72, 132.0, 132.1, 132.2, 135.8, 137.7, 138.0, 138.9, 140.1, 141.4, 141.81, 141.83, 142.9, 143.5, 145.2, 148.4, 148.5, 150.1, 150.2, 150.3, 153.1, 155.0, 156.0, 156.5, 156.7, 157.0, 158.0, 191.8; MS (APCI+): 2349.70 $[M]^+$.

ZnP–COPV3–CHO

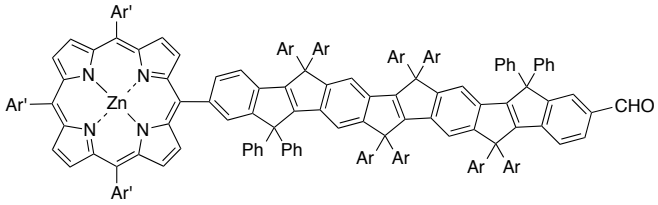

A mixture of **Br–COPV3–CHO** (41.3 mg, 17.6×10^{-3} mmol) was dissolved in 2.5 mL of dimethoxyethane and 0.6 mL of water. **ZnP–Bpin** (20.7 mg, 19.4×10^{-3} mmol) and $Ba(OH)_2 \bullet 8H_2O$ (27.7 mg, 87.8×10^{-3} mmol) was added and the solution was degassed through argon for 10 min. $Pd(PPh_3)_4$ (2.0 mg, 1.73×10^{-3} mmol) was added and the solution was heated at 80 °C for 21 hours. Purification by silica gel chromatography (*n*-Hexane:Dichloromethane = 4:1 to 2:1) afforded the title compound (45.5 mg, 14.1×10^{-3} mmol, 80%) as a purple solid. ^{1}H NMR (400 MHz, $CDCl_3$): δ 0.87–0.91 (m, 24H), 1.29–1.44 (m, 80H), 1.52 (s, 54H), 1.58-1.67 (m, 16H), 2.50–2.56 (m, 12H), 2.62 (t, *J* = 8.0 Hz, 4H), 6.88–7.43 (m, 59H), 7.57 (d, *J* = 8.0 Hz, 1H), 7.64 (d, *J* = 7.6 Hz, 1H), 7.78 (s, 3H), 8.00 (d, *J* = 8.0 Hz, 1H), 8.06-8.15 (m, 5H), 8.36 (s, 1H), 8.91 (d, *J* = 4.8 Hz, 2H), 8.96–8.98 (m, 6H), 9.84 (s, 1H); ^{13}C NMR (100 MHz, $CDCl_3$) δ 14.31, 14.33, 22.88, 22.89, 22.92, 29.51, 29.54, 29.71, 29.77, 29.78, 29.81, 29.86, 29.90, 29.95, 31.64, 32.11, 32.12, 32.15, 32.17, 32.20, 35.19, 35.84, 35.95, 62.40 (two peaks are overlapped), 62.46, 62.77, 63.24, 63.34, 118.19, 118.21, 120.86, 120.92, 121.53, 122.53, 122.57, 124.92, 126.93, 127.27, 127.69, 128.24, 128.27, 128.39, 128.43, 128.49, 128.53, 128.55, 128.64, 128.77, 128.83, 129.72, 129.75, 129.83, 129.90, 132.26, 133.52, 134.43, 134.96, 136.32, 136.96, 138.41, 138.55, 138.98, 139.49, 140.04, 140.20, 140.68, 140.71, 140.75, 140.78, 141.02, 141.19, 141.23, 141.32, 141.46, 141.65, 142.01, 142.07, 142.09, 143.39, 145.83, 148.65, 150.36, 150.40, 150.51, 153.48, 154.70, 154.91, 155.61, 156.20, 156.24, 156.26, 156.76, 156.93, 157.54, 157.55, 161.02, 191.92; MS (MALDI-TOF): 3228.96 $[M]^+$.

ZnP–COPV4–CHO

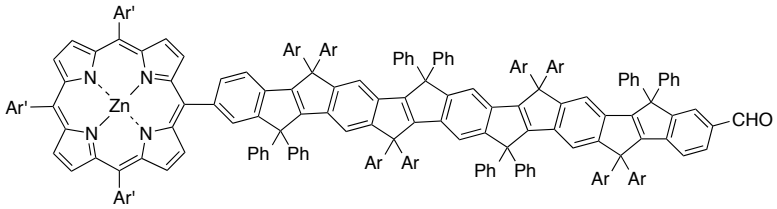

A mixture of **Br–COPV4–CHO** (20 mg, 7.1 × 10^{-3} mmol) was dissolved in 2.4 mL of dimethoxyethane and 0.6 mL of water. **ZnP–Bpin** (8 mg, 7.5 × 10^{-3} mmol) and $Ba(OH)_2$•$8H_2O$ (11 mg, 0.035 mmol) was added and the solution was degassed through argon for 10 min. $Pd(PPh_3)_4$ (0.76 mg, 0.66 × 10^{-3} mmol) was added and the solution was heated at 80 °C for overnight. Purification by silica gel chromatography (*n*-Hexane:Dichloromethane = 6 : 1 to 2 : 1) afforded the title compound. The compound was used to next reaction without characterization.

ZnP–COPV1–C_{60}

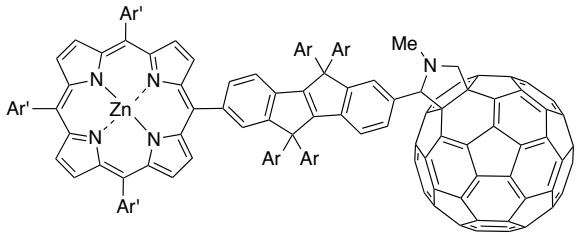

A solution of **ZnP–COPV1–CHO** (28.0 mg, 14.6 × 10^{-3} mmol), C_{60} (52.6 mg, 73.0 × 10^{-3} mmol), and sarcosine (26.0 mg, 0.292 mmol) in distilled chlorobenzene (8.0 mL) was degassed through argon for 10 min and then heated under reflux in the dark. After being stirred for 4 h, the reaction mixture was allowed to cool to room temperature. After evaporation, the residue was subjected to silica gel chromatography (CS_2 only to hexane/toluene = 2:1 to 1:1) to give the title compound (24.6 mg, 9.96 × 10^{-3} mmol, 63%) as a dark purple solid. ^{1}H NMR (500 MHz, $C_2D_2Cl_4$, 373 K) δ 0.86–0.92 (m, 12H), 1.28–1.33 (m, 40H), 1.57 (s, 54H), 1.61–1.71 (m, 8H), 2.53 (t, *J* = 8.0 Hz, 2H), 2.57 (t, *J* = 6.8 Hz, 2H), 2.61 (t, *J* = 6.8 Hz, 2H), 2.66 (t, *J* = 8.0 Hz, 2H), 2.87 (s, 3H), 4.42 (d, *J* = 9.2 Hz, 1H), 4.92 (d, *J* = 9.2 Hz, 1H), 4.96 (s, 1H), 7.03 (d, *J* = 8.0 Hz, 2H), 7.08 (d, *J* = 7.4 Hz, 2H), 7.13– 7.15 (m, 4H), 7.36–7.40 (d, *J* = 8.0 Hz, 1H), 7.50 (d, *J* = 7.4 Hz, 1H), 7.63 (br, 1H), 7.83 (s, 3H), 7.97 (d, *J* = 7.4 Hz, 1H), 8.01 (s, 1H), 8.08 (s, 6H),

8.37 (s, 1H), 8.88 (s, 4H), 8.98 (s, 4H); ^{13}C NMR (125 MHz, $CDCl_3$, 293 K) δ 14.15, 14.20, 22.65, 22.71, 29.24, 29.27, 29.31, 29.40, 29.55, 29.57, 29.59, 29.71, 31.23, 31.76, 31.88, 31.94, 35.02, 35.58, 35.67, 62.61, 62.77, 68.41, 83.23, 118.82, 120.61, 120.70, 121.42, 122.35, 122.40, 127.52, 127.54, 128.22, 128.27, 128.37, 128.46, 128.49, 128.66, 129.03, 129.55, 129.60, 129.66, 129.71, 131.85, 132.04, 132.10, 132.16, 133.91, 134.20, 134.23, 136.19, 136.27, 137.63, 138.84, 139.08, 139.21, 139.26, 139.84, 140.20, 140.39, 140.95, 141.09, 141.36, 141.45, 141.49, 141.54, 141.67, 141.69, 141.76, 141.88, 141.92, 142.08, 142.11, 142.18, 142.69, 143.80, 144.05, 144.26, 144.45, 144.64, 144.77, 145.02, 145.14, 145.34, 145.42, 145.68, 145.90, 146.11, 146.46, 146.58, 148.43, 148.46, 150.16, 150.20, 150.30, 152.91, 153.13, 153.18, 155.89, 156.21 (some peaks are overlapping); MS (MALDI-TOF) calcd for $C_{197}H_{167}N_5Zn$ $[M]^+$ m/z (%) 2668.26 (100), found 1948.59 $[M–C_{60}]^+$, 2668.41 $[M]^+$.

ZnP–COPV2–C_{60}

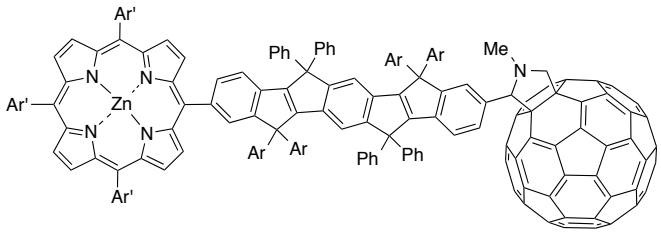

A solution of compound **ZnP–COPV2–CHO** (21.6 mg, 9.18×10^{-3} mmol), C_{60} (33 mg, 45.8×10^{-3} mmol), and sarcosine (16.4 mg, 0.184 mmol) in distilled chlorobenzene (5.0 mL) was degassed through argon for 15 min and then heated under reflux in the dark. After being stirred for 4 h in the dark, the reaction mixture was allowed to cool to room temperature. After evaporation, the residue was subjected to silica gel chromatography (CS_2 only to hexane/toluene = 2:1 to 1:1) and GPC (toluene) to give **ZnP–COPV2–C_{60}** (25.1 mg, 8.10×10^{-3} mmol, 88%). ^{1}H NMR (400 MHz, $C_2D_2Cl_4$, 393 K) δ 0.87–0.88 (m, 6H), 0.93–0.96 (m, 6H), 1.30–1.35 (m, 40H), 1.56 (s, 36H), 1.57 (s, 18H), 2.54–2.60 (m, 8H), 2.79 (s, 3H), 4.05 (m, *J* = 8.4 Hz, 1H), 4.76 (d, *J* = 8.4 Hz, 1H), 4.79 (s, 1H), 6.90–7.44 (m, 35H), 7.54 (d, *J* = 7.4 Hz, 1H), 7.83 (s, 3H), 7.90 (br, 1H), 8.01 (d, *J* = 8.0 Hz, 1H), 8.09 (m, 6H), 8.38 (s, 1H), 8.88–8.91 (m, 4H), 8.99 (s, 4H); ^{13}C NMR (100 MHz, $C_2D_2Cl_4$, 393 K) δ 13.66, 13.75, 22.27, 22.31, 22.37, 28.85, 28.95, 29.09,

29.17, 29.22, 29.25, 29.29, 29.33, 30.61, 30.67, 31.57, 31.67, 34.76, 35.28, 62.55, 62.72, 63.23, 118.30, 120.58, 120.64, 122.17, 125.13, 126.32, 126.45, 127.89, 127.98, 128.07, 128.16, 128.29, 128.38, 128.43, 128.59, 128.84, 129.35, 131.66, 131.69, 131.75, 131.78, 133.86, 135.20, 135.26, 136.12, 136.30, 138.09, 138.69, 139.38, 139.46, 139.48, 139.78, 139.83, 140.86, 140.89, 141.03, 141.34, 141.45, 141.67, 141.70, 141.78, 141.84, 141.89, 142.14, 143.00, 143.02, 143.32, 143.65, 143.73, 143.90, 144.17, 144.26, 144.58, 144.68, 144.81, 144.92, 145.35, 145.52, 145.83, 146.74, 148.52, 150.09, 150.24, 150.26, 150.30 (some peaks are overlapping); MS (MALDI-TOF) calcd for $C_{231}H_{189}N_5Zn$ $[M]^+$ m/z (%) 3098.43 (100), 2378.66 $[M–C_{60}]^+$, 3098.50 $[M]^+$

ZnP–COPV3–C_{60}

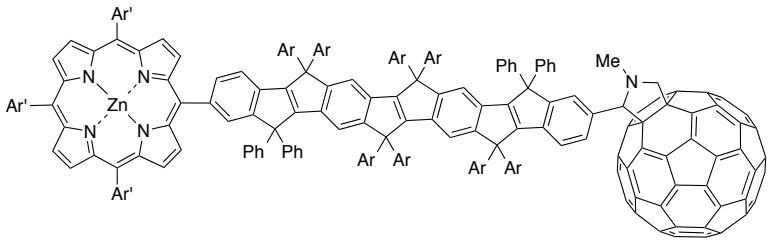

A solution of compound **ZnP–COPV3–CHO** (44.8 mg, 13.9×10^{-3} mmol), C_{60} (49.7 mg, 69.0×10^{-3} mmol), and sarcosine (24.4 mg, 0.274 mmol) in distilled chlorobenzene (7.7 mL) was degassed through argon for 20 min and then heated under reflux in the dark. After being stirred for 5 h in the dark, the reaction mixture was allowed to cool to room temperature. After evaporation, the residue was subjected to silica gel chromatography (CS_2 only to hexane/toluene = 4:1 to 1:1) to give **ZnP–COPV3–C_{60}** (32.1 mg, 8.06×10^{-3} mmol, 58%). ^{1}H NMR (400 MHz, $C_2D_2Cl_4$, 408 K) δ 0.92–0.96 (m, 24H), 1.35–1.42 (m, 80H), 1.58 (s, 54H), 1.65–1.76 (m, 16H), 2.52–2.59 (m, 12H), 2.68 (t, *J* = 7.2 Hz, 4H), 2.81 (s, 3H), 4.13 (d, *J* = 9.6 Hz, 1H), 4.83 (d, *J* = 9.6 Hz, 1H), 4.86 (s, 1H), 6.86–7.60 (m, 59H), 7.84 (s, 3H), 7.91 (s, 1H), 8.04 (d, *J* = 8.0 Hz, 1H), 8.10 (m, 6H), 8.39 (s, 1H), 8.90 (d, *J* = 4.8 Hz, 2H), 8.92 (d, *J* = 4.8 Hz, 2H), 8.98 (s, 4H); ^{13}C NMR (100 MHz, $C_2D_2Cl_4$, 393 K) δ 13.65, 13.69, 22.29, 22.31, 22.33, 22.35, 28.95, 28.98, 29.18, 29.20, 29.23, 29.26, 29.32, 29.35, 29.36, 29.38, 30.68, 30.73, 30.77, 30.80, 30.81, 31.56, 31.59, 31.62, 31.65, 34.76, 35.30, 35.37, 35.40, 35.45, 39.44, 62.25, 62.27, 62.28, 62.69, 63.26, 63.33, 68.67, 77.57, 83.45, 92.10, 92.12, 118.05, 118.16,

118.33, 118.60, 120.60, 120.64, 121.06, 122.18, 126.40, 126.48, 127.27, 127.68, 127.70, 127.72, 127.93, 128.06, 128.21, 128.26, 128.29, 128.46, 128.47, 128.53, 129.32, 129.38, 131.48, 131.57, 131.73, 131.81, 133.71, 135.19, 135.29, 135.55, 135.78, 136.09, 136.29, 136.98, 138.43, 138.68, 139.45, 139.47, 139.54, 139.65, 139.81, 140.07, 140.18, 140.27, 140.33, 140.35, 140.37, 140.51, 140.54, 140.58, 140.74, 140.76, 140.88, 141.21, 141.36, 141.38, 141.42, 141.63, 141.65, 141.67, 141.71, 141.79, 141.84, 141.88, 142.00, 142.11, 142.16, 142.34, 142.53, 142.68, 143.00, 143.65, 143.92, 144.17, 144.28, 144.59, 144.63, 144.71, 144.82, 144.84, 144.90, 144.97, 144.98, 145.33, 145.36, 145.45, 145.50, 145.54, 145.62, 145.74, 145.82, 145.83, 145.97, 146.53, 146.69, 146.75, 148.55, 148.56, 150.11, 150.25, 150.29, 150.32, 153.15, 153.32, 153.64, 154.48, 154.70, 155.30, 155.40, 155.47, 156.06, 156.13, 156.44, 156.57, 156.76, 156.85, 157.25 (some peaks are overlapping); MS (MALDI-TOF) calcd for $C_{297}H_{275}N_5Zn$ $[M]^+$ m/z (%) 3978.11 (100), found 3257.78 $[M–C_{60}]^+$, 3978.16 $[M]^+$.

ZnP–COPV4–C_{60}

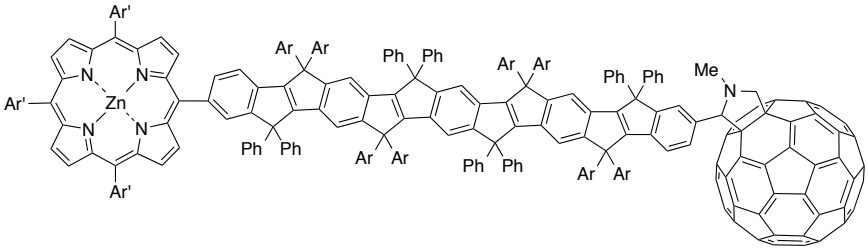

A solution of compound **ZnP–COPV4–CHO** (17 mg, 4.6×10^{-3} mmol), C_{60} (52 mg, 0.072 mmol), and sarcosine (7 mg, 0.078 mmol) in distilled chlorobenzene (7 mL) was degassed through argon for 20 min and then heated under reflux in the dark. After being stirred for 5 h in the dark, the reaction mixture was allowed to cool to room temperature. After evaporation, the residue was subjected to silica gel chromatography (CS_2 only to hexane/toluene = 4:1 to 1:1) to give the titled compound. ^{1}H NMR (500 MHz, $CDCl_3$): δ 0.86–0.89 (m, 24H), 1.28–1.38 (m, 80H), 1.50 (s, 54H), 1.54 (s, 12H), 1.60–1.71 (m, 4H), 2.48 (t, *J* = 7.8 Hz, 12H), 2.61 (t, *J* = 7.8 Hz, 4H), 2.70 (br, 3H), 4.14 (d, *J* = 8.0 Hz, 1H), 4.83–4.86 (m, 2H), 6.86–7.22 (m, 69H), 7.29–7.31 (m, 6H), 7.33 (s, 1H), 7.36 (s, 1H), 7.39–7.40 (m, 4H), 7.53 (d, *J* = 7.4 Hz, 1H), 7.77 (s, 3H), 7.99 (d, *J* = 7.4 Hz, 1H), 8.04–8.05 (m, 6H), 8.32 (s, 1H), 8.88 (d, *J* = 4.6 Hz, 2H), 8.95 (d, *J* = 4.6 Hz, 2H),

8.96 (s, 4H); ^{13}C NMR was not obtained due to an insufficient amount of sample; MS (MALDI-TOF) calcd for $C_{331}H_{297}N_5Zn$ $[M]^+$ m/z (%) 4408.28 (100), found 4407.89 $[M]^+$.

Quantum Calculation

All calculations were performed by Gaussian 09 program and the analyses were performed by GaussView 5. The structures of the molecules were simplified to reduce the computational costs.

Fitting Procedure

The fitting of the semi-classical Marcus equation was performed using Igor Pro 5.03 software.

References

1 Daizadeh, I., Medvedev, E. S. & Stuchebrukhov, A. A. Effect of protein dynamics on biological electron transfer. *Proc. Natl. Acad. Sci. USA* **94,** 3703–3708 (1997).

2 Nozik, A. J. *et al*. Semiconductor quantum dots and quantum dot arrays and applications of multiple exciton generation to third-generation photovoltaic solar cells. *Chem. Rev*. **110,** 6873–6890 (2010).

3 Ellingson, R. J. *et al*. Highly efficient multiple exciton generation in colloidal PbSe and PbS quantum dots. *Nano Lett*. **5,** 865–871 (2005).

4 Leturcq, R. *et al*. Franck-Condon blockade in suspended carbon nanotube quantum dots. *Nature Physics* **5,** 327–331 (2009)

5 Bostwick, A., Ohta, T., Seyller, T., Horn, K. & Rotenberg, E. Quasiparticle dynamics in graphene. *Nature Physics* **3,** 36–40 (2006).

6 van der Lit, J. *et al*. Suppression of electron–vibron coupling in graphene nanoribbons contacted via a single atom. *Nature Communications* **4,** 1–6 (2013).

7 Prezhdo, O. V. Photoinduced dynamics in semiconductor quantum dots: Insights from time-domain ab initiostudies. *Acc. Chem. Res*. **42,** 2005–2016 (2009).

8 Long, R. & Prezhdo, O. V. Ab initio nonadiabatic molecular dynamics of the ultrafast electron injection from a PbSe quantum dot into the TiO_2 surface. *J. Am. Chem. Soc*. **133,** 19240–19249 (2011).

9 Zhu, X., Tsuji, H., López-Navarrete, J. T., Casado, J. and Nakamura, E., Carbon-bridged oligo(phenylenevinylene)s: stable π-systems with high responsiveness to doping and excitation, *J. Am. Chem. Soc*. **134**, 19254–19259 (2012).

10 Imahori, H., Hagiwara, K., Akiyama, T., Taniguchi, S., Okada, T. & Sakata, Y. Synthesis and photophysical property of porphyrin-linked fullerene, *Chem. Lett*. **24**, 265–266 (1995).

11 Imahori, H. *et al*. Comparison of reorganization energies for intra- and intermolecular electron transfer, *Angew. Chem. Int. Ed*. **41**, 2344–2347 (2002).

12 Guldi, D. M., Illescas, B. M., Atienza, C. M., Wielopolskia, M. & Martín, N. Fullerene for organic electronics, *Chem. Soc. Rev*. **38**, 1587–1597 (2009).

13 de la Torre, G., Giacalone, F., Segura, J. L., Martin, N. & Guldi, D. M. Electronic Communication through π-Conjugated Wires in Covalently Linked Porphyrin/C_{60} Ensembles. *Chem. Eur. J*. **11,** 1267–1280 (2005).

14 Sakamoto, A., Furukawa, Y. & Tasumi, M. Infrared and Raman studies of poly(*p*-phenyenevinylene) and its model compounds. *J. Phys. Chem*. **96**, 1490–1494 (1992).

15 Shizu, K., Sato, T. & Tanaka, K. Vibronic coupling density analysis for free-base porphin cation. *Chemical Physics Letters* **505,** 42–46 (2011).

16 Iwahara, N., Sato, T., Tanaka, K. & Kaji, H. Vibronic couplings in derivatives for organic photovoltaics. *Chemical Physics Letters* **590,** 169–174 (2013).

17 Gloss, G. L., Calcaterra, L. T., Green, N. J., Penfield, K. W. & Miller, J. R. Distance, stereoelectronic effects, and the Marcus inverted region in intramolecular electron transfer in organic radical anions. *J. Phys. Chem.* **90**, 3673–3683 (1986).

18 Wiederrecht, G. P., Niemczyk, M. P., Svec, W. A. & Wasielewski, M. R. Ultrafast photoinduced electron transfer in a Chlorophyll-based triad: Vibrationally hot ion pair intermediates and dynamic solvent effects. *J. Am. Chem. Soc.* **118**, 81–88 (1996).

19 Koch, M. *et al*. Real-time observation of the formation of excited radical ions in bimolecular photoinduced charge separation: Absence of the Marcus inverted region explained. *J. Am. Chem. Soc.* **135**, 9843–9848 (2013).

20 Zhu, X.; Mitsui, C.; Tsuji, H. & Nakamura,E, Modular synthesis of 1*H*-indenes, dihydro-*s*-indacene, and diindenoindacene-a carbon-bridged *p*-phenylenevinylene congener, *J. Am. Chem. Soc.* **131**, 13596–13597 (2009).

21 Prato, M. & Maggini, M., Fulleropyrrolidines: a family of full-fledged fullerene derivatives, *Acc. Chem. Res.* **31**, 519–526 (1998).

22 Armaroli, N. *et al*. Photoinduced energy transfer in a fullerene–oligophenylenevinylene conjugate. *Chem. Commun*. 599–600 (2000).

23 Weller, A., Photoinduced electron transfer in solution: exciplex and radical ion pair formation free enthalpies and their solvent dependence, *Z. Phys. Chem.* **133**, 93–98 (1982).

24 Marcus, R. A., On the theory of oxidation reduction involving electron transfer. I. *J. Chem. Phys.* **24**, 966–978 (1956).

25 Ricks, A. B. *et al*. Exponential Distance Dependence of Photoinitiated Stepwise Electron Transfer in Donor–Bridge–Acceptor Molecules: Implications for Wirelike Behavior. *J. Am. Chem. Soc.* **134,** 4581–4588 (2012).

26 Giacalone, F., Segura, J. L., Martin, N. & Guldi, D. M. Exceptionally Small Attenuation Factors in Molecular Wires. *J. Am. Chem. Soc.* **126,** 5340–5341 (2004).

27 Marcus, R. A., On the theory of electron-transfer reactions. VI. Unified treatment for homogeneous and electrode reactions *J. Chem. Phys.* **43**, 679–701 (1965).

28 Jortner, J., Temperature dependent activation energy for electron transfer between biological molecules, *J. Chem. Phys.* **64**, 4860–4867 (1976).

29 Hopfield, J. J., Electron transfer between biological molecules by thermally activated tunneling, *Proc. Natl. Acad. Sci. USA* **71**, 3640–3644 (1974).

30 Winkler, J. R. & Gray, H. B. Electron transfer in ruthenium-modified proteins. *Chem. Rev.* **92,** 369–379 (1992).

31 Osuka, A. *et al*.,Energy-Gap Dependence of Photoinduced Charge Separation and Subsequent Charge Recombination in 1,4-Phenylene-Bridged Zinc–Free-Base Hybrid Porphyrins, *Chem. Eur. J.* **6**, 33–46 (2000).

32 Wiederrecht, G. P., Niemczyk, M. P., Svec, W. A. & Wasielewski, M. R. Ultrafast photoinduced electron transfer in a Chlorophyll-based triad: Vibrationally hot ion pair intermediates and dynamic solvent effects. *J. Am. Chem. Soc.*, **118**, 81–88 (1996).

33 Koch, M. *et al*. Real-time observation of the formation of excited radical ions in bimolecular photoinduced charge separation: Absence of the Marcus inverted region explained. *J. Am. Chem. Soc.*, **135**, 9843–9848 (2013).

34 Kushmerick, J. G. *et al*. Vibronic contributions to charge transport across molecular junctions. *Nano Lett.* **4,** 639–642 (2004).

35 Osorio, E. A. *et al*. Addition energies and vibrational fine structure measured in electromigrated single-molecule junctions based on an oligophenylenevinylene derivative. *Adv. Mater.* **19,** 281–285 (2007).

36 Zhu, X., Tsuji, H., Nakabayashi, K., Ohkoshi, S. & Nakamura, E. Air- and heat-stable planar tri-*p*-quinodimethane with distinct biradical characteristics. *J. Am. Chem. Soc.* **133**, 16342–16345 (2011).

37 Zhu, X. *et al*. New sensitizers for dye-sensitized solar cells featuring a carbon-bridged phenylenevinylene. *Chem. Commun.* **49,** 582-584 (2013).

38 Sukegawa, J., Tsuji, H., & Nakamura, E. Large electronic coupling in a homoconjugated donor–acceptor system involving carbon-bridged oligo-*p*-phenylenevinylene and triazine. *Chem. Lett.* doi:10.1246/cl.140022. (in the press)

39 Shizu, K., Sato, T., Tanaka, K. & Kaji, H. Electron–vibration interactions in triphenylamine cation: Why are triphenylamine-based molecules good hole-transport materials? *Chemical Physics Letters* **486,** 130–136 (2010).

40 Sato, T. *et al*. in The Jahn-Teller Effect: Fundamentals and Implications for Physics and Chemistry. (ed. Koeppel, H., Yarkony, D. R. & Barentzen, H.) 99–131 (Springer, 2010).

Chapter 3

Synthesis and Photophysical Properties of Carbon-Bridged Oligo(Phenylenevinylene)s–Fullerene Conjugates

本章については、５年以内に雑誌等で刊行予定のため、非公開。

Chapter 4

Large Electronic Coupling in a Homoconjugated Donor–Acceptor System Involving Carbon-Bridged Oligo-*p*-Phenylenevinylene and Triazine

4-1. Introduction

Development of donor–acceptor (D–A) systems that show efficient charge separation (CS) and charge recombination (CR) in the Marcus inverted region is required for artificial photosynthesis.[1] The rate of charge transfer is primarily determined by the D–A electronic coupling (*V*), which depends on the type of conjugation or interaction between D and A, such as π conjugation,[2] Si–Si σ conjugation,[3,4] cross-conjugation,[5] and π–π stacking.[6] However, the D–A systems electronically coupled via homoconjugation have received less attention.[7–13] Here we show that the carbon-bridged oligo-*p*-phenylenevinylene (COPV)[14–16] possessing homoconjugated triazine (TRZ) substituents **COPV2–(TRZ)$_4$** undergoes efficient CS (98%) and 100-times slower CR in polar solvent (Figure 1). The electronic coupling was estimated to be as large as 1.0×10^3 cm^{-1}, which is one of the largest values among conjugations/interactions. The rigid and planar skeleton of COPVs is responsible for the good electron donating ability as previously demonstrated in the application that the COPVs served as efficient photosensitizer in dye-sensitized solar cell.[17]

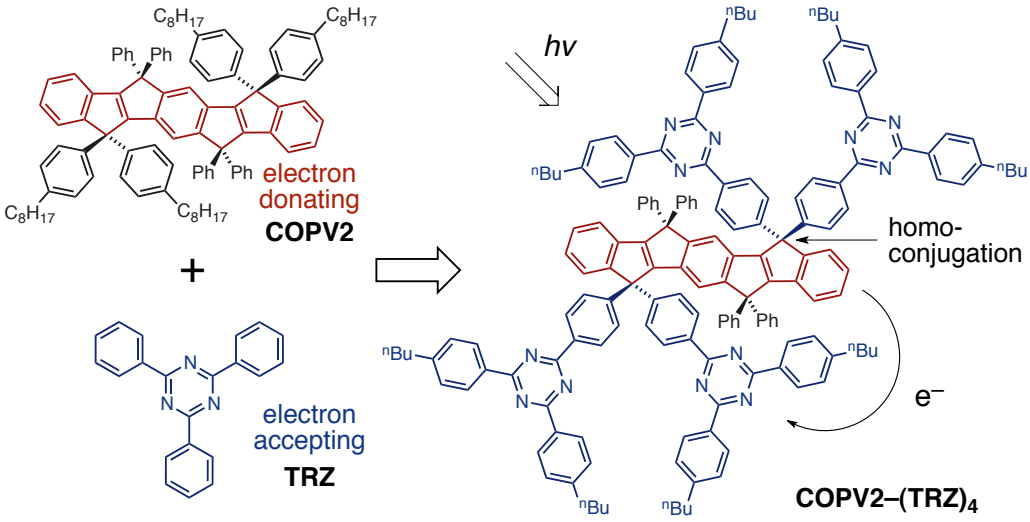

Figure 1. Novel donor-acceptor conjugate **COPV2–(TRZ)$_4$**.

4-2. Results&Discussion

4-2-1. DFT calculations

According to DFT calculations of COPV2, the homoconjugation only between HOMO of COPV2 and HOMO TRZ is symmetrically allowed (Figure 2). The homoconjugation between HOMO of COPV2 and LUMO of TRZ is negligible because of the large energy gap.

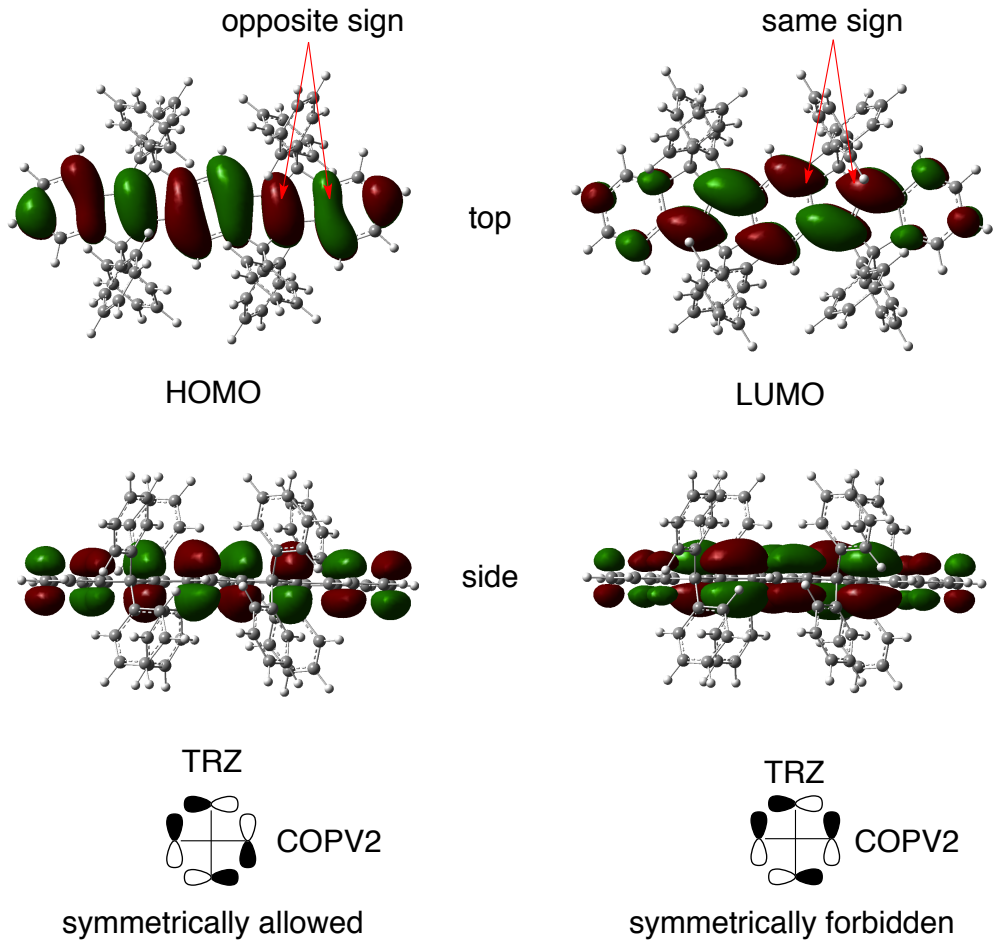

Figure 2. Kohn–Sham orbitals of **COPV2** (B3LYP/6-31G*). The *n*-octyl groups are omitted to reduce the calculation costs.

DFT calculations of **COPV2–(TRZ)$_4$** indicated that HOMO is delocalized on COPV2 moiety, while LUMO is distributed over COPV2 and TRZ moieties (Figure 3). The latter can be attributed to the close energy level of LUMOs of COPV2 and TRZ although they are not conjugated as mentioned above. Thus the photoexcitation of

COPV2–(TRZ)$_4$ follows CS from COPV2 to TRZ moieties to form the charge separated state **COPV2$^{\bullet+}$–(TRZ$^{\bullet-}$)(TRZ)$_3$** favorably in polar solvents.

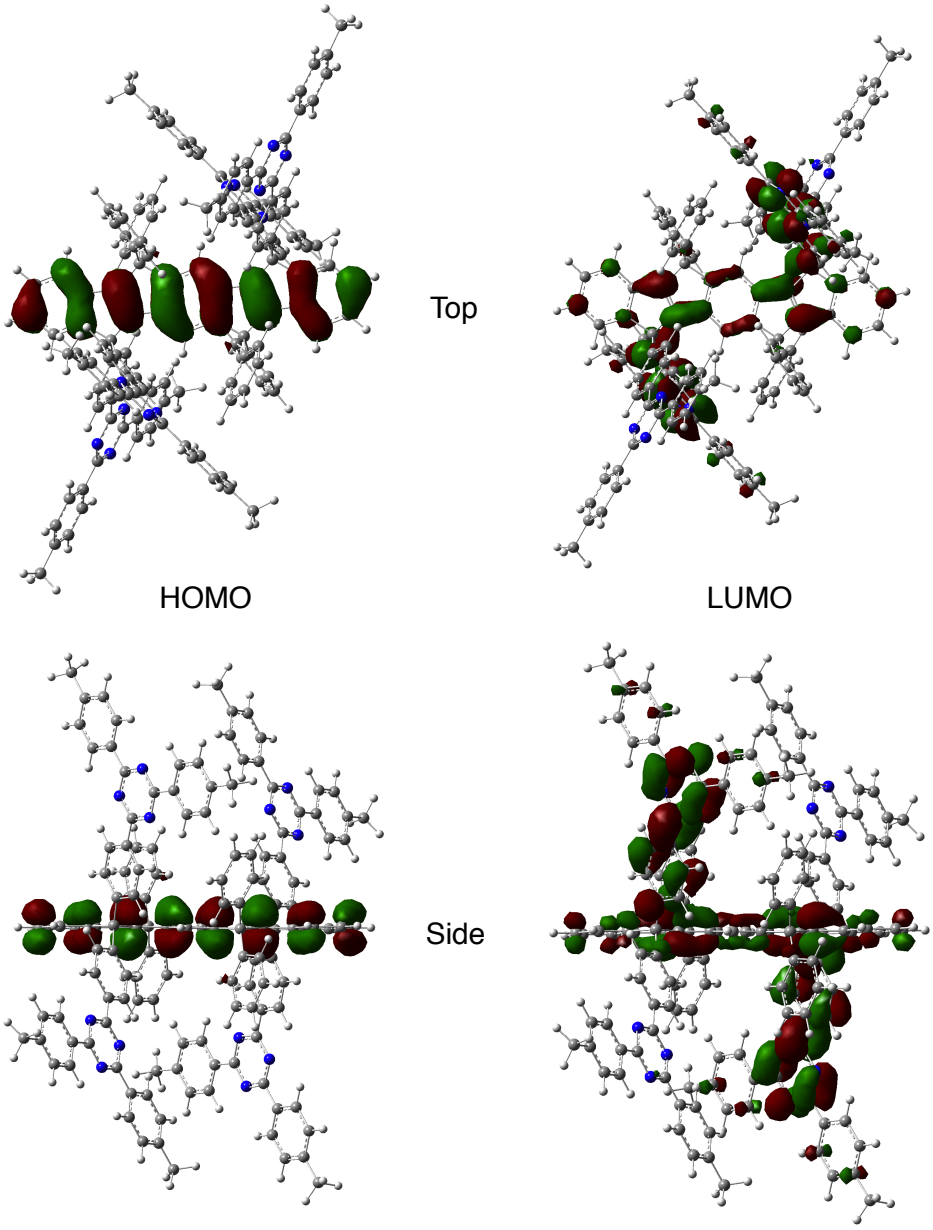

Figure 3. Kohn-Sham orbitals of **COPV2–(TRZ)$_4$** (B3LYP/6-31G*). *n*-Butyl groups are replaced by methyl group to reduce the calculation costs.

4-2-2. Synthesis

Scheme 1 shows the synthesis of the ketone substituted by triazine (**5**). The diaryl triazine (**2**) was obtained by the nucleophilic attack of the excess amount of the Grignard reagent to the cyanuric chloride (**1**) in moderate yield. Miyaura–Ishiyama–Hartwig boration on the di-bromide (**3**) afforded the corresponding bononic ester (**4**). Suzuki–Miyaura cross coupling of **2** and **4** succeeded in good yield without the addition of ligand thanks to the assistance of nitrogen next to C–Cl bond.

Scheme 1. Synthesis of the ketone.

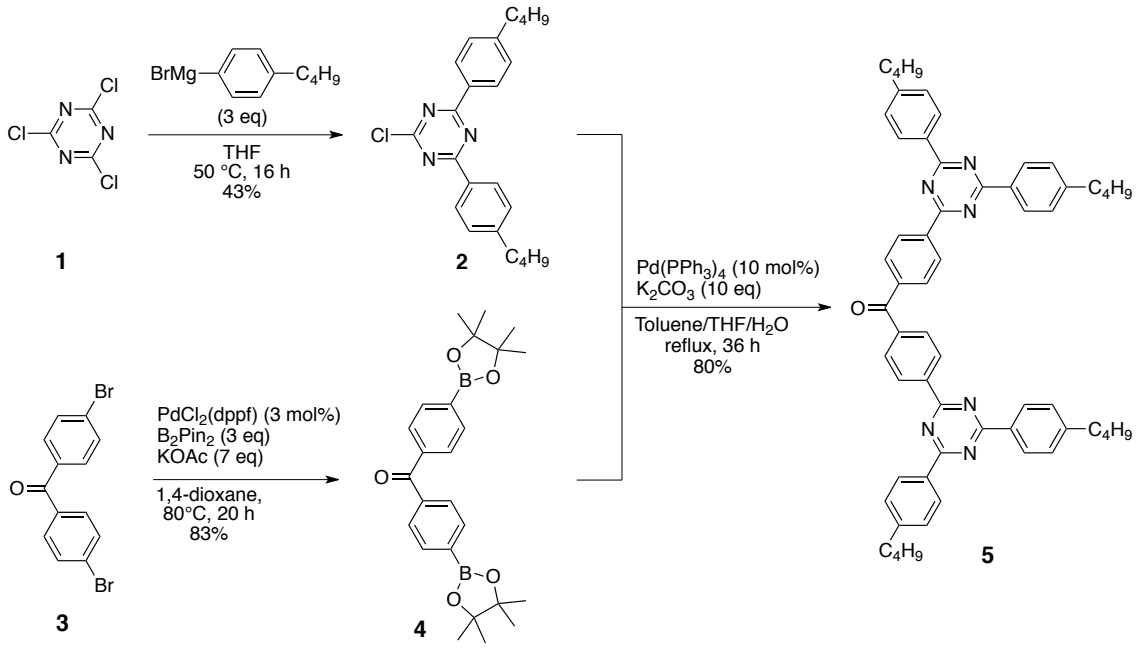

The target compound **COPV2–(TRZ)$_4$** was obtained by the reductive cyclization using lithium naphthalenide (LiNaph) and the subsequent intramolecular Friedel–Crafts reaction in good yield (Scheme 2). The latter reaction was sluggish with equimolar BF_3•OEt_2 (2 eq) because of the coordination with twelve sp^2 nitrogen atoms of triazines, thus the excess reagent was necessary.

Scheme 2. Reductive cyclization of ester **6** and Friedel-Crafts reaction.

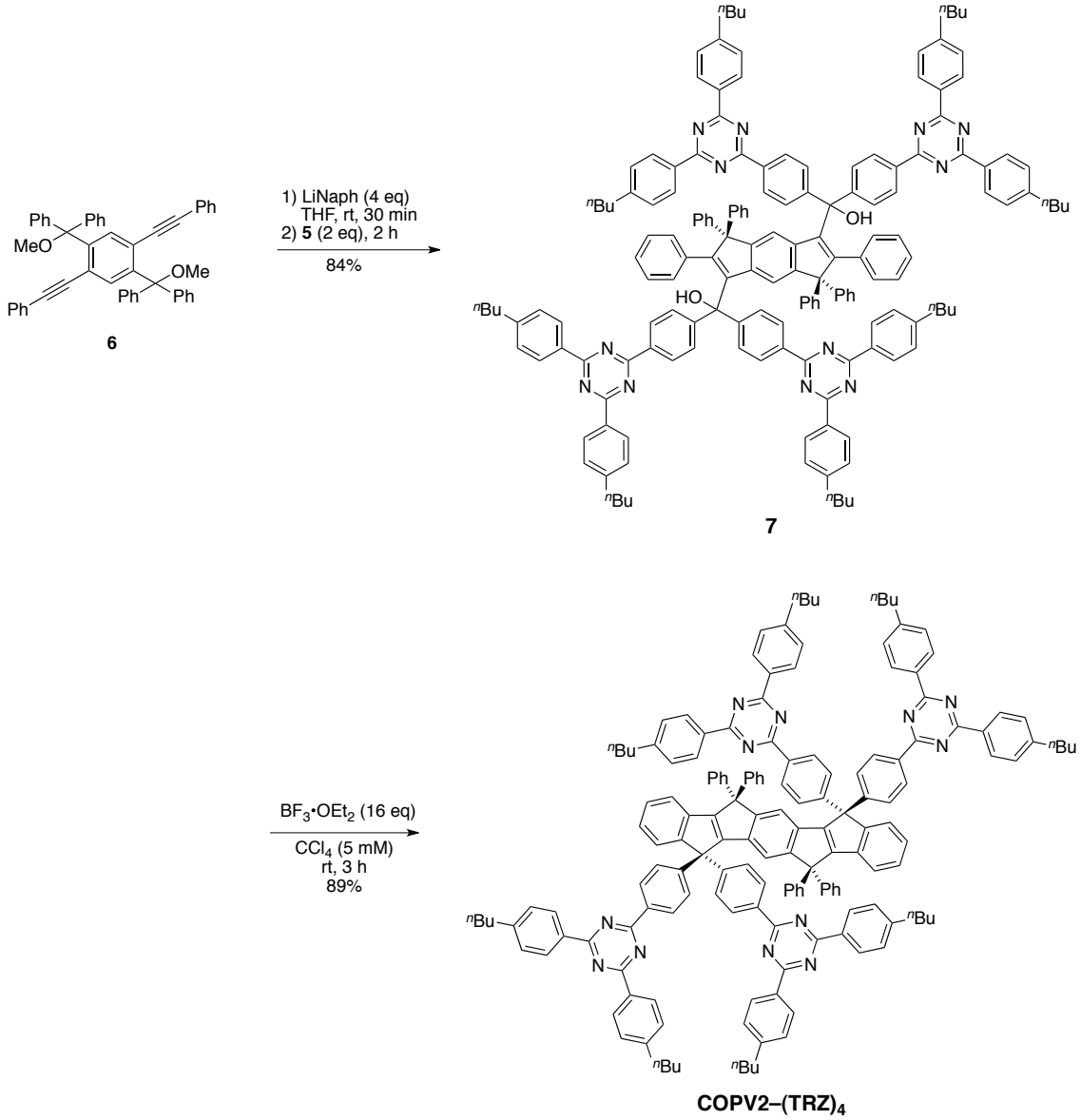

4-2-3. Steady-State Photophysical Properties

Steady state UV-Vis absorption spectrum of **COPV2–(TRZ)$_4$** shows a very small redshift of the COPV2 moiety (6 nm) compared with the parent COPV2, suggesting only small electronic coupling between the COPV2 and TRZ moieties in the ground state (Figure 4a). Steady-state fluorescence spectra in toluene (upon exciting at both 300 and 400 nm) showed emission from the COPV2 moiety, while that in benzonitrile showed an additional tail over 500 nm (Figure 4b). This band was assigned to charge-transfer (CT) emission.

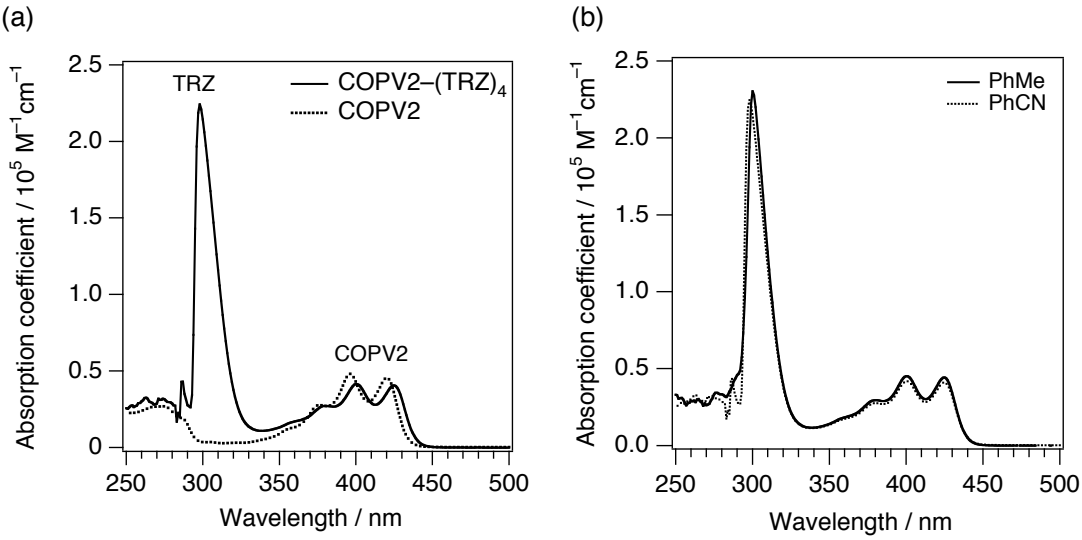

Figure 4. (a) UV-Vis absorption spectra of **COPV2–(TRZ)$_4$** and **COPV2** in toluene and dichloromethane, respectively. (b) UV-Vis absorption spectra of **COPV2–(TRZ)$_4$** in toluene and benzonitrile.

Emission spectra showed the COPV2 fluorescence around 400-600 nm, while the triazine emission was not detectable upon excitation at 300 nm (Figure 5a). In polar solvent, the emission was quenched by 56%, which suggest the electron transfer from COPV2 to TRZ because there is no possibility of energy transfer.

The excitation spectra of the emission at 470 nm showed the absorption of not only COPV2 but also TRZ, which indicates the energy transfer from TRZ to COPV2 (Figure 5b). This attests to the efficient light-harvesting ability of TRZ moieties. Employing the light-harvesting moieties at the quaternary carbons would be a good

strategy to obtain an efficient photosensitizer. Note that the effects of homoconjugation to promote energy transfer was reported in the literature.[18]

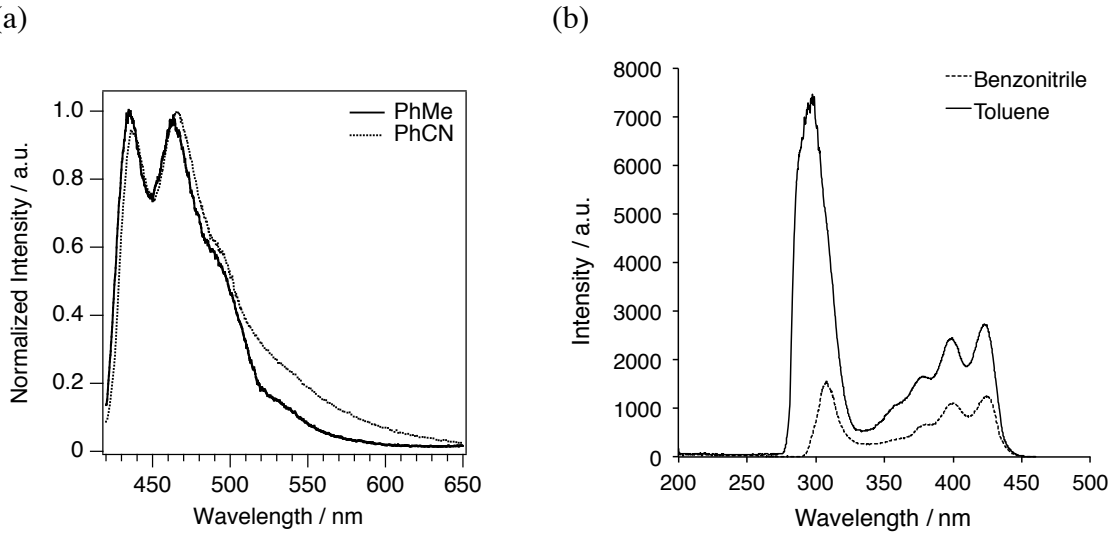

Figure 5. (a) Steady-state fluorescence spectra and (b) Excitation spectra of **COPV2–(TRZ)$_4$** in argon saturated benzonitrile and toluene (1×10^{-6} M). Excitation at 400 nm and emission at 470 nm.

Table 2 summarizes the photophysical properties. Slight decrease in the optical energy gap, which was estimated from the absorption peak (λ_{abs}) and emission peak (λ_{em}), might indicate the elongation of the π conjugation via homoconjugation. Decrease in the fluorescence quantum yield (Φ_F) of **COPV2–TRZ** (Φ_F = 1.00) in toluene compared to **COPV2** (Φ_F = 0.84) reflects the internal conversion at TRZ moieties. The lower Φ_F of **COPV2–TRZ** was found in the polar solvent, which supports the electron transfer from COPV2 to TRZ moieties.

Table 2. Summary of photophysical properties.

compound	solvent	λ_{abs} / nm	λ_{em} / nm	E_g^{OP} / eV [a]	Φ_F
COPV2	DCM	419	433	2.91	1.00
COPV2–(TRZ)$_4$	PhMe	425	434.6	2.88	0.84
	PhCN	426	436.0	2.88	0.36

[a] optical energy gap calculated by the equation $E_g^{OP} = 1240/((\lambda_{abs} + \lambda_{em})/2)$.

4-2-4. Electrochemistry

Cyclic voltammetry showed a reversible oxidation wave at 0.69 V (vs Fc^+/Fc) and reduction wave at –2.23 V (vs Fc^+/Fc) in tetrahydrofuran (THF), which can be assigned to the one-electron oxidation of the COPV2 and the four-electron reduction of the TRZ moieties, respectively (Figure 6), indicating that the COPV and the TRZ moieties are independent of each other. The oxidation peak was anodically shifted compared with that of **COPV2** (0.53 V)[16], while the reduction peak was essentially the same as that of **TRZ** (–2.18 V)[19]. The origin of the anodic shift of the COPV2 moiety can be ascribed to the orbital interaction between HOMOs of the COPV2 and TRZ moieties via homoconjugation, which is symmetrically allowed.

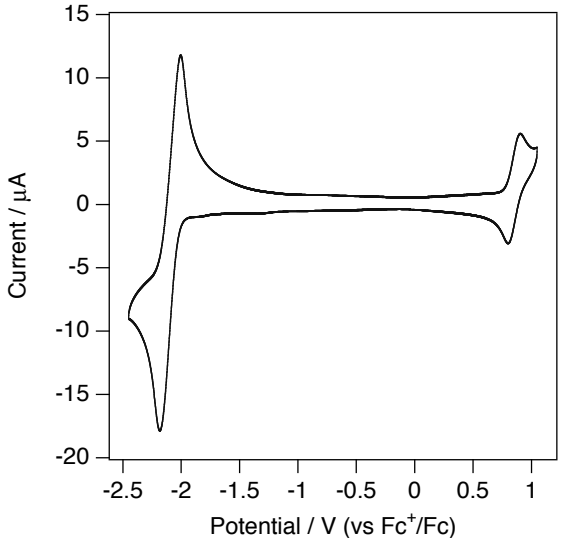

Figure 6. Cyclic voltammogram of **COPV2–(TRZ)$_4$** in THF (0.1 M Bu_4NPF_6, 100 mV/s scan speed).

The driving forces for CS ($-\Delta G^0_{CS}$) and CR ($-\Delta G^0_{CR}$) in benzonitrile (PhCN, ε_S = 25.2) were estimated to be 0.03 eV and 2.85 eV, respectively, using Weller's model.[20]

$$E_{IP} = E_{ox} - E_{red} - \frac{1}{4\pi\varepsilon_0}\frac{e^2}{\varepsilon_S R_{DA}} + \frac{e^2}{4\pi\varepsilon_0}\left(\frac{1}{2r_D} + \frac{1}{2r_A}\right)\left(\frac{1}{\varepsilon_S} - \frac{1}{\varepsilon'_S}\right) \quad (1)$$

where E_{ox} and E_{red} are oxidation and reduction potentials, respectively, e is the electronic charge, ε_0 is the dielectric constant of vacuum, ε_s is the static dielectric constatnt of the

solvent in which the rate constants are measured, ε_s' is the dielectic constant of the solvent in which E_{ox} and E_{red} are measured, R_{DA} (0.915 Å) is the donor-acceptor center-to-center distance, and r_D (0.558 Å) and r_A (0.562 Å) are the spherical radii of donor and acceptor, respectively. R_{DA}, r_D, and r_A were estimated from the energy minized strucutre calculated using density functional theory.

Note that $-\Delta G^0_{CS}$ in a less-polar solvent, such as tetrahydrofuran (THF, ε_S = 7.58), is negative (–0.06 eV). Thus, CS is thermodynamically feasible only in highly polar solvents.

Table 1. Redox Potentials of **COPV2–(TRZ)$_4$** and references (in V vs Fc^+/Fc) and the driving force for charge separation ($-\Delta G^0_{CS}$) and charge recombination ($-\Delta G^0_{CR}$).[a]

compound	solvent	$E_{1/2}^{ox}$ (V)	$E_{1/2}^{red}$ (V)	$-\Delta G^0_{CS}$ (eV)[b]	$-\Delta G^0_{CR}$ (eV)[c]
COPV2[d]	CH_2Cl_2	0.53	–	–	–
TRZ[e]	PhMe/MeCN (1:1)	–	–2.18	–	–
COPV2–(TRZ)$_4$	THF	0.69	–2.25	–0.06	2.94
	PhCN	0.66	–2.25	0.03	2.85

[a] Experimental conditions: GCE as working electrode, Pt as counter, Bu_4NPF_6 (0.1 M) as supporting electrolyte, 100 mV/s scan rate, vs Fc^+/Fc. [b] estimated using the Weller's model. [c] estimated using the equation $-\Delta G^0_{CR} = E_g^{OP} - (-\Delta G^0_{CS})$. [d] taken from ref 16. [e] taken from ref 19.

4-2-5. Fluorescence Lifetime

The fluorescence lifetime (τ_F) of **COPV2–(TRZ)$_4$** clearly depended on the polarity of solvent as depicted in Figure 7. The emission excited at 405 nm in toluene decays mono-exponentially with a lifetime of 1.97 ns, which is similar to the **COPV2** (τ_0=1.68 ns) in toluene, suggesting that the fluorescence quenching by charge separation (CS) does not occur. In contrast the emission in benzonitrile decays bi-exponentially in 0.17 ns (5%) and 10.8 ns (95%). The fast component can be assigned as the fluorescence from the singlet excited state of COPV2 moiety quenched by the charge separation, while the slow component is due to the CT emission.

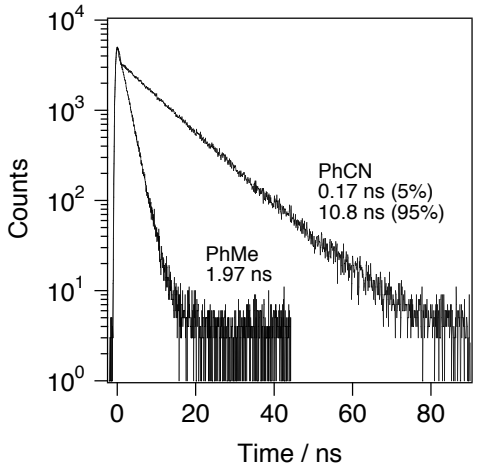

Figure 7. Fluorescence decay profiles of **COPV2–(TRZ)$_4$** at 460 nm in deaerated toluene and benzonitrile at 298 K observed by excitation at 405 nm.

4-2-6. Energy Diagram

Figure 8 summarizes plausible processes upon photoexcitation. In toluene, the singlet excited state **^{1}COPV2*–(TRZ)$_4$** is quenched by either fluorescence (k_F) or nonradiative decay (k_{nr}) at rate constants of 4.2×10^8 s^{-1} and 8.2×10^7 s^{-1}, respectively, according to the equations $k_F = \Phi/\tau_F$ and $\Phi = k_F/(k_F + k_{nr})$ (Figure 8a). In benzonitrile, CS(k_{CS}) occurs to form the charge-separated state **COPV2$^{\bullet+}$–(TRZ$^{\bullet-}$)(TRZ)$_3$** at a rate constant of 5.3×10^9 s^{-1} based on the equation $k_{CS} = 1/\tau_F - 1/\tau_0$ (Figure 8b). The quantum yield of CS is 98%. The charge-separated state decays via CT emission (k_{CT}) or a nonradiative process (k_{nr2}) at rate constants of 3.2×10^7 s^{-1} and 6.2×10^7 s^{-1}, respectively. The nonradiative process is composed of CR via tunneling mechanisms and some other relaxation pathways. Thus the CR rate is approximately 100 times slower than the CS rate, which indicates the CR process is located in the Marcus inverted region.[21]

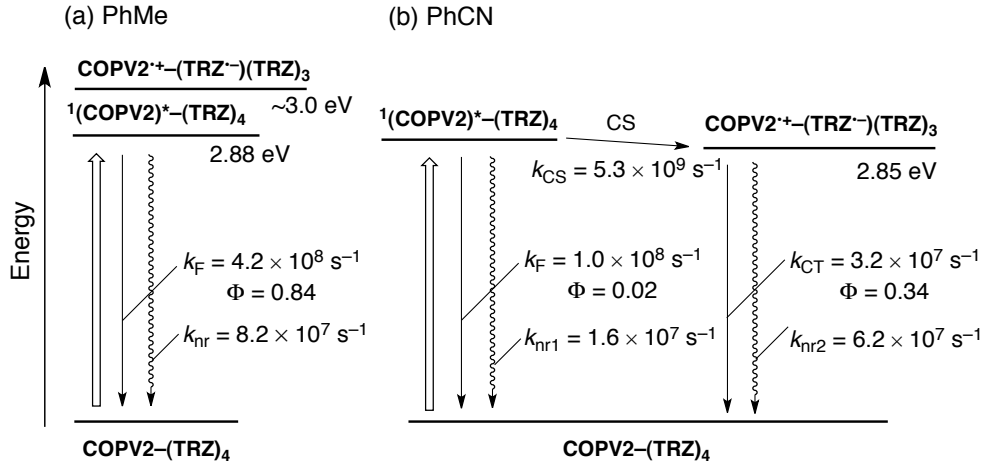

Figure 8. Energy diagram and the possible reaction pathways of **COPV2–(TRZ)$_4$** in (a) toluene and (b) benzonitrile.

The electronic coupling (V) can be obtained by the following equation.[22]

$$V \approx \sqrt{\frac{1.39\times10^5 k_{CT}}{\nu_{max} n^2 R^2}} = 1.0\times10^3 \text{ cm}^{-1}$$

Here, n is the refractive index of the solvent (1.528), R is the center to center D–A distance (9.2 Å), and ν_{max} is the maximum absorption wavenumber (2.27×10^3 cm^{-1}). The V value is quite large compared to other D–A systems linked via π-conjugation (*e.g.* 1830 cm^{-1})[23] and π–π staking in the contacted radical-ion pairs of zinc porphyrin–fullerene dyads (100 cm^{-1})[24].

4-3. Summary

In summary a new class of D–A system that features homoconjugative interaction between D and A parts have been designed and synthesized. This unique system showed a highly efficient intramolecular CS, and a CR that is located in the Marcus inverted region. The electronic coupling via homoconjugation is larger than by other types of conjugations or interactions. The aryl substituents of COPVs can readily be modified and thus the energy levels and the frontier orbitals can be tuned. The orbital engineering would maximize the CS rate and minimize the CR rate by making use of the symmetry rule for homoconjugation. This study is the cornerstone for the development of homoconjugated D–A systems toward artificial photosynthesis.

Experimental Section

General. All reactions dealing with air- or moisture-sensitive compounds were carried out in a dry reaction vessel under nitrogen or argon. The water content of the solvent was confirmed with a Karl-Fischer Moisture Titrator (MKC-210, Kyoto Electronics Company) to be less than 50 ppm. Analytical thin-layer chromatography was performed on glass plates coated with 0.25 mm 230–400 mesh silica gel containing a fluorescent indicator (Merck). Flash silica gel column chromatography was performed on silica gel 60N (Kanto, spherical and neutral, 140–325 mesh) as described by Still. Gel permeation column chromatography (GPC) was performed on a Japan Analytical Industry LC-908 (eluent: toluene) with JAIGEL 1H and 2H polystyrene columns.

Materials. Unless otherwise noted, materials were purchased from Tokyo Kasei Co., Aldrich Inc., and other commercial suppliers and used after appropriate purification before use. Anhydrous ethereal solvents (stabilizer-free) were purchased from WAKO Pure Chemical and purified by a solvent purification system (GlassContour) equipped with columns of activated alumina and supported copper catalyst (Q-5) prior to use. All other solvents were purified by distillation and stored over molecular sieves 4Å.

Instruments. Proton nuclear magnetic resonance (^{1}H NMR) and carbon nuclear magnetic resonance (^{13}C NMR) spectra were recorded using a JEOL ECA-500 (500 MHz) NMR spectrometers. Chemical data for protons are reported in parts per million (ppm, δ scale) downfield from tetramethylsilane and are referenced to the residual protons in the NMR solvent ($CDCl_3$: δ 7.26). Carbon nuclear magnetic resonance spectra (^{13}C NMR) were recorded at 125 MHz: chemical data for carbons are reported in parts per million (ppm, δ scale) downfield from tetramethylsilane and are referenced to the carbon resonance of the solvent ($CDCl_3$: δ 77.0). The data are presented as follows: chemical shift, multiplicity (s = singlet, d = doublet, t = triplet, m = multiplet and/or multiple resonances, br = broad), coupling constant in Hertz (Hz), and integration. Melting points of solid materials were determined on a Mel-Temp II capillary melting-point apparatus and are uncorrected. Routine mass spectra were acquired by atmospheric pressure ionization (APCI) using a quadrupole mass analyzer on Shimadzu QP-8000. UV-vis absorption and fluorescence spectra are recorded on JASCO V-670

and FP6500 spectrometers, respectively. Cyclic voltammetry (CV) and differential pulse voltammetry (DPV) were performed on HOKUTO DENKO HZ-5000 voltammetry analyzer. Steady state UV/Vis spectroscopy and fluorescence spectroscopy were performed on JASCO V-670 and JASCO FP6500 spectrophotometer, respectively. Fluorescence lifetime measurements were performed on Hamamatsu Photonics C11367-01 spectrophotometer. Absolute photoluminescence quantum yield was measured on Hamamatsu Photonics C9920-02 spectrophotometer.

Synthesis.

2,4-bis(4-butylphenyl)-6-chloro-1,3,5-triazine (2)

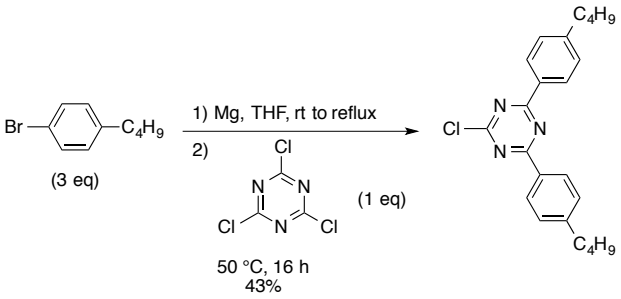

A solution of 4-*n*-butylbromobenzene (31 mL, 180 mmol, 3 eq) was added dropwise to a suspension of magnesium turnings (4.81 g, 198 mmol, 3.3 eq) in anhydrous THF (120 mL) over 30 minutes. After complete addition, the reaction mixture was maintained for 2 h at reflux temperature, then cooled to room temperature. The Grignard solution was added dropwise to a solution of cyanuric chloride (11.1 g, 60.0 mmol) in anhydrous THF (100 mL) while the temperature was maintained at 0 °C. When the addition was completed, the mixture was stirred for 10 h at 50 °C and then cooled to room temperature and poured into an aqueous solution of HCl (200 mL) to neutralize. Ethyl acetate (200 mL) was poured in the mixture. The organic phase was separated, washed three times with water, dried over anhydrous $MgSO_4$, then concentrated and the residue was purified by silica-gel chromatography (hexane/dichloromethane = 20:1 to 5:1) to afford the title compound (9.89 g, 26.0 mmol, 43%) as a white solid. Mp: 82–83 °C; ^{1}H NMR (500 MHz, $CDCl_3$): δ 0.93 (t, *J* = 7.4 Hz, 6H), 1.37 (sext, *J* = 7.4 Hz, 4H), 1.64 (quint, *J* = 7.4 Hz, 4H), 2.70 (t, *J* = 7.4 Hz, 4H), 7.33 (d, *J* = 8.0 Hz, 4H), 8.50 (d, *J* = 8.0 Hz, 4H); ^{13}C NMR (125 MHz, $CDCl_3$): δ 13.9, 22.3, 33.3, 35.8, 128.9, 129.4, 132.0,

149.3, 171.9, 173.3; TOF MS (APCI+): 380.1 $[M+H]^+$. Anal. Calcd for $C_{23}H_{26}ClN_3$: C, 72.71; H, 6.90; N, 11.06; Found: C, 72.59; H, 7.02; N, 10.86.

bis(4-(4,4,5,5-tetramethyl-1,3,2-dioxaborolan-2-yl)phenyl)methanone (4)

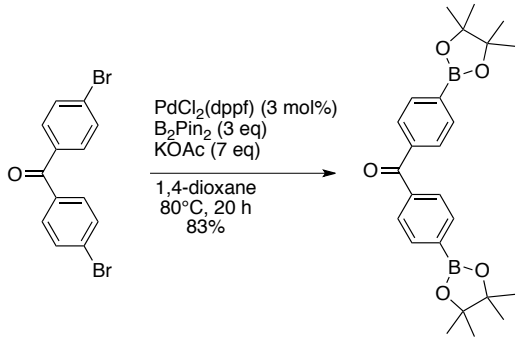

A solution of bis(4-bromophenyl)methanone (3.00 g, 8.82 mmol), B_2Pin_2 (6.72 g, 26.5 mmol, 3 eq) and KOAc (6.06 g, 61.7 mmol, 7 eq) in 50 mL of 1,4-dioxane was degassed through argon for 10 min. $PdCl_2$(dppf) (360 mg, 0.441 mmol, 5 mol%) were added and the solution was heated to 80 °C. After stirring for 20 hours, the reaction mixture was cooled to room temperature, and it was washed with water three times, and dried over $MgSO_4$. The organic phase was evaporated, and the resulting solid was washed with *n*-hexane to provide the title compound as a white solid (3.17 g, 7.30 mmol, 83%). Mp: 235–236 °C; ^{1}H NMR (500 MHz, $CDCl_3$): δ 1.35 (s, 24 H), 7. 74 (d, J = 8.0 Hz, 4H), 7.89 (d, J = 8.0 Hz, 4H); ^{13}C NMR (125 MHz, $CDCl_3$): δ 24.9, 84.2, 129.1, 134.5, 139. 6 197.1 (carbon atoms adjacent to boron atom could not be detected); TOF MS (APCI+): 435.2 $[M+H]^+$. Anal. Calcd for $C_{25}H_{32}B_2O_5$•0.25H_2O: C, 68.45; H, 7.47; Found: C, 68.49; H, 7.52.

bis(4-(4,6-bis(4-butylphenyl)-1,3,5-triazin-2-yl)phenyl)methanone (5)

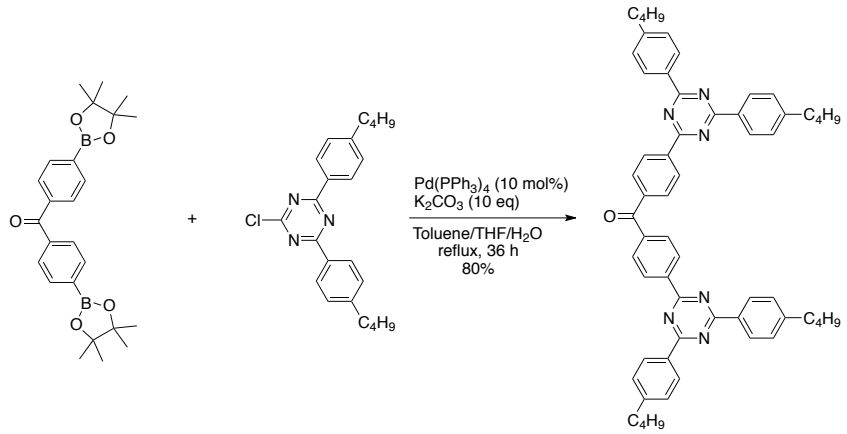

To a solution of **4** (2.37 g, 5.45 mmol), **2** (4.56 g, 12.0 mmol, 2.2 eq) in 40 mL of toluene and 15 mL of THF was poured into 3.5 M aqueous K_2CO_3 (15.6 mL, 54.6 mmol, 10 eq). The mixture was degassed through argon for 30 min. $Pd(PPh_3)_4$ (630 mg, 2.50×10^{-3} mmol, 10 mol%) were added and the solution was heated to reflux. After stirring for 36 hours, the reaction mixture was cooled to room temperature, and it was washed with water three times, and dried over $MgSO_4$. The organic phase was evaporated to furnish white solid, which was washed with *n*-hexane to yield the title compound (4.37 g, 5.03 mmol, 80%) as a white solid. Mp: 175–176 °C; ^{1}H NMR (500 MHz, $CDCl_3$): δ 0.96 (t, *J* = 7.4 Hz, 12H), 1.41 (sext, *J* = 7.4 Hz, 8H), 1.68 (quint, *J* = 7.4 Hz, 8H), 2.74 (t, *J* = 7.4 Hz, 8H), 7.39 (d, *J* = 8.3 Hz, 8H), 8.04 (d, *J* = 8.3 Hz, 4H), 8.69 (d, *J* = 8.3 Hz, 8H), 8.90 (d, *J* = 8.3 Hz, 4H); ^{13}C NMR (125 MHz, $CDCl_3$): δ 14.0, 22.4, 33.4, 35.8, 128.8 (two carbons are overlapping), 129.0 (two carbons are overlapping), 130.2, 133.5, 140.2, 148.2, 170.5, 171.8, 196.0; TOF MS (APCI+): 869.6 $[M+H]^+$. Anal. Calcd for $C_{59}H_{60}N_6O$: C, 81.53; H, 6.96; N, 9.67; Found: C, 81.48; H, 7.14; N, 9.58.

(2,3,3,6,7,7-hexaphenyl-3,7-dihydro-*s*-indacene-1,5-diyl)bis(bis(4-(4,6-bis(4-butylphenyl)-1,3,5-triazin-2-yl)phenyl)methanol) (7)

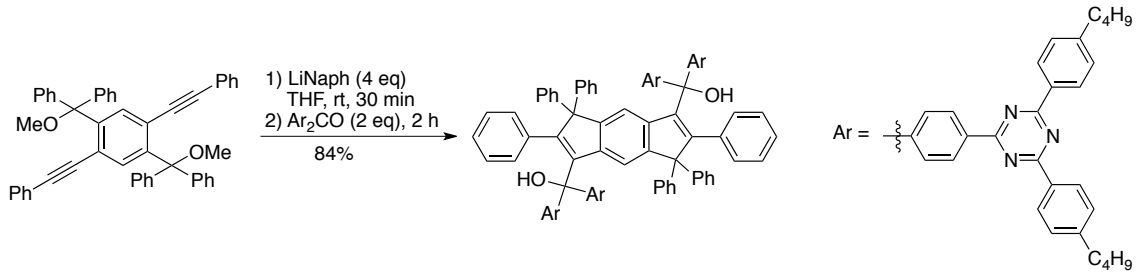

To a solution of compound **6** (3.11 g, 5.19 mmol) in THF (30 mL) was added the 0.648 M LiNaph in THF (8.80 mL, 5.70 mmol) at room temperature. After stirred for half an hour, **5** (2.59 g, 2.98 mmol) was added to the reaction mixture at room temperature. The reaction mixture was stirred for another 2 h and then quenched with several drops of saturated aqueous NH_4Cl. Ethyl acetate (200 mL) was poured in the mixture. The organic phase was washed three times with water, dried over anhydrous $MgSO_4$, then concentrated and the residue was purified on silica-gel column (*n*-hexane/dichloromethane = 3:1 to 2:1) to give the title compound (2.94 g, 1.25 mmol, 84%) as a white solid. Mp: 206–207 °C; ^{1}H NMR (500 MHz, $CDCl_3$): δ 0.94 (t, *J* = 7.4 Hz, 24H), 1.40 (sext, *J* = 7.4 Hz, 16H), 1.67 (quint, *J* = 7.4 Hz, 16H), 2.73 (t, *J* = 7.4 Hz, 16H), 2.95 (s, 2H), 6.18 (s, 2H), 6.55 (d, *J* = 7.4 Hz, 4H), 6.80 (t, *J* = 7.4 Hz, 4H), 6.87–6.90 (m, 12H), 7.01 (t, *J* = 7.4 Hz, 10H), 7.38 (d, *J* = 8.0 Hz, 16H), 7.44 (d, *J* = 8.6 Hz, 8H), 8.55 (d, *J* = 8.6 Hz, 8H), 8.68 (d, *J* = 8.0 Hz, 16H); ^{13}C NMR (125 MHz, $CDCl_3$): δ 14.0, 22.4, 33.4, 35.8, 70.7, 80.4, 126.4, 127.7, 127.8, 128.1, 128.4, 128.7, 128.8, 129.0, 130.0, 133.9, 125.7, 136.1, 140.8, 141.1, 144.8, 148.0, 149.4, 151.1, 171.0, 171.5 (two carbons are missing); TOF MS (APCI+): 2348.6 $[M+H]^+$. Anal. Calcd for $C_{166}H_{154}N_{12}O_2$: C, 84.87; H, 6.61; N, 7.16; Found: C, 84.63; H, 6.83; N, 7.09.

5,7,12,14-tetrahydro-5,5,12,12-tetra(4-(4,6-bis(4-butylphenyl)-1,3,5-triazin-2-yl)phenyl)-7,7,14,14-tetraphenyl-di(indeno[2,1-a:2',1'-d'])-s-indacene (COPV2–(TRZ)$_4$)

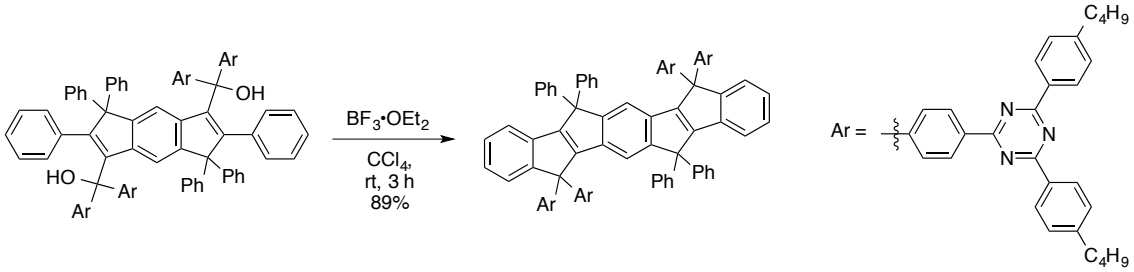

To a solution of compound **7** (829 mg, 0.353 mmol) in CCl_4 (70 mL) was added $BF_3 \cdot OEt_2$ (737 μL, 5.82 mmol, 16 eq) at room temperature. After being stirred for 3 hours, the reaction mixture was quenched with methanol. The reaction mixture was passed through a short-path silica-gel column with toluene as the eluent to give the title compound (728 mg, 0.315 mmol, 89%) as a yellow solid. Mp: > 400 °C (dec); ^{1}H NMR (500 MHz, $CDCl_3$): δ 0.94 (t, *J* = 7.4 Hz, 24H), 1.39 (sext, *J* = 7.4 Hz, 16H), 1.66 (quint, *J* = 7.4 Hz, 16H), 2.72 (t, *J* = 7.4 Hz, 16H), 7.05 (td, *J* = 1,7 and 6.9 Hz, 2H), 7.06 (td, *J* = 1,7 and 6.9 Hz, 2H), 7.13 (td, *J* = 1,7 and 7.4 Hz, 2H), 7.16 (td, *J* = 1,2 and 7.4 Hz, 2H), 7.22–7.29 (m, 18 H), 7.36 (d, *J* = 8.0 Hz, 16H), 7.41 (s, 2H), 7.64 (d, *J* = 8.6 Hz, 8H), 7.52 (d, *J* = 8.0 Hz, 2H), 8.59 (d, *J* = 8.6 Hz, 8H), 8.65 (d, *J* = 8.0 Hz, 16H); ^{13}C NMR (125 MHz, $CDCl_3$): δ 13.9, 22.4, 33.4, 35.8, 63.1, 63.2, 118.0, 121.0, 125.1, 125.8, 126.9, 127.6, 128.4, 128.6, 128.7, 128.9, 129.1, 129.2, 133.9, 135.3, 136.0, 139.1, 143.0, 147.1, 148.0, 155.0, 155.3, 155.9, 156.6, 171.0, 171.4; TOF MS (APCI+): 2312.6 $[M]^+$. Anal. Calcd for $C_{166}H_{150}N_{12}$: C, 86.20; H, 6.54; N, 7.27; Found: C, 85.94; H, 6.80; N, 7.15.

References

1 Fukuzumi, S. Bioinspired electron-transfer systems and applications. *Bull. Chem. Soc. Jpn.* **79,** 177–195 (2006).

2 Weiss, E. A. *et al.* Making a molecular wire: Charge and spin transport through para-phenylene oligomers. *J. Am. Chem. Soc.* **126,** 5577–5584 (2004).

3 Sasaki, M. *et al.* Oligosilane chain-length dependence of electron transfer of zinc porphyrin–oligosilane–fullerene molecules. *J. Phys. Chem. A* **111,** 2973–2979 (2007).

4 Kobori, Y. *et al.* Time-resolved EPR characterization of a folded conformation of photoinduced charge-separated state in porphyrin–fullerene dyad bridged by diphenyldisilane. *J. Am. Chem. Soc.* **131,** 1624–1625 (2009).

5 Ricks, A. B. *et al.* Controlling electron transfer in donor–bridge–acceptor molecules using cross-conjugated bridges. *J. Am. Chem. Soc.* **132,** 15427–15434 (2010).

6 Molina-Ontoria, A. *et al.* [2,2′]Paracyclophanebased π-conjugated molecular wires reveal molecular-junction behavior. *J. Am. Chem. Soc.* **133,** 2370–2373 (2011).

7 Karpiuk, J. Photoinduced electron transfer in malachite green lactone. *Phys. Chem. Chem. Phys.* **5,** 1078–1090 (2003).

8 Karpiuk, J. Dual fluorescence from two polar excited states in one molecule. structurally additive photophysics of crystal violet lactone. *J. Phys. Chem. A* **108,** 11183–11195 (2004).

9 Maslak, P. *et al.* Optical properties of spiroconjugated charge-transferd dyes. *J. Am. Chem. Soc.* **118,** 1471–1481 (1996).

10 King, S. M., Hintschich, S. I., Dai, D., Rothe, C. & Monkman, A. P. Spiroconjugation-enhanced intramolecular charge-transfer state formation in a polyspirobifluorene homopolymer. *J. Phys. Chem. C* **111,** 18759–18764 (2007).

11 Zhu, L. *et al.* Spiroconjugated intramolecular charge-transfer emission in non-typical spiroconjugated molecules: The effect of molecular structure upon the excited-state configuration. *ChemPhysChem* **14,** 982–989 (2013).

12 Yoon, M.-C. *et al.* Homoconjugation in diporphyrins: excitonic behaviors in singly and doubly linked Zn(II)porphyrin dimers. *Chem. Sci.* **4,** 1756 (2013).

13 Saragi, T. P. I., Spehr, T., Siebert, A., Fuhrmann-Lieker, T. & Salbeck, J. Spiro compounds for organic optoelectronics. *Chem. Rev.* **107,** 1011–1065 (2007).

14 Zhu, X., Mitsui, C., Tsuji, H. & Nakamura, E. Modular synthesis of 1*H*-indenes, dihydro-*s*-indacene, and diindenoindacene—a carbon-bridged

p-phenylenevinylene congener. *J. Am. Chem. Soc.* **131,** 13596–13597 (2009).

15 Zhu, X., Tsuji, H., Nakabayashi, K., Ohkoshi, S.-I. & Nakamura, E. Air- and heat-stable planar tri-*p*-quinodimethane with distinct biradical characteristics. *J. Am. Chem. Soc.* **133,** 16342–16345 (2011).

16 Zhu, X., Tsuji, H., López Navarrete, J. T., Casado, J. & Nakamura, E. Carbon-bridged oligo(phenylenevinylene)s: Stable π-systems with high responsiveness to doping and excitation. *J. Am. Chem. Soc.* **134,** 19254–19259 (2012).

17 Zhu, X. *et al*. New sensitizers for dye-sensitized solar cells featuring a carbon-bridged phenylenevinylene. *Chem. Commun.* **49,** 582 (2012).

18 Osío Barcina, J. *et al*. Efficient photoinduced energy transfer mediated by aromatic homoconjugated bridges. *Chem. Eur. J.* **16,** 6033–6040 (2010).

19 Zeng, L., Lee, T. Y. H., Merkel, P. B. & Chen, S. H. A new cass of non-conjugated bipolar hybrid hosts for phosphorescent organic light-emitting diodes. *J. Mater. Chem.* **19,** 8772 (2009).

20 Weller, A. Photoinduced electron transfer in solution: exciplex and radical ion pair formation free enthalpies and their solvent dependence, *Z. Phys. Chem.*, **133**, 93–98 (1982).

21 Marcus, R. A. On the theory of oxidation reduction involving electron transfer. I. *J. Chem. Phys.*, **24**, 966–978 (1956).

22 Vehmanen, V., Tkachenko, N. V., Imahori, H., Fukuzumi, S. & Lemmetyinen, H. Charge-transfer emission of compact porphyrin-fullerene dyad analyzed by Marcus theory of electron-transfer. *Spectrochim Acta A Mol Biomol Spectrosc* **57,** 2229–2244 (2001).

23 Makarov, N. S. *et al*. Impact of electronic coupling, symmetry, and planarization on one- and two-photon properties of triarylamines with one, two, or three diarylboryl acceptors. *J. Phys. Chem. A* **116,** 3781–3793 (2012).

24 Al-Subi, A. H., Niemi, M., Tkachenko, N. V. & Lemmetyinen, H. Quantitative analysis of intramolecular exciplex and electron transfer in a double-linked zinc porphyrin–fullerene dyad. *J. Phys. Chem. A* **116,** 9653–9661 (2012).

Chapter 5

Summary and Perspectives

The author has disclosed the effects of rigidity and planarity of carbon-bridged oligo-*p*-phenylenevinylenes (COPVs) on electron–vibration (e–v) coupling and electronic coupling in electron transfer (ET). In addition, the author obtained new insights into homoconjugated donor–acceptor (D–A) systems.

In Chapter 2, a series of zinc porphyrin–fullerene conjugates bridged by COPVs has been synthesized and photochemical properties were studied. It was found that a rigid and flat COPV exhibited 650-fold increase in ET rate compared with the conventional organic wires in the Marcus inverted region, where the e–v coupling affects ET greatly. The rigidity caused an unusually strong e–v coupling and accounted for the 50-fold rate enhancement, which was caused by inelastic electron tunneling; this is unprecedented for organic molecular wires. The flatness enhanced electronic coupling and accounted for the rest. This ET pathway emerged in solution at room temperatures, suggesting the practical utility of COPVs as molecular devices. The COPV wire is unique among organic and carbon nanotube nanowires regarding the diversity of molecular designs, stability, solubility, and processability.

In Chapter 3, a series of COPV*n*–fullerene dyads has been synthesized and the photochemical properties were studied. For $n = 2$ and 3, the charge separation occurred to provide the charge separated state from the singlet excited state of C_{60} produced after the ultrafast energy transfer from COPV*n* to C_{60}. The semiclassical Marcus analysis indicated the significant e–v couplings caused by COPV*n* moiety as well as the strong electronic couplings. These observations are contrastive to the oligo-*p*-phenylenevinylene (OPV)–fullerene dyads, in which the photoinduced ET does not occur due to the higher oxidation potentials arising from the flexibility of OPVs.

In Chapter 4, The COPV2 possessing triazine (TRZ) substituents, which is a new class of homoconjugated D–A system, was synthesized and the photophysical properties were studied. Efficient charge separation (CS) from COPV2 to TRZ moieties (98%) was observed in polar solvent, which can be ascribed to the short D–A distance and the multiple acceptors. The charge recombination (CR) process is successfully located in the Marcus inverted region, which is a key phenomenon to produce a long-lived charge separated state. Thus the CR rate was 100-times slower than CS rate. The electronic coupling via homoconjugation was one of the largest values among reported interactions such as π conjugation and π–π stacking.

COPVs have great potential to realize molecular electronics, which is the ultimate goal. Nevertheless, further investigations such as molecular conductance measurements using break junction method, modification of molecular skeleton to control the e–v coupling at an atomic precision, and theoretical study on the relationship between the e–v coupling and the structures of COPVs and their related compounds should be performed.

Lists of Publication

Chapter 2. Junpei Sukegawa, Christina Schubert, Xiaozhang Zhu, Hayato Tsuji, Dirk M. Guldi, and Eiichi Nakamura, "Electron transfer through rigid organic molecular wires enhanced by electronic and electron-vibration coupling", *Nat. Chem.*, **6**, 899–905 (2014). (Highlighted in News and Views, *Nat. Chem.*, **6**, 854–855 (2014).)

Chapter 3. Junpei Sukegawa, Christina Schubert, Xiaozhang Zhu, Hayato Tsuji, Dirk M. Guldi, and Eiichi Nakamura, "Large Electronic and Electron-Vibration Coupling in Carbon-Bridged Oligo(*p*-Phenylenevinylene)–Fullerene Conjugates", to be submitted.

Chapter 4. Junpei Sukegawa, Hayato Tsuji, and Eiichi Nakamura, "Large Electronic Coupling in a Homoconjugated Donor–Acceptor System Involving Carbon-Bridged Oligo-*p*-Phenylenevinylene and Triazine", *Chem. Lett.*, **43**, 699–701 (2014).

Lists of Publication not Related to the Thesis

1. Motohiro Akazome, Junpei Sukegawa, Yohei Goto, Syoji Matsumoto, "A cyclic trimer of 2-(2-aminophenoxy)propionic acid with a bowl-shaped structure", *Tetrahedron Letters*, **50**, 5382–5385 (2009).

Acknowledgement

This study was conducted under the supervision of Professor Eiichi Nakamura in the Physical Organic Chemistry Laboratory during the period of April 2011 to March 2014.

The author genuinely expresses his heartfelt gratitude to Professor Eiichi Nakamura for his enthusiastic instructions not only on the research but also on the mentality and the personality. The author gratefully appreciated Associate Professor Hayato Tsuji for his daily guidance, discussion, and encouragement. The author acknowledges a great debt to Assistant Professors Koji Harano, Laurean Ilies, Hideyuki Tanaka, and Shunsuke Furukawa. The author is grateful to Dr. Xiaozhang Zhu for his contribution to a part of synthesis in Chapter 2 and 3. Thanks also go to the members of the laboratory for their kind supports, valuable discussions, and their friendship.

The author is indebted to Professor Dirk M. Guldi and Ms. Christina Shubert at the Friedrich-Alexander Universität Erlangen-Nürnberg (Germany) for the laser flash photolysis measurements in Chapter 2 and 3.

The author would like to thank Professor Michael R. Wasielewski at the Northwestern University (USA) for providing him the opportunity to stay at his laboratory as a visiting scholar from September to December in 2011. Thanks also go to Dr. Amanda L. Smeigh and Dr. Gregory Kuzmanich for their friendship and the daily experimental assistance as well as the laser flash photolysis measurements not related to the thesis.

The author really appreciates the financial support from The University of Tokyo Global COE Program “Chemistry Innovation through Cooperation of Science and Engineering” as well as from the Department of Chemistry and the Physical Organic Chemistry Laboratory.

Finally the author would like to thank his father, Yoshinori and his mother, Toshiko for encouraging him throughout the graduate course.

Junpei Sukegawa

The University of Tokyo

Graduate School of Science

Department of Chemistry

2014